# Integer and Fractional Charge Transfer in the Doping of Poly- and Oligothiophenes

Hannes Hase

A Thesis
In the Department of
Physics

Presented in Partial Fulfillment of the Requirements
For the Degree of
Doctor of Philosophy (Physics) at
Concordia University
Montréal, Québec, Canada

June 2023

**CONCORDIA UNIVERSITY**

**SCHOOL OF GRADUATE STUDIES**

This is to certify that the thesis prepared

By: Hannes Hase

Entitled: Integer and Fractional Charge Transfer in the Doping of Poly- and Oligothiophenes

and submitted in partial fulfillment of the requirements for the degree of

Doctor of Philosophy (Physics)

complies with the regulations of the University and meets the accepted standards with respect to originality and quality.

Signed by the final examining committee:

_____Chair
Dr. Louis Cuccia

_____External Examiner
Dr. Christian Pellerin

_____Examiner
Dr. Alexandre Champagne

_____Examiner
Dr. Pat Forgione

_____Examiner
Dr. Ayse Turak

_____Thesis Supervisor
Dr. Ingo Salzmann

Approved by _____
Dr. Pablo Bianucci, Graduate Program Director

August 2, 2023 _____
Dr. Pascale Sicotte, Dean of the Faculty of Arts and Sciences

# Abstract

## Integer and Fractional Charge Transfer in the Doping of Poly- and Oligothiophenes

**Hannes Hase, Ph.D.**
**Concordia University, 2023**

In the p-doping of organic semiconductors with small molecular dopants integer-charge transfer forming ion-pairs (IPAs) and fractional charge transfer through the formation of ground state charge-transfer complexes (CPXs) have been identified as competing fundamental processes. IPAs and CPXs differently affect the performance of doped organic electronic devices, however, the conditions leading to either phenomenon are still to be fully understood. This thesis focuses on the conjugated polymer poly(3-hexylthiophene) (P3HT) p-doped with the strong molecular electron acceptor tetrafluorotetracyanoquinodimethane (F4TCNQ) and its derivatives of lower electron affinity (F2TCNQ, FTCNQ, TCNQ). Under consideration of their different dopant strengths, the role of the critical dopant concentration promoting the one phenomenon over the other is investigated. Cyclic voltammetry is used to determine ionization energy and electron affinity values of the materials involved to gauge their influence on IPA and CPX occurrence, as identified through optical and vibrational spectroscopy. Supported by electrostatic modeling taking into account the width of the Gaussian density of states (DOS) related to the highest occupied molecular orbital in P3HT, DOS broadening upon doping is considered to explain IPA formation with weaker dopants. Grazing incidence x-ray diffraction is employed to assess the interplay between the supramolecular structure and the two doping phenomena, supporting the hypothesis that a CPX polymorph can occurs that effectively prevents IPA formation for a given host-dopant stoichiometry. Conductivity data on doped films highlights the application-related impacts of these findings. Finally, for a series of custom thiophene oligomers of different lengths, instead of P3HT, the common observation of CPX formation being promoted in the molecular doping of (small) conjugated molecules is investigated. The threshold of transition into the doping phenomenology of the polymer limit is observed at a chain length of 10 thiophene units—a parameter to be considered when employing oligothiophene semiconductors in applications demanding molecular doping. Overall, due the multi-technique approach targeting doping phenomena and mechanisms of a prototypical polymer and oligomer equivalents doped with a systematic series of p-dopants, the database presented here provides a consistent and coherent point of reference for assessing the performance and phenomenology encountered with novel dopants.

# Acknowledgements

None of this work would have been possible without the constant support of my supervisor Dr. Ingo Salzmann. I am very grateful for his believing in my capabilities which, on some days, taught me a greater degree of autonomy and, on other days, gave me the motivation to continue my studies whenever I felt overwhelmed by their complexity. Thank you.

My work on this thesis was enabled through funds from the Concordia University Graduate Fellowship, the Concordia International Tuition Award of Excellence, and a research bursary from my supervisor which was paid from funds provided by the Natural Sciences and Engineering Research Council (NSERC), Le Fonds de Recherche du Québec, Nature et Technologies (FRQNT), and the New Frontiers in Research Fund (NFRF); as well as funds provided by my mother to allow me to focus on writing for the last year.

Feedback originating from a variety of viewpoints is an important drive in the development of complex ideas. In that regard, my thanks go out to Dr. Alexandre Champagne and Dr. Pat Forgione as members of my supervisory committee, Dr. Georg Heimel (former Humboldt-Universität zu Berlin, Germany) for his contributions in the conceptualization of the doping experiments, Dr. Artem Fediai (former Karlsruhe Institute of Technology, Germany) for insightful and critical correspondence about their work, Dr. Martin Oehzelt (former Helmholtz-Zentrum Berlin für Materialien und Energie, Germany) for support in computational modeling, Melissa Berteau-Rainville (Institut National de la Recherche Scientifique, Canada) for conducting said modeling and fruitful discussions on its results, Prof. Dr. Roland Resel (TU Graz, Austria) for commentary on the publication draft behind chapter 4, and Jiang Tian Liu, Venelin Petkov, and Shubham Bhagat for insightful conversations regarding oligothiophenes. I also like to thank Shubham Bhagat along with Somaiyeh Charoughchi for being the kind 'sisters-in-PhD' they were to me.

Part of the research described in this thesis was performed at the Canadian Light Source, a national research facility of the University of Saskatchewan, which is supported by the Canada Foundation for Innovation (CFI), NSERC, the National Research Council (NRC), the Canadian Institutes of Health Research (CIHR), the Government of Saskatchewan, and the University of Saskatchewan; on behalf our research team, I thank Dr. Beatriz Diaz Moreno and Dr. Chang-Yong Kim for experimental support in using beamline BXDS-IVU. Likewise, I acknowledge Elettra Sincrotrone Trieste for providing access to its synchrotron radiation facilities and thank Dr. Luisa Barba for assistance in using beamline XRD1. I am grateful to Melissa Berteau-Rainville, Somaiyeh Charoughchi, Shubham Bhagat, and Dr. Wolfgang Bodlos (former TU Graz, Austria) for measuring my samples at these facilities. Further, I like to thank Dr. Rafik Naccache and Dr. Laszlo

Kalman for the provision of their UV-vis/NIR spectrometers, Dr. Rolf Schmidt for support in using the FTIR spectrometer at the Integrated Platform for Biomolecular Function, Interactions and Structure (BIOFINS) at Concordia University, Patricia Moraille for support in using the AFM in the Laboratoire de Caractérisation des Matériaux (LCM) at Université de Montréal, and William Chicoine from the Science Technical Center at Concordia University for our conversations about and help with building laboratory equipment and mechanical repairs.

Finally, I am grateful for all the love and mental support that I received from the wonderful people at The Mindful Project at Concordia and The Hive Free Lunch, from my friends—in Montreal and those in Europe, patiently waiting for my return—and my family, especially, my loving and caring parents.

# Contribution of Authors

Chapter 4 is, except for a thesis-related foreword, based on a published manuscript by myself, Melissa Berteau-Rainville, Somaiyeh Charoughchi, Dr. Wolfgang Bodlos, Prof. Emanuele Orgiu, and Dr. Ingo Salzmann. While all authors reviewed the final manuscript and approved of the contents, the original draft was written by myself and in-depth revisions were done together with MBR and IS. Grazing-incidence x-ray diffraction data was acquired by MBR and SC at the Canadian Light Source Saskatoon, SK, Canada (data depicted in figures 4.4, C.6, C.8), and by WB at Elettra Sincrotrone Trieste, Italy (data depicted in figure C.7); note, that all data processing and analysis was done by myself. MBR conducted all calculations on the density of states (data visualized in figures 4.6 and C.10) and density functional theory calculations to provide dipole and quadrupole moments of the dopant molecules (data in table C.2). Cyclic-voltammetry data was, partially in close collaboration with me, acquired by SC (voltammograms shown in figure C.9).

# Table of Contents

# List of Figures

# List of Tables

# List of Associated Works

[1] **The Impact of Dopant Strength and Thermal Annealing on p-Doped P3HT Thin Films**
H. Hase
Master's thesis, Humboldt-Universität zu Berlin, Berlin, May 2017

The data acquired for my master's thesis can be viewed as quasi-preliminary data to the present thesis and inspired the studies included here.

[2] **Unraveling the Microstructure of Molecularly Doped Poly(3-hexylthiophene) by Thermally Induced Dedoping**
H. Hase, K. O'Neill, J. Frisch, A. Opitz, N. Koch, and I. Salzmann
*The Journal of Physical Chemistry C*, vol. 122, no. 45, pp. 25893–25899, Nov. 2018.

Based on data from [1], re-evaluated and re-interpreted for publication during the first year of my PhD program. Shifts observed in the vibrational signature of the ionized dopant in this study laid the foundation for their further discussion in sections 2.3.2 and 4.4.1 of this thesis.

[3] **Doping in Organic Semiconductors**
H. Hase and I. Salzmann
in *Handbook of Organic Materials for Electronic and Photonic Devices, 2nd Edition*
O. Ostroverkhova, Ed. Woodhead Publishing, 2019, pp. 349–383.

A review chapter on molecular doping in organic semiconductors, addressing issues beyond the scope of this thesis which, therefore, can be seen as an extension to chapters 1 and 2 here.

[4] **Approaching the Integer-Charge Transfer Regime in Molecularly Doped Oligothiophenes by Efficient Decarboxylative Cross-Coupling**
J. T. Liu, H. Hase, S. Taylor, I. Salzmann, and P. Forgione
*Angewandte Chemie International Edition*, vol. 59, no. 18, pp. 7146–7153, Apr. 2020.

Describes the synthesis and part of the characterization of the oligothiophenes featured in this thesis in chapter 5.

[5] **Chemical Doping of Organic Semiconductors**
S. Bhagat, H. Hase, and I. Salzmann
in *Organic Flexible Electronics*
P. Cosseddu and M. Caironi, Eds. Elsevier, 2021, pp. 107–141.

An updated version of [3].

[6] **Doping-Related Broadening of the Density of States Governs Integer-Charge Transfer in P3HT**
H. Hase, M. Berteau-Rainville, S. Charoughchi, E. Orgiu, and I. Salzmann
*Applied Physics Letters*, vol. 118, no. 20, p. 203301, May 2021.

Based on a small subset of the data published in [7] with increased focus on the density of states. All information in this publication has been recapitulated in [7] and is therefore part of chapter 4 in this thesis.

[7] **Critical Dopant Concentrations Govern Integer and Fractional Charge-Transfer Phases in Doped P3HT**
H. Hase, M. Berteau-Rainville, S. Charoughchi, W. Bodlos, E. Orgiu, and I. Salzmann
*Journal of Physics: Materials*, vol. 6, no. 1, p. 014004, Jan. 2023.

Reproduced in this thesis as chapter 4.

[8] **Sterically-Hindered Molecular p-Dopants Promote Integer Charge Transfer in Organic Semiconductors**
S. Charoughchi, J. T. Liu, M. Berteau-Rainville, H. Hase, M. S. Askari, S. Bhagat, P. Forgione, and I. Salzmann
*Angewandte Chemie International Edition*, vol. 62, no. 31, p. e202304964, Aug. 2023.

I was involved in optical and vibrational spectroscopy as well as conductivity measurements on poly(3-hexylthiophene-2,5-diyl) thin-films on which the novel dopant presented in that work was applied; this was benchmarked against data from [7].

[9] **Energy-Level Alignment Governs Doping Related Fermi-Level Shifts in Polymer Films**
F. Hu, M. Berteau-Rainville, H. Hase, Y. Zhang, Q. Wang, I. Salzmann, and S. Duhm
*ACS Applied Electronic Materials*, under review, 2023.

A study that virtually expands [7] through ultraviolet photoelectron spectroscopy as a means of looking at shifts of the density of states and Fermi-level shifts upon doping; I shared my sample preparation technique with the researchers conducting the experiments and assisted in the drafting of this publication.

# Chapter 1

# Introduction

Organic semiconductors (OSCs), i.e. conjugated polymers (CPs) and conjugated (small) molecules (COMs), have been the subject of intense research efforts ever since the first reports of organic light-emitting diodes (OLEDs) [10], organic photovoltaic cells (OPVCs) [11], and organic field-effect transistors (OFETs) [12] were published in the late 1980s. The first wide-spread commercial success of OSCs is their employment in OLED displays [13, 14] and white OLEDs pose as a viable contender for energy-saving lighting [15]. The general appeal of OSCs for opto-electronic devices lies with the ability to tune the optical energy gap through methods of synthetic organic chemistry—a pathway that does not exist for inorganic semiconductors (ISCs) in a similar way. Importantly, OSCs offer mechanical flexibility and allow for low energy-cost, large-area deposition techniques, i.e. vacuum sublimation (COMs) and various solution-processing methods (CPs and soluble COMs) including, among others, spin coating, blade coating, slot-die coating, inkjet printing, or roll-to-roll processing [16]. This gives rise to concepts like covering surfaces through which heat loss occurs, with large-area thermoelectric energy harvesting devices [17–19]. Adding that OSCs exhibit high absorption coefficients and, again, that their energy gap can be tuned, ultra-thin OPVCs covering green houses can be envisioned, selectively absorbing parts of the light spectrum not vital to plant growth [20]. All these properties are also key to flexible, thin, wearable electronics [17, 18, 21]. Last but not least, using bio-sourced and biodegradable OSCs with low-energy solution processing techniques holds the promise to mitigate environmental impacts of electronic device production and disposal [22, 23].

Electrically doping ISCs is the key technique in enabling virtually all modern electronic devices as it provides high levels of control over electronic material properties [24] In contrast, the parameters for efficient doping of OSCs to reliably control their electronic properties are still highly debated [25] allowing no similar level of control today. This lack of knowledge contributes to the situation that, beside the remarkable success of OLEDs and despite highly promising concepts, no other devices like OPVCs, OFETs, or thermoelectric elements have yet reached commercially viable levels of operability. Firstly, doping plays a crucial role in the generation of mobile charge carriers which reduces ohmic losses within the accordingly doped layers in a device. Increases in conductivity over multiple orders of magnitude have, indeed, been observed for doping in both CPs [26] and COMs [27] and, historically, formed the basis for the enormous interest in

the materials class of organic semiconductors honoured in 2000 by the Nobel Prize in Chemistry awarded to Alan G. MacDiarmid, Alan J. Heeger, and Hideki Shirakawa [28]. Controlling conductivity is key for the use of OSCs in transport layers including hybrid devices such as perovskite solar cells [29].

Secondly, doping is vital to deliberately control energy barriers impacting charge-transport. It allows reducing energy barriers for charge injection from electrodes and to control charge transport through the creation of n-doped electron-transporting/hole-blocking layers and, *vice versa*, p-doped hole-transporting/electron-blocking layers. This is, e.g., employed in OLEDs within so-called p-i-n structures where the optically active layer is sandwiched between a p- and n-type transport layer, allowing electrons and holes to enter from opposing electrodes but being blocked from passing all the way through the device, hence, increasing electron/hole recombination and, subsequently, the emission yield of the OLED [30, 31].

When employing molecular acceptors and donors as p- and n-type dopants, respectively, in the doping of OSCs, two complementary, fundamental phenomena can be observed: *integer charge transfer* resulting in spatially separated ion-pairs (IPAs), and *fractional charge transfer* as the result of supramolecular orbital rehybridization in the formation of ground-state charge-transfer complexes (CPXs*) [25, 32, 33]. Generally, IPA formation is regarded as the ultimate goal of doping, as it is intrinsically more efficient in the generation of mobile charge carriers due to direct ionization. This is in contrast to the charge carriers trapped in the CPX where an additional ionization step needs to take place instead [25, 33, 34]. In fact, only a few recent studies found that CPX formation is not an exclusively detrimental process and showed some value in doped systems where moderate CPX-to-IPA fractions occur, finding benefits to the performance of OLED [35], thermoelectric [36], and OFET [37] devices. Therefore, gaining control over the occurrence of the two phenomena is of application-related relevance and represents a key goal of the present work.

In first approximation, IPA formation becomes energetically favorable when the electron affinity $EA$ of the acceptor is equal to or higher than the ionization energy $IE$ of the donor; in p-doping, the dopant is the electron acceptor, the host OSC is the electron donor, and *vice versa* in n-doping. CPX formation is the result of spatial overlap and rehybridization of the frontier molecular orbitals, i.e. the lowest unoccupied molecular orbital in the ground state (LUMO) of the acceptor and the highest occupied molecular orbital in the ground state (HOMO) of the donor; this phenomenon can be seen as favorable to the host-dopant system since the formed CPX HOMO exhibits a higher binding energy for electrons than the pristine donor HOMO [38]. Clearly, conditions for IPA and CPX formation do not exclude each other: CPXs can be seen in $EA > IE$ situations and IPA formation was observed in cases where the spatial arrangement for CPXs was structurally possible [38–40]. The identification of additional parameters governing either phenomenon is an ongoing and vivid field of research, which the present thesis aims to join. A comprehensive introduction into the fundamentals of these doping scenarios

*'CPX' was chosen as the abbreviation for 'ground-state charge-transfer complex', here, to conform with the most influential studies [33, 34] behind this thesis. While, e.g., 'CTC' appears to be a more straightforward option, choosing 'CPX' allows, e.g., the unaltered use of figure 2.8.

is provided in **chapter** 2 and according experimental characterization methods, as employed in this thesis, are explained in **chapter** 3.

In all aforementioned application scenarios of OSCs as well as in fundamental studies, conjugated poly- and oligothiophenes have attracted particular attention in recent decades [36, 41–46]. The CP poly(3-hexylthiophene-2,5-diyl) (P3HT) p-doped with the strong molecular acceptor 2,3,5,6-tetrafluoro-7,7,8,8-tetracyanoquinodimethane (F4TCNQ) represents a prototypical system in the investigation of doping-related phenomena, not only in this material class but also for OSCs in general. Further, it is known that for the (existing) F4TCNQ derivatives with fewer fluorine substitutions (see skeletal structure in figure 2.4), i.e. 2,5-difluoro-7,7,8,8-tetracyanoquinodimethane (F2TCNQ), 2-fluoro-7,7,8,8-tetracyanoquinodimethane (FTCNQ), and 7,7,8,8-tetracyanoquinodimethane (TCNQ), in this order, the *EA* values decrease [47, 48] as LUMO-level stabilization through the electron-withdrawing property of the fluorine substituent decreases [47]. Meanwhile, CPX occurrence with P3HT increases, reducing therefore the amount of IPAs formed [1, 34]. Considering that the spatial demand of the dopant remains virtually the same while its *EA* changes significantly, this series of dopants is an ideal system to isolate that parameter to assess doping-related phenomena. Based thereon, regardless which member of this 'FxTCNQ' series is employed, one can conclude that higher *EA* values do promote IPA formation. But this parameter does not stand alone since recent studies employing the strongest dopant of the FxTCNQ series, F4TCNQ,[†] have reported that CPXs can still replace IPAs, depending on dopant concentration, P3HT average molar weight, thin-film deposition parameters [39], or degree of randomness in P3HT side-chain orientation (its regio-regularity) [49]. While these findings paint the image of a truly multi-faceted issue, "[...] the experimental data are often a fragmented patchwork [...]", as a recent review [25] on OSC doping expressed in general; investigations of the P3HT-FxTCNQ system are no exception. Hence, the central study [7] of this thesis, presented in **chapter** 4, was conducted with the goal of providing a broad, coherently produced dataset on FxTCNQ-doped P3HT thin-films for a series of dopant concentrations around the threshold to the high-concentration regime, where CPX formation does occur with F4TCNQ.

An assuring level of comparability is provided by having optical and vibrational absorption spectroscopy, cyclic voltammetry, conductivity, and grazing-incidence x-ray diffraction (GIXRD) all measured under largely the same sample preparation conditions, instead of being brought together from various publications across different laboratories. Firstly, this allows for the scrutiny of commonly used CPX and IPA indicators. In particular, vibrational spectroscopy is often employed, recording shifts in the position of the C≡N stretching modes of FxTCNQs that can be assigned to fractional charge transfer (CPX phenomenon) or integer charge transfer (IPA phenomenon) and show whether neutral dopants are present in a sample [4, 33, 34, 36, 39, 49, 51–58]. The ambiguity of these assignments had already been pointed out in the late 1980s [53] but investigations into other factors influencing the C≡N mode positions only gained traction in recent

[†]1,3,4,5,7,8-Hexafluorotetracyanonaphthoquinodimethane (F6TCNNQ) is a stronger dopant than F4TCNQ and could be regarded as an extension to the FxTCNQ series, however, spatial demand is not as comparable as within the FxTCNQ series due to the naphthoquinone core of F6TCNNQ instead of the quinone core of FxTCNQs [50].

years [2, 54, 58–60], including a recent theoretical study of our group [61] and an own publication [2] created in the framework of my master's thesis [1]. The present broad multi-technique dataset allows to review and evaluate these investigations in a wider context.

Secondly, the main goal of chapter 4 is, of course, to further the determination of parameters leading to either CPX or IPA formation. To this end, for all $EA$ values and concentrations of the FxTCNQs employed, the percentage of dopants in IPAs is estimated from vibrational spectroscopy data and held against a model of doping-induced broadening of the Gaussian-shaped density of states (DOS) [33, 34, 62, 63] of the HOMO levels in P3HT. The idea behind this model is that the introduction of dopants drives structural disorder (resulting, e.g., in variations in polarization energy) and conformational disorder (leading to a locally varying $IE$), which overall translates into a broader energy distribution of HOMO levels in the host OSC matrix. Consequently, they reach further towards the LUMO energy levels of weaker dopants, thus, allowing for the ionization of a higher portion of dopants. In other words, high IPA content produced with low-$EA$ dopants is the result of a P3HT HOMO-DOS width that is broader than that of pristine P3HT [64]. Still, however, in some cases of high CPX occurrence discussed in this work, calculations using a HOMO-DOS width even narrower than that of pristine P3HT can yield significantly higher IPA content than experimentally observed. Questioning the physical sensibility of this observation opens a discussion about the extent to which CPX occurrence can be modeled by considering the DOS alone. Finally, adding the analysis of structural data from GIXRD allows discussing a possible host-dopant stoichiometry-dependence as a factor deciding whether IPA or CPX formation are favored.

To date, the expertise I gathered in the production of this extensive P3HT-FxTCNQ dataset led to my involvement in two publications where (i) the performance of a novel dopant in P3HT was referenced against F2TCNQ and F4TCNQ [8] and (ii) the dataset was extended through ultraviolet photoelectron spectroscopy [9] (see List of Associated Works for details). These works are not included in the present thesis but may serve the inclined reader as follow-up literature.

**Chapter 5** is then dedicated to the comparison of the situation found in the CP P3HT with that in structurally comparable oligothiophenes. Contrasting the various size and batch-to-batch differences that polymers can exhibit, the uniform size distribution and reproducibility of oligothiophenes can be of significant application-related relevance [65–68]. However, in contrast to P3HT, the FxTCNQ-doped oligothiophenes experimentally studied, to date, predominantly exhibited CPX formation, exclusively [34, 38]. On the one hand, this might be an issue of conjugation length, as those investigations did not venture beyond six thiophene repeat units, i.e. $\alpha$-sexithiophene (6T) [38]. On the other hand, the studied oligothiophenes, $\alpha$-quarterthiophene (4T) and 6T, did not include hexyl side-chains as featured in P3HT. Therefore, chapter 5 characterizes F4TCNQ- and F2TCNQ-doping of a series of hexylated oligothiophenes (h$x$Ts) ranging from $x = 4$ to 10 thiophene units (full names in section 5.2, skeletal structure in figure 2.2), using optical and vibrational absorption spectroscopy as well as cyclic voltammetry. Indeed, IPAs start to occur at a backbone length of 10 units, therefore identifying for the first time the critical chain length for IPA formation in oligothiophenes. This outcome is discussed in light of the recent finding that the existence of an alkyl side-chain region plays an important

role in facilitating IPA formation, assisting in keeping distance between the dopant radical anion and the vicinity of the host's π-conjugated backbone [69]; the latter creates an environment electrostatically less favorable for integer charge transfer [70].

In summary, the present thesis aims to further the elucidation of the conditions for fractional charge transfer—in competition with integer charge transfer—in situations where host-dopant frontier-orbital overlap and subsequent CPX formation cannot be excluded. In particular, the prototypical system of F4TCNQ-doped P3HT is investigated through the lens of a wide array of experimental methods, by substituting F4TCNQ with structurally comparable dopants of weaker dopant strength (FxTCNQs) and using oligomer equivalents of P3HT (h*x*Ts). The overarching conclusions of this thesis can be found in **chapter 6**. Overall, this work contributes to advancing the knowledge of fundamental concepts behind the doping of OSCs which, in turn, constitutes an important building block in the development of organic and organic-inorganic hybrid (opto-)electronic devices.

# Chapter 2

# Fundamentals of Doping Organic Semiconductors

The material class of organic semiconductors (OSCs) consists of conjugated (small) molecules (COMs) and conjugated polymers (CPs). The bandgap $E_g$ in OSCs is typically greater than in inorganic semiconductors (ISCs) such as silicon ($E_g = 1.1\,\text{eV}$ [24, 71]). Therefore, intrinsic OSCs are essentially electronic insulators which can, for one, become conductive upon optical activation of charge carriers, an appealing property underlying all opto-electronic applications. While thermal activation occurs in small-bandgap ISCs, energy gaps in OSCs are typically much greater, that is, in a defect-free pure semiconductor. However, chemical defects are commonplace with practically achievable levels of compound purity and can donate mobile charge carriers. To actually control the introduction of mobile charge carriers, it is common practice to bring select guest molecules into the OSC host matrix. This practice is referred to as *molecular doping*. Its underlying mechanisms are still plagued with open questions, some of which the present thesis aims to address. To understand these issues, first, an introduction into the fundamentals of conjugated molecular orbitals, is provided in section 2.1. Then, as the doping of ISCs is well established as a standard topic in introductory solid-state physics courses, section 2.2 recapitulates the basic concepts and, by pointing out the contrasts to ISCs, explains why OSC doping is subject to many unresolved issues, of which some are addressed in this thesis. Finally, section 2.3 explores the fundamental OSC doping-phenomena—ion-pair (IPA) and charge-transfer complex (CPX) formation—while 2.4 takes a look at how these are influenced by the microstructure.*

## 2.1 Conjugated Molecules

At the basis of understanding molecular orbitals in OSCs lies the configuration of the six electrons of the carbon atom in the ground state, namely, $1s^2 2s^2 2p^2$. Four valence electrons are found in the $2s^2 2p^2$ orbitals of which $2p^2$ can be practically divided into

*This is a commonly used term in the research field of OSCs, where the term 'micro' in 'microstructure' is to be understood in contrast to 'macro' and does not strictly refer to the micrometer scale, but rather to micrometer and below; thus, the term here also encompasses the nanometer scale.

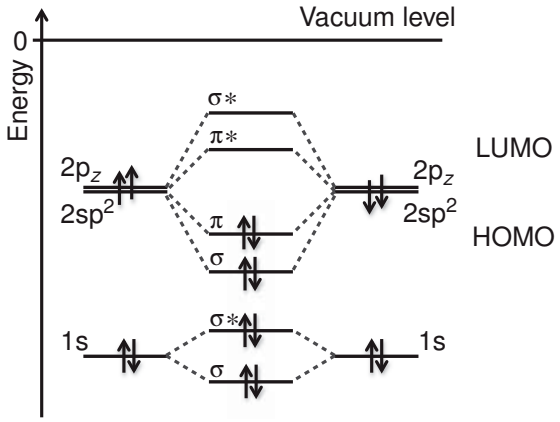


Figure 2.1: Schematic energy level diagram of σ- and π-bonds forming from atomic orbitals between the carbon atoms in ethene (i.e. the four $2sp^2$-orbitals forming σ-bonds with the hydrogen atoms are omitted). Note, that energy in this depiction refers to the kinetic energy of the free electron and, consequently, orbital levels are shown at the negative value of their binding energy.
From [73] A. Köhler and H. Bässler, *Electronic Processes in Organic Semiconductors: An Introduction*. Weinheim: Wiley-VCH, 2015. Copyright 2015 Wiley-VCH Verlag GmbH & Co. KGaA.

$2p_x^1 2p_y^1 2p_z^0$, named for their orthogonal, three-dimensional orientation to one another. A specialty of carbon is its affinity to undergo sp, $sp^2$, or $sp^3$ hybridization through linear combinations of its 2s-orbital with one, two, or three 2p-orbitals, respectively. (Note that with hybridization nomenclature the numbers in superscript refer to the number of p-orbitals involved, not to the number of electrons in an orbital.) This hybridization can become energetically favorable in the vicinity of orbitals of neighboring atoms, hence, is an effect in bound carbon [72, 73]. Most relevant for OSCs is the $sp^2$ hybridization with one p-orbital left unhybridized, commonly denoted as $p_z$. The latter is oriented perpendicular to the three coplanar, equiangular, and energetically degenerate $2sp^2$-orbitals. In these total of four orbitals resides each one of the four valence electrons, offering electron-pair sharing with neighboring atoms, hence, covalent bonding.

Molecular orbitals are defined through the possibilities of interference between the constituting atomic-orbital wavefunctions. Where constructive interference occurs, the atomic orbital overlap in-between the nuclei is adding up in the molecular wavefunction, i.e. the probability for electrons to exist in this region is increased. This shields the electrostatic repulsion of the nuclei, thus, provides an energy reduction to the system. Being energetically favorable to harbor electrons, such a molecular orbital is referred to as *bonding*; analogously, destructive interference enhances the repulsion of the nuclei and molecular orbitals where it is dominant, are therefore referred to as *anti-bonding* [72, 73]. Bonding and anti-bonding molecular orbitals whose electron density is centered around the bonding axis are called σ- and σ*-orbitals, respectively; they are accordingly named π- and π*-orbitals if the electron density is mainly found above and below the bond axis [73].

When $sp^2$-hybridized carbon atoms are bonded to each other, the $2p_z$-orbitals protrude perpendicular from the bond axis. Therefore, the $2sp^2$-orbitals have a much greater overlap with each other than the $2p_z$-orbitals, which makes the effects of both constructive and destructive interference larger in σ- and σ*-orbitals than in π- and π*-orbitals, respectively. In other words, the binding energy of electrons in σ is higher than in π and in σ* lower than in π* [72, 73]. As the $2sp^2$- and $2p_z$-orbitals each contribute only one electron, all electrons can reside in the bonding orbitals which effectively makes π the highest occupied molecular orbital in the ground state (HOMO) and π* the lowest unoccupied molecular orbital in the ground state (LUMO). As such, they are also known as the *frontier orbitals* and play a critical role in OSCs [73]. Figure 2.1 illustrates the formation of σ- and π-bonds between the carbon atoms in ethene on a typical energy level diagram, however, the energy axis is oriented with the kinetic energy of the free electron in mind and, consequently, orbital levels are shown at the negative value of their binding energy.

Experimentally, the energy levels of HOMO and LUMO are commonly characterized by the ionization energy $IE$ and the electron affinity $EA$, typically directly measured through ultraviolet photoelectron spectroscopy (UPS) and inverse photoelectron spectroscopy (IPES), respectively [25, 74]. The principle of UPS and IPES being *in-vacuo* electron extraction and injection, respectively, underlies the free-electron notation for the energy scale, as used in figure 2.1. For the sake of discussing the effects of higher and lower $IE$ or $EA$ throughout this thesis, their values are provided on a positive binding-energy scale if not specified otherwise; the binding-energy axis is commonly drawn inverted for visual comparability (*cf.* figures 2.5 and 2.6). Recently, the assessment of $IE$ and $EA$ from redox potentials $V_{\text{redox}}^{\text{HOMO}}$ and $V_{\text{redox}}^{\text{LUMO}}$, respectively, as measured by cyclic voltammetry (CV) rather than by UPS/IPES has gained attention among researchers working on OSCs (in addition to, of course, its much more budget-friendly experimental setup). It must be considered that CV is a measurement of intermolecular charge-transfer [48, 75] probing solid-state effects on $IE$ and $EA$ only in few, limited cases [76–78]. In contrast, UPS and IPES are commonly conducted on solid samples but suffer from pronounced surface-sensitivity and the dependence on molecular orientation [79] alongside final-state effects [80]. For the latter issues, CV might be preferred over UPS/IPES, on a case-to-case basis, as well; sections 4.3.5 and 4.4.2 explain why CV was chosen in the present thesis and a technical introduction into CV can be found in section 3.3.

Where the molecular structure can be represented by alternating single and multiple bonds, a *conjugated system* is formed whereas the term 'conjugation' denotes the interaction between p-orbitals across the σ-bond sandwiched between the multiple bonds [81]. While the σ-orbitals form the structural backbone of the molecule, harboring strongly localized electrons, the π-orbitals are delocalized over many atoms, mostly forming electron clouds above and below the molecular plane of the conjugated system [73]. The extent of this plane and, more generally, the planarity of a CP segment or COM is vital to the extent of coherent π-electron delocalization which is termed *conjugation length* [73]. This term is of key significance in OSC research as π-electron delocalization—in connection with lower binding energy compared to σ-electrons—is crucial to intra- and intermolecular charge transport. In addition, the conjugation length is key to optical absorption and emission; qualitatively, this can be understood through the quantum-well model where a wider well yields lower-energy transitions, hence, optical absorption and emission take

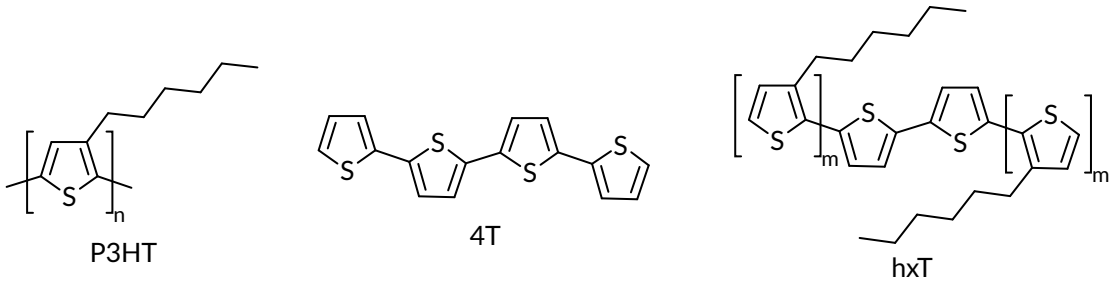


Figure 2.2: Skeletal structures of the OSCs most prominent in this thesis: the CP poly(3-hexylthiophene-2,5-diyl) (P3HT) and the COMs $\alpha$-quarterthiophene (4T) and h$x$T (full names in section 5.2); the latter denotes a series of hexylated oligothiophenes synthesized for the study presented in chapter 5.

place at lower energies for larger conjugation lengths [73]. Particularly in CPs, coherence in $\pi$-electron delocalization may be weakened, i.e. effectively interrupted, through conformational variation (resulting from solvent interaction and subsequent solid-state deposition) as well as the degree of torsional disorder along the polymer chain, chemical defects, and phonon scattering [73]. Spectroscopically, a CP can therefore be approximated by oligomers whose number of repeat units is equivalent to the CP's conjugation length. In polythiophenes, as employed in the present work, the conjugation length typically constitutes 5–6 repeat units but over 20 when the polymer adapts a fully planar conformation in the solid state [73]; following a $1/x$-dependency on the number $x$ of consecutive thiophene rings in a plane, the fundamental absorption onset in the solid state lies at lower energies than in the dissolved state [65, 82–85]. This thesis focuses on poly(3-hexylthiophene-2,5-diyl) (P3HT) in comparison with a custom synthesized series of oligomer equivalents ('h$x$Ts'; full names in section 5.2) and previous studies on oligothiophenes, most notably, $\alpha$-quarterthiophene (4T) [33, 34, 86]; their skeletal structures are depicted in figure 2.2.

## 2.2 Doping of Organic *versus* Inorganic Semiconductors

In contrast to OSCs, the mechanisms behind doping (crystalline) ISCs are well established to the point that they are part of virtually every entry-level solid-state physics course. Research into OSC doping is mostly conducted on issues where it deviates from its inorganic counterpart. Therefore, it is sensible to recapitulate the basic concepts of ISC doping, first. In ISCs, impurity atoms are introduced as dopants into a (most often) highly pure, highly crystalline semiconductor matrix. The ratio between dopant and host atoms ranges between $10^{-6}$ to $10^{-3}$ and they bond covalently to one another. The dopant atoms introduce electronic defect states within the fundamental energy gap of the host crystal; in a *p-doping* example, the boron dopant in a silicon host introduces unoccupied states at only 44 meV above the valence band (VB) edge; in an *n-doping* example, a phosphorous dopant in silicon introduces occupied levels at 46 meV below the conduction band (CB) edge [24]. These energetically shallow levels draw the Fermi level $E_F$ from its

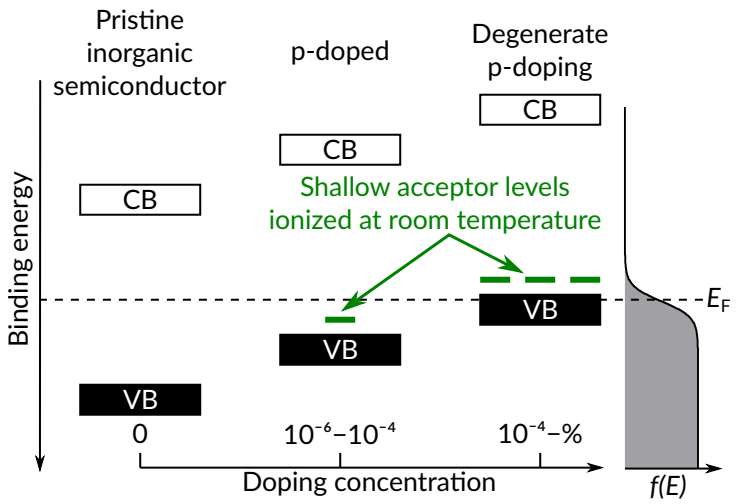


Figure 2.3: Schematic energy-level diagram of an inorganic semiconductor for p-type doping at different doping concentrations, relative to the Fermi level $E_F$, set against the Fermi function $f(E)$, with 'CB' and 'VB' denoting the conduction and valence band, respectively. Concentration threshold into the degenerate regime represents boron-doped silicon [87].
Redrawn and adapted from [89] I. Salzmann and G. Heimel, "Toward a comprehensive understanding of molecular doping organic semiconductors (review)," *Journal of Electron Spectroscopy and Related Phenomena*, vol. 204, pp. 208–222, Oct. 2015. Copyright 2015 Elsevier.

mid-gap position of the pristine semiconductor towards the corresponding band edges, the VB for p-doping and the CB for n-doping, respectively. With electron occupation following Fermi-Dirac statistics at room temperature, these shallow levels become ionized by accepting electrons from VB and donating electrons into CB in the case of p- and n-doping, respectively. Through this, mobile majority charge-carriers, i.e., holes in VB and electrons in CB are generated, leading to desired increases in conductivity. With a *doping efficiency*, i.e. holes/electrons generated per p/n-dopant added, of ≈1 in doped ISCs, dramatic increases in conductivity can be observed at doping ratios of $10^{-5}$ and below. Because of this, the host structure is largely unperturbed and charge-carrier mobility is retained as, otherwise, dopants would constitute considerable scattering centers in band transport. Further, through the shift of $E_F$, electronic band alignment can be exploited to tailor contact resistance with electrodes and selectively control charge-carrier transport with differently doped semiconductors—a circumstance employed in, e.g. the p-n junction and field-effect transistors, generally forming the basis for all modern Si-based electronics [24]. Notably, for doping ratios in, e.g., boron-doped silicon of $1.3 \times 10^{-4}$ and higher [87], $E_F$ shifts into VB/CB and the semiconductor becomes *degenerate*, effectively enabling metallic behavior [24, 88]. Figure 2.3 summarizes the energy levels of doping in ISCs on the example of p-doping.

First ventures into doping OSCs occurred since the late 1970s through employing halides on both CPs [90–92] and COMs [93], yielding conductivity increases by mul-

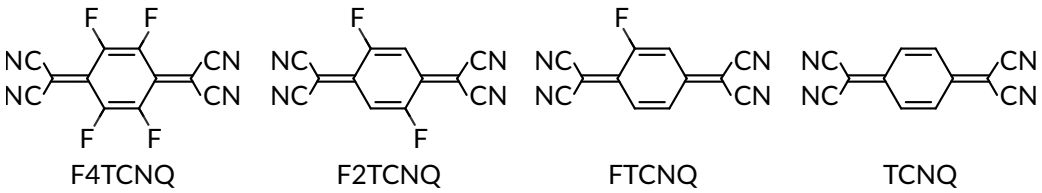


Figure 2.4: Skeletal structures of the p-dopants employed in this thesis: 2,3,5,6-tetrafluoro-7,7,8,8-tetracyanoquinodimethane (F4TCNQ), 2,5-difluoro-7,7,8,8-tetracyanoquinodimethane (F2TCNQ), 2-fluoro-7,7,8,8-tetracyanoquinodimethane (FTCNQ), and 7,7,8,8-tetracyanoquinodimethane (TCNQ).

tiple orders of magnitude. Later approaches employed alkali metals as n-dopants but proved not practical as such small dopant species were found to diffuse readily [94] making, e.g., doped injection layers for ohmic contact or organic p-n junctions unstable under operating conditions. In response, larger *molecular dopants* had been used ever since, enabling conductivity to be tunable by several orders of magnitude in COMs [27] and CPs [26]. A prominent example of p-type dopant is the strong molecular acceptor 2,3,5,6-tetrafluoro-7,7,8,8-tetracyanoquinodimethane (F4TCNQ)–a derivative of 7,7,8,8-tetracyanoquinodimethane (TCNQ) with fluorine substitutions serving to increase the *EA*. Along with F4TCNQ, 2,5-difluoro-7,7,8,8-tetracyanoquinodimethane (F2TCNQ), 2-fluoro-7,7,8,8-tetracyanoquinodimethane (FTCNQ), and TCNQ are employed in this thesis (see structures in figure 2.4), here collectively termed 'FxTCNQs', providing a series of structurally similar dopants with decreasing *EA* values, in that order [47, 48].

Major contrasts to ISC doping stem from a more complex microstructure of OSCs brought about by their different constituents, i.e. atoms and atomic dopants for ISCs *versus* COMs/CPs and molecular dopants for OSCs. Firstly, orientation matters since most molecules are not rotationally invariant. This plays an important role for virtually all physical properties that are therefore typically anisotropic as well. As *polymorphism*, i.e. crystal-structure variation of chemically equal compounds, is observed very commonly for organic molecular solids [95], e.g. different polymorphs (sometimes surface-mediated and nonexistent in the bulk) occurring in the channel of OFETs can affect the characteristics of the transistor [96]. Surface-sensitive x-ray diffraction techniques like grazing-incidence x-ray diffraction (GIXRD; see section 3.4) are often used to determine unit-cell parameters of these different crystalline phases from Bragg peak positions [97–99] while molecular orientations within the unit cell can be deduced from the diffraction intensities or theoretical modeling [100–102].

Secondly, the constituents of the solid are not covalently bound like in ISCs but, rather, held together by van-der-Waals and electrostatic interactions. Not only does this result in significantly lower bond strength and, subsequently, lower mechanical strength, but it also leads to differences in the electronic structure, as compared to ISCs. Even in single crystals, the width of the HOMO/LUMO derived bands is typically at least one order of magnitude smaller than that of VB/CB in crystalline Si [103]. Therefore, band transport in OSCs is the exception rather than the rule and only observed in very pure single crystals and along polymer chains [104]. Instead, charge transport occurs by thermally

assisted hopping from site to site. Further, the low dielectric constant (often around 3 in OSCs in contrast to >10 in ISCs) means electron-hole pairs tend to be strongly Coulombically bound and described as Frenkel excitons [105], thus, optical absorption/emission is largely defined either by the single molecules or, at most, nearest neighbors. Finally, the density of states (DOS) in an ideal ISC parabolically cuts off at the band edges (where mobile charge carriers are energetically situated) and, therefore, the DOS is zero within the band gap [24]. In contrast, the culmination of weaker binding and the lack of rotational invariance translates into an inherently greater disorder in OSCs, which introduces localized states into the gap; i.e. *structural disorder* causes a broader variation in, e.g., polarization energy while conformational disorder influences locally dependent $IE/EA$ values, resulting in increased *energetic disorder* entailing a broader spread of energy levels. As a result, the band edge region can be modeled as an exponential DOS instead [106], and, more generally, the DOS follows a Gaussian distribution where disorder governs the Gaussian width [62, 107].

## 2.3 Organic-Semiconductor Doping Phenomena

### 2.3.1 Ions and Polarons

So far, degenerate doping of OSCs, i.e, the concept that $E_F$ moves from its mid-gap position into VB/CB for a sufficiently high p-/n-dopant concentration has not been consistently observed for OSCs.[†] Instead, it is generally observed that the $E_F$ shift saturates at elevated dopant concentrations [109–114] and degenerately doped OSCs, in contrast to ISCs, do therefore not seem to exist. This is commonly interpreted as a result of the formation of singly occupied polaronic states which, until recently, were thought to lie in the fundamental gap of the pristine OSC due to the polarization of surrounding molecules (and repeat units in a polymer), i.e., due to the reorganization energy $\lambda$ (see figure 2.5(a)) [108, 115–118]. However, even if dedicatedly investigated, such polaronic states could not be observed [38].

Subsequently, a revision to the polaron energetics was suggested by Winkler et al. [119], explaining the absence of states at $E_F$ for charged OSCs. Figure 2.5(a) shows the traditional energy-level diagram of a positive polaron with the cation surrounded by neutral molecules: an electron is removed from the HOMO and as a result of geometrical relaxation the now singly occupied level shifts by $\lambda$ into the gap. This level should be observable *via* UPS, accompanied by a LUMO level of increased binding energy, detectable through IPES [116]. While Winkler et al. observed the latter, a singly occupied level did not appear and, instead, a UPS feature at higher binding energy than the neutral HOMO was recorded. To explain this, the revised view depicted in figure 2.5 was devised. Firstly, the energy $IE^0$ to remove an electron from the neutral molecule is equal to the gain in energy $EA^+$ to return it to the relaxed cation plus the reorganization energy $\lambda$.

[†]An early UPS study, p-doping P3HT with the inorganic dopant $NOPF_6$, did report indications of $E_F$ shifting into the HOMO manifold at high doping ratios [108]. However, this remained an isolated observation in literature ever since, which challenges its interpretation as OSC degeneration in the experiment cannot be ruled out.

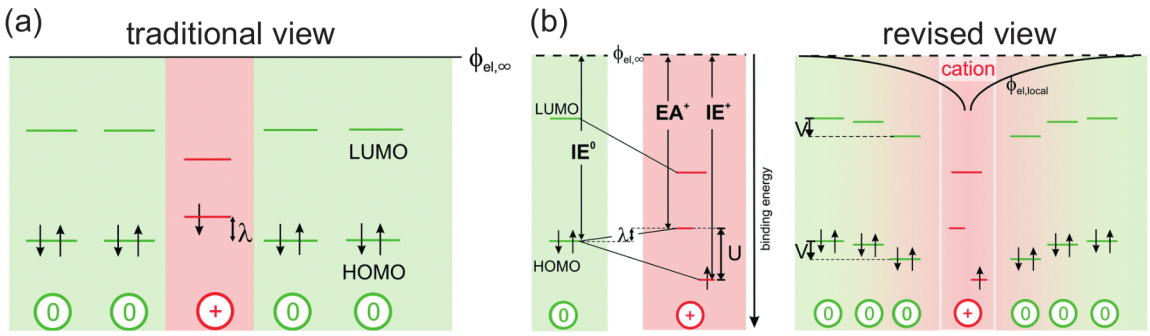


Figure 2.5: Single-particle energy levels (red) in a neutral-molecule matrix (green), exemplified on a cation. (a) Traditional view with the common vacuum level $\phi_{el,\infty}$ and reorganization energy $\lambda$. (b) Revised view considering on-site Coulomb interaction $U$, causing a split of the charged HOMO level into an occupied and an empty sublevel (left), and distance-dependent inter-site Coulomb potential $\phi_{el,local}$ up to a value of $V$ (right). Modified from [119] S. Winkler, P. Amsalem, J. Frisch, M. Oehzelt, G. Heimel, and N. Koch, "Probing the energy levels in hole-doped molecular semiconductors," *Materials Horizons*, vol. 2, no. 4, pp. 427–433, 2015. Published 2015 by The Royal Society of Chemistry under CC BY 3.0.

Then, the cation ionization energy $IE^+$ is considered to be greater than $IE^0$ due to on-site Coulomb interaction with electrons in the HOMO ('Hubbard $U$' [120]), leading to a split of the singly occupied level into an unoccupied sublevel shifted by $\lambda$ into the gap, and an occupied one shifted by $U - \lambda$ into the HOMO manifold. Finally, due to the low dielectric constant in OSCs, intersite Coulomb interaction is considerable, which adds a component up the value $V$ to the energy levels of the surrounding neutral molecules, following the Coulomb-potential well $\phi_{el,local}$ around the cation. The negative polaron scenario works in a manner analogous to the description of the cation above [119]. This revised view has since been independently, experimentally confirmed on a doped OSC [121]. Overall, to this end UPS cannot be used as direct evidence for p-doping since photoemission of the singly occupied level is easily masked by that of the surrounding neutral matrix and alternative experimental methods must therefore be employed. A UPS study [9] (currently under review; see List of Associated Works for details) that I was involved in but is not featured in this thesis, investigated the shift of $E_F$ and changes in the occupied DOS upon F4TCNQ-, F2TCNQ-, and TCNQ-doping of P3HT and can therefore be seen as a UPS-based extension of [7], i.e., of chapter 4, here.

A common starting point to evidence IPA formation in OSCs is optical absorption spectroscopy in the ultraviolet to near-infrared, often denoted 'UV-vis/NIR' spectroscopy (*cf.* section 3.1), where characteristic transitions of the ionized dopant and host can be observed. As section 4.3.1 demonstrates, among others, the absorption onset of the neutral host, e.g. P3HT at 2 eV, allows to clearly observe features of the dopant radical cation, e.g. $F4TCNQ^{\bullet-}$ with sharp peaks (solid vertical lines in figure 4.2) at 1.45 and 1.63 eV [33, 34, 39, 122–124], along broad P3HT polaron features (yellow shaded areas in figure 4.2) around 0.5 and 1.6 eV [34, 124–126].

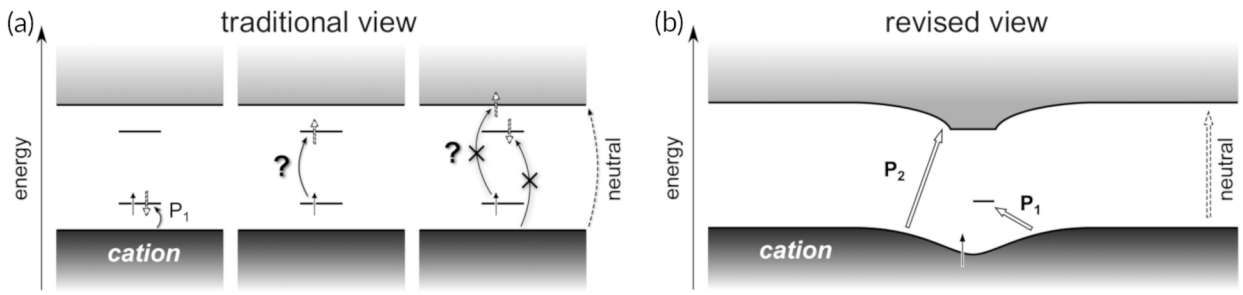


Figure 2.6: Energy levels in a cationic segment in a CP with suggested optical transitions of the polaron. Dark- and light-gray-shaded boxes symbolize the CP valence and conduction bands, respectively. (a) Traditional view (*cf.* figure 2.5(a)); question marks denote transitions impossible within the revised view; crossed-out transitions have been questioned in literature [127, 128]. (b) Revised view (*cf.* figure 2.5(b)). Note, that energy in this depiction refers to the kinetic energy of the free electron and, consequently, energy levels are shown at the negative value of their binding energy.
Modified from [126] G. Heimel, "The Optical Signature of Charges in Conjugated Polymers," *ACS Central Science*, vol. 2, no. 5, pp. 309–315, May 2016. Copyright 2016 American Chemical Society.

The energy levels between which the polaron transitions occur are still under debate. A theoretical work by Heimel [126] adapted these to the energy levels in the revised view by Winkler et al. [119], as described above (figure 2.5). As depicted in figure 2.6, both transitions include the neutral HOMO level of a surrounding molecule or, in this case, polymer segment; the smaller energy transition would then occur towards the unoccupied split half-level within the gap while the higher energy one would be a transition to the LUMO of the cation; note, that more transitions are predicted by the classical view than the two that are experimentally, unambiguously observed—a discrepancy that has been mentioned and investigated already in the early 1980s [127, 128].

A related phenomenon is the coupling of two polarons to form a spin-less quasiparticle, a *bipolaron* [116]. It is mainly observed with stronger dopants or electrochemical doping [129–132] but is not ruled out to exist for, e.g. F4TCNQ at high dopant concentrations [130] as well. Therefore, while not greatly applicable to the systems investigated here, bipolarons are still considered in sections 4.3.1, 4.3.4, and 4.4.1, concluding that recently associated near-infrared features [130] can alternatively be assigned to increased polaron delocalization [58] and ground-state charge-transfer complex (CPX; *vide infra*) formation [39].

While host and dopant atoms are selected to yield desired (opto-)electronic properties in ISC doping, a level of complexity—and opportunity—is added in OSC doping as host and dopant molecules can be gradually altered via chemical modifications, e.g., with structurally comparable derivatives of varied electronic properties. A prime example is the aforementioned fluorination series of TCNQ-derived dopants (FxTCNQs) employed in this thesis, as these dopants' *EA* values increase with the number of fluorine atoms [47, 48] due to LUMO-level stabilization through the electron-withdrawing property of

the fluorine substituent [47].[‡] While the *EA* of TCNQ is insufficient for IPA formation with P3HT, ionic UV-vis/NIR features were found to gain in strength, going from FTCNQ to F4TCNQ [34]. This property is used in chapter 4 to investigate the energetic threshold for IPA occurrence.

Similarly, peripheral substitutions on the host molecules can benefit ionization through the electrostatic environment they create [133–136]. On the one hand, Li et al. [70] recently calculated that the *EA* of F4TCNQ is effectively reduced by up to 0.7 eV in the vicinity of the host's π-conjugated core (e.g. in the case of pentacene and *N*,*N*′-di(1-naphthyl)-*N*,*N*′-diphenyl-(1,1′-biphenyl)-4,4′-diamine, known as NPB or NPD); this is argued to be the result of electrostatic contributions to *EA* due to the fundamentally different charge-density distributions (electrostatic layouts) in compounds with electron-attracting groups at the molecular periphery (e.g. C≡N in FxTCNQs) *versus* those with electron-rich π-conjugated cores. On the other hand, Comin et al. [69] calculated that F4TCNQ residing in the alkyl side-chain region of poly(2,5-bis(3-tetradecylthiophen-2-yl)thieno[3,2-*b*]thiophene) (known as PBTTT) effectively adds >0.5 eV to the *EA*, as such a spatial arrangement positions the electrostatic layouts of host and dopant molecules in a way that is more favorable to integer charge transfer. Such effects of anisotropy, again, demonstrate the increased complexity in comparison to ISC doping. In addition, the side-chain environment can thermally stabilize the dopant position [137]. Indeed, in alkylated polythiophenes, dopants are mostly found to reside in the alkyl-chain regions [2, 36, 56, 58, 138–142]. Therefore, hexylation is a key aspect to the h*x*T oligothiophenes featured in chapter 5, drawing conclusions from contrasts with studies on side chain-free equivalents [34, 38, 143, 144].

### 2.3.2 Charge-Sensitive Vibrational Bands

A commonly employed method to assess IPA formation, easily accessible through Fourier-transform infrared spectroscopy (FTIR; see section 3.2), and one that receives special attention in this thesis, is the analysis of vibrational absorption bands that are sensitive to the charged state of a molecule. This is the case for two sets of mid-infrared fingerprint bands in TCNQ derivatives, namely, the C≡N stretching and ring C=C stretching modes. Here, the degree of charge transfer $\delta$ between host and dopant can be estimated *via*:

$$\delta = \frac{2\Delta\nu}{\nu_0}\left(1 - \frac{\nu_1^2}{\nu_0^2}\right)^{-1}, \tag{2.1}$$

through the wavenumber shift $\Delta\nu$ of the vibrational bands from the neutral-molecule position $\nu_0$ ($\delta = 0$), under knowledge of the radical-anion position $\nu_1$ ($\delta = 1$) [51, 52]. Between the two sets of fingerprint bands in question, an early work by Meneghetti and Pecile [53] recommends using the ring C=C modes around 1500 $\mathrm{cm}^{-1}$ for their good agreement with the expected $\delta$ value; indeed, using these modes led to reliable results in mixed single-crystal COMs with TCNQ, F2TCNQ, and F4TCNQ [145]. However, CPs

[‡]The cited work [47] also considered a threefold fluorinated TCNQ-derivative, in theory, but offers no experimental data on it, presumably, because such a 'F3TCNQ' compound does not seem to be commercially available or no synthesis route has been put forward to date.

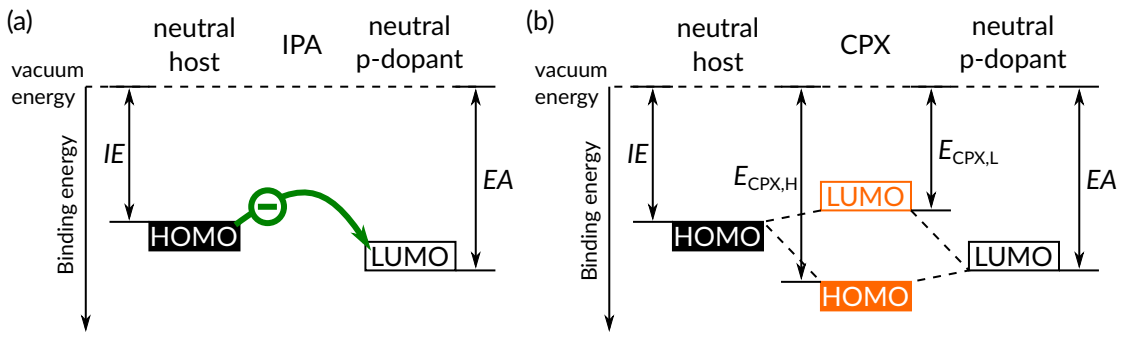


Figure 2.7: Energy levels in p-doping for (a) ion-pair (IPA) and (b) charge-transfer complex (CPX) formation.
Adapted from [7] (chapter 4; figure 4.1(a)) H. Hase, M. Berteau-Rainville, S. Charoughchi, W. Bodlos, E. Orgiu, and I. Salzmann, "Critical Dopant Concentrations Govern Integer and Fractional Charge-Transfer Phases in Doped P3HT," *Journal of Physics: Materials*, vol. 6, no. 1, p. 014004, Jan. 2023. Published 2023 by IOP Publishing under CC BY 4.0.

like P3HT exhibit intense peaks in the same region [146, 147], often rendering the dopant ring C=C modes ambiguous to identify (*cf.* figure C.5). Instead, the C≡N stretching modes around 2200 $cm^{-1}$ are more commonly employed [33, 34, 51–53, 148] despite being highly sensitive to intermolecular interactions subject to packing and polymorphism [53], adding a level of uncertainty to the interpretation of $\delta$. Notably, Haworth et al. [54] demonstrated in a theoretical study on the density functional theory level that $\nu_1$—not $\Delta\nu$—in $Li^+F4TCNQ^-$ severely shifts based on the placement of the $Li^+$ counterion. This general notion was employed in my master's thesis [1] and a subsequent publication [2]. There, P3HT-F4TCNQ thin-films were thermally annealed at increasing temperatures and a shift in $\nu_1$ from position $\nu_{1A} = 2192\,cm^{-1}$ to $\nu_{1B} = 2185\,cm^{-1}$ was observed; it was correlated with changes in structural data from GIXRD which led to the assignment of $\nu_{1A}$ to $F4TCNQ^{\bullet-}$ in a mixed stack with the CP backbone and $\nu_{1B}$ for the dopant residing in the side-chain region. Ever since, new studies approached the $\nu_{1A}$–$\nu_{1B}$ shift with different interpretations [58–60] which are discussed in the light of present data in section 4.4.1.

### 2.3.3 Charge-Transfer Complex Formation

Doping the P3HT COM-equivalent 4T with the aforementioned FxTCNQ series consistently yields $\delta \approx 1/4$ [34]. Such fractional charge transfer is indicative of ground-state charge-transfer complex (CPX) formation where frontier-orbital overlap between host and dopant leads to their rehybridization into a doubly occupied, bonding supramolecular orbital and an empty anti-bonding one which form the respective HOMO and LUMO of the CPX (see figure 2.7(b)). Following a Hückel-like approach, the energy levels of the CPX HOMO $E_{CPX,H}$ and LUMO $E_{CPX,L}$, in the p-doping scenario, can be estimated as:

$$E_{CPX,H/L} = \frac{IE + EA}{2} \pm \sqrt{(IE - EA)^2 + 4\beta^2} \tag{2.2}$$

from the host $IE$, the p-dopant $EA$, and the resonance integral $\beta$; the latter is descriptive of the electronic coupling between host HOMO and dopant LUMO and increases in value the greater the nodal structure of these orbitals match up [33, 50]. Note that a fully analogous n-type scenario has been proposed as well [38]. An important takeaway from equation 2.2 is that CPX formation contributes to the binding energy between host and dopant.

Besides intermediate shifts between the $\nu_0$ and $\nu_1$ peak positions of vibrational fingerprint bands, CPX formation can also be indicated by electronic transitions between the rehybridized frontier molecular orbitals of the CPX (*cf.* figure 2.7). The respective UV-vis/NIR features occur in the fundamental gap of the pristine materials but typically differ from those assigned to IPA formation. However, these optical transitions are specific to the host-dopant combination and their interpretation should be independently supported by other experimental techniques such as the vibrational band-shifts in FTIR (taking into account their limitations mentioned above). Notably, for $EA < IE$ the low-energy onset of the CPX transitions shifts to higher energy for lower dopant $EA$ as the $E_{\mathrm{CPX,H}}$–$E_{\mathrm{CPX,L}}$ gap increases according to equation 2.2 [34, 50]. Here, chapter 4 provides new assignments of optical CPX features for the host-dopant combinations of P3HT-F2TCNQ, -FTCNQ, and -TCNQ.

CPX formation is commonly seen as detrimental to the doping efficiency. In IPA formation, a charge carrier is directly introduced on the host molecule. In contrast, the contribution of $\beta$ in CPX formation adds a significant energy barrier (e.g. 0.42 eV for F4TCNQ-doped 4T [34]) to charge-carrier generation. Framed from a DOS perspective, considering the CPX states embedded into the OSC DOS and an occupation according to Fermi-Dirac statistics, the CPX LUMO is at a lower binding energy than the pristine dopant LUMO (which is the case of $\beta = 0$, i.e., when CPX formation had not occurred), thus, fewer states are ionized and fewer mobile charge carriers can be generated. However, apart from its detrimental role in electrical doping *per se*, recent studies found that CPX formation can potentially serve other purposes for OSCs: optimizing CPX-IPA ratios showed improved performance of hole transport layers in OLEDs [35] as well as stabilization of thermoelectric function under thermal stress [36]. All of these observations demonstrate that being able to control CPX occurrence is of high application-related relevance, be it for increasing the doping efficiency by suppressing CPX formation or for additional functionality.

### 2.3.4 Ionization and Complex Formation Regarding the Density of States

A comprehensive view of the changes to the DOS in both CPX and IPA cases was proposed by Salzmann et al. [33] and is illustrated in figure 2.8. This view (i) considers the aforementioned fact that the DOS follows a Gaussian distribution due to the energetic disorder inherent to OSCs [62, 107] and (ii) included the reorganization energy $\lambda$ (*cf.* figure 2.5) alongside $U_1$ and $U_2$ as the Hubbard $U$ (*cf.* figure 2.5(b)) for electron donor and acceptor, i.e. host/dopant and dopant/host in the p-/n-doping scenario, respectively [119]. The left side of figure 2.8 depicts the CPX with $E_{\mathrm{CPX,H}}$ of higher and $E_{\mathrm{CPX,L}}$ of lower binding

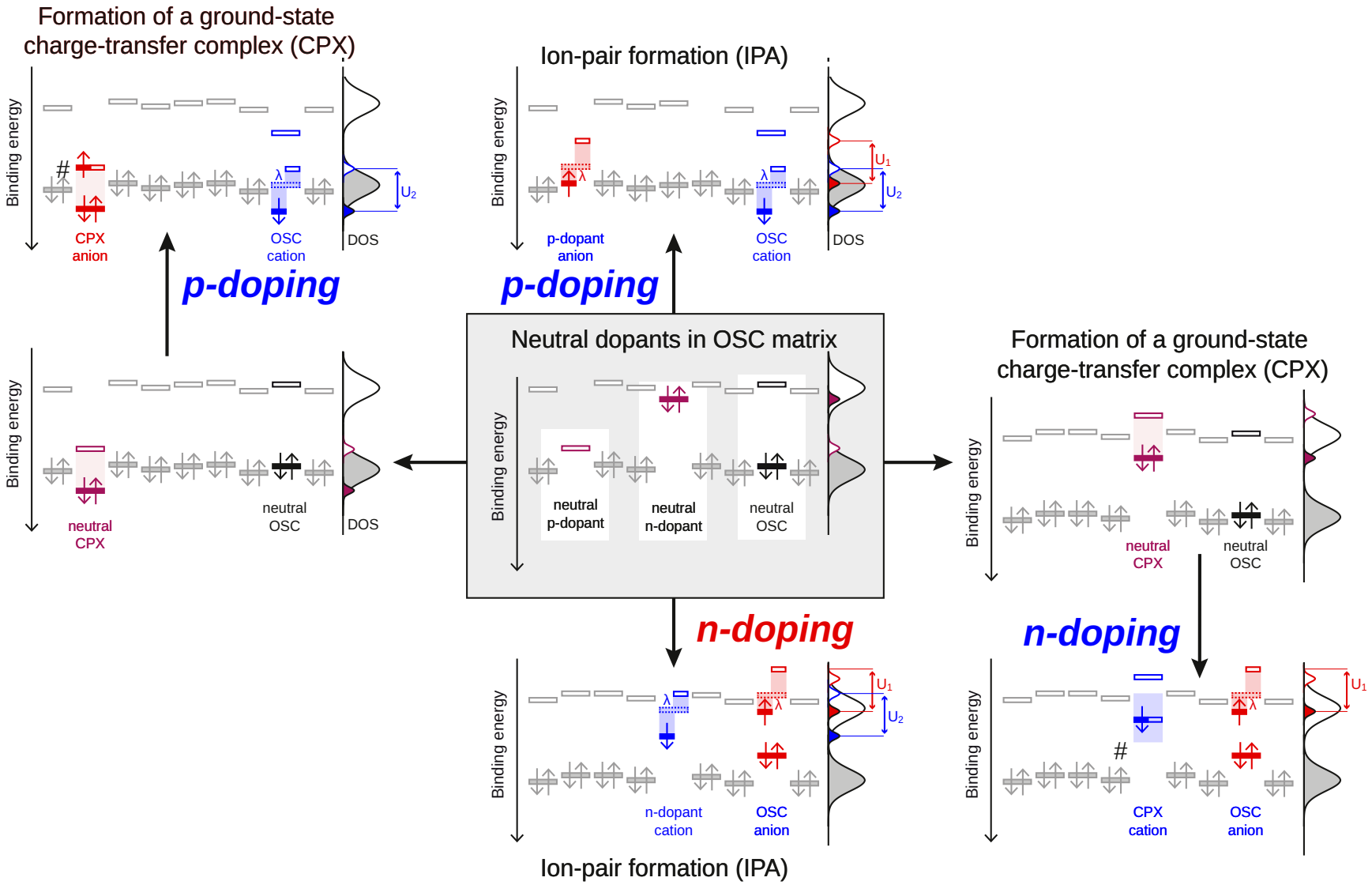


Figure 2.8: Energy levels and the corresponding DOS upon molecular p-/n-doping for the scenarios of IPA *versus* CPX formation and the subsequent ionization of the latter; noted are the reorganization energy $\lambda$ and the Hubbard $U$ of the electron acceptor $U_1$ and donor $U_2$ of each scenario except the ionized state of the CPX as its levels are yet to be observed and, here, are approximated by those of the neutral species (marked with #).
From [33] I. Salzmann, G. Heimel, M. Oehzelt, S. Winkler, and N. Koch, "Molecular Electrical Doping of Organic Semiconductors: Fundamental Mechanisms and Emerging Dopant Design Rules," *Accounts of Chemical Research*, vol. 49, no. 3, pp. 370–378, Mar. 2016. Copyright 2016 American Chemical Society.

energy than the $IE$ of the neutral OSC levels. Therefore, the CPX in the pristine-host matrix provides a doubly occupied level below the transport manifold and an empty one above it. Then the top left part of the figure shows the situation upon charge transfer between the CPX and a pristine-host matrix level as a precondition to mobile charge-carrier (hole) generation; note that the energy levels of the ionized CPX have not been experimentally observed to date [34, 50] and the figure represents energy-level positions of neutral CPX (marked by #), *en lieu*. The right side of figure then illustrates the n-doping situation in analogy. Top and bottom center depict p-type and n-type IPA formation, respectively, with splitting of the singly occupied levels as proposed by Winkler et al. [119] (*cf*. figure 2.5(b)).

## 2.4 Structural Aspects of Doping Organic Semiconductors

The high doping ratios in the order of % needed for optimal conductivity in molecular doping of OSCs [33, 34] constitute a significant disturbance of packing of crystalline host materials which can play out detrimentally to charge-carrier mobility. However, the introduction of molecular dopants does not necessarily have to be seen as a disturbance to an otherwise crystalline order. Indeed, calculations suggest that doping-induced disorder may as well replace intrinsic disorder in OSCs, in general [149] and doping was found to increase order in largely amorphous regio-random (rra) P3HT [150].

The latter, in comparison with regio-regular (rr) P3HT, offers a rewarding system to investigate effects of crystalline *versus* amorphous phases. In rr-P3HT, all repeat units are (ideally) only found in head-to-tail orientation while rra-P3HT exhibits a random series of head-to-head, head-to-tail, and tail-to-tail alignments [151, 152].[§] As a result, in otherwise identically doped films, rr-P3HT yields significantly higher doping efficiency than rra-P3HT which, firstly, is attributed to increased formation of amorphous phases in rra-P3HT which shortens the effective conjugation length and inhibits hole delocalization [153]. Further, CV data suggests that the $IE$ of rra-P3HT is about 0.3 eV higher than that of rr-P3HT [76] turning IPA formation energetically less favorable for rra-P3HT and, as has been suggested [49], making F4TCNQ doping turn to CPX formation, instead. In general, rra-P3HT is seen as a valid approximation to amorphous regions of rr-P3HT [154], hence, differences observed between these P3HT variants are commonly seen as general effects of varying degrees of crystallinity.

As mentioned before, CPX formation hinders mobile charge-carrier generation since, through rehybridization, it replaces the electron-attractive LUMO of a strong dopant with the CPX LUMO that offers lower $EA$. Its competition against IPA formation results in significantly lower doping efficiency in OSCs compared to ISCs. To offer a CPX LUMO of stronger $EA$, the resonance integral $\beta$ is key as it governs the energy-level splitting beyond the energy difference between host $IE$ and dopant $EA$ [34, 38, 50, 145]. $\beta$ depends on the mutual wavefunction overlap and, therefore, the host-dopant spatial arrangement, i.e. the microstructure. When the conjugated cores of the host and dopant molecules are

[§]More generally, repeat units in rra-polymers are made up of different isomers but in rr-polymers, ideally, only of one isomer. Pragmatically, rr-polymers are those where *practically* all repeat units are the same isomer, e.g., 93% in the rr-P3HT batch employed in this thesis.

of similar dimension, mixed crystal structures are likely to grow [155]. E.g., 1:1 FxTCNQ-doped 2,7-didecyl[1]benzothieno[3,2-b][1]benzothiophene (known as C10-BTBT) forms co-facial stacks with the dopant, exhibiting great frontier-orbital overlap and $\beta \approx 0.5\,\mathrm{eV}$ [50]; this scenario is akin to FxTCNQ-doped 4T [34]. Note, that this overlap is further subject to matching nodal structures along the molecular planes of host and dopant—a mismatch would reduce $\beta$ (*vide supra*: section 2.3.3). A commonly mentioned strategy to suppress CPX formation is the synthesis of novel dopants that sterically protect their conjugated core, inhibiting frontier orbital overlap [33, 156, 157]. One publication [8] that I became involved with (see List of Associated Works for details), features the design, synthesis, and characterization of a dopant based on a cyclopropane core, shielded by three peripheral perfluorophenyl rings; study [7] (chapter 4) serves to reference this novel dopant against F2TCNQ and F4TCNQ as dopants without steric protection of the conjugated core. Finally, CPX formation curbs doping efficiency to such an extent, that it was recently suggested to even introduce structural defects into crystalline materials to suppress it [40].

A striking observation, unchallenged until recently, was that CPs of sufficiently low $IE$ tend to always undergo IPA formation [33, 124, 158, 159] while numerous examples for CPX formation are found with COMs [33, 34, 38, 50, 50, 160]. However, both phenomena were simultaneously observed in F4TCNQ-doped thiophene-based copolymers where the reason for CPX formation was stated to be the local interaction of the dopants with the quinoxaline units of the CP [161]. Moreover, Jacobs et al. [39] created distinct IPA and CPX polymorphs of F4TCNQ-doped P3HT through changes in the deposition protocol. Films prepared from a common solution that was heated to 60°C but then spin-coated at ambient temperature, yielded the commonly known IPA phenomenology [2, 34, 158, 162]; keeping solution, pipette tips, and substrates constantly at 80°C until the film was deposited, created a CPX-only system as evidenced by optical and vibrational absorption; the polymorphs' distinct crystal structures were observed using GIXRD. As P3HT-F4TCNQ aggregates readily form in solution, the study explains its observation to result from keeping the solute dissolved until meeting the substrate, thus, enabling the compounds to form a more ordered film—featuring a dense CPX polymorph—that would be disturbed if pre-aggregation had occurred [39]. Here, such a CPX polymorph alongside simultaneous IPA formation is observed without the use of this special preparation protocol in the study [7] presented in chapter 4; its investigation leads to the hypothesis that this CPX polymorph is conditional on the provision of a certain host-dopant stoichiometry at which CPX formation, as a broader collective phenomenon, becomes energetically more favorable than IPA formation. In that light, the additional thermal energy Jacobs et al. provided during film formation might have allowed for host and dopant molecules to order into blends within the film that locally achieve such stoichiometry.

It goes to show, that the host-dopant spatial arrangement is critical to the doping process and, since CPX formation heavily influences doping efficiency, structural investigations are crucial to understanding doping in OSCs.

# Chapter 3

# Experimental Methods

While experimental details are provided within the studies featured in this thesis, i.e. in sections 4.2 and 5.2, the present chapter aims to equip the reader with the basic principles behind the techniques. Further, it reports on the solutions applied for technical issues encountered during the experiments conducted for this thesis and provides details on how experimental data was processed. First and foremost, optical absorption in the ultraviolet, visible light, and the near-infrared (UV-vis/NIR; section 3.1) and Fourier-transform infrared spectroscopy (FTIR; section 3.2) are introduced since they prominently serve as the means to identify dopant mechanisms at work in a given sample. They are followed by cyclic voltammetry (CV; section 3.3) and grazing-incidence x-ray diffraction (GIXRD; section 3.4) as techniques that help elucidate the energetic influences and structural consequences, respectively, of the observed doping behavior. Finally, to demonstrate the application-relevance of the latter, thin-film conductivities were determined. The process is explained in section 3.5 together with a follow-up on atomic force microscopy (AFM; section 3.6) which was used to provide sample dimensions (film thickness) required for the conductivity calculations.

## 3.1 Optical Absorption Spectroscopy (UV-vis/NIR)

Throughout the investigations featured in this thesis, the first experimental step has always been the assessment of optical absorption features in near-infrared (NIR; 0.41–1.6 eV, 3000–800 nm), visible light (vis; 1.6–3.1 eV, 800–400 nm), and ultraviolet (UV; near- to far-UV: 3.1–10 eV. 400–120 nm).* Especially, but not exclusively, NIR absorption features offer a valuable first impression on the doping phenomena at work (*cf.* section 2.3.1), most relevant to this thesis. The instruments employed here are two Cary 5000, one produced by Agilent Technologies (for chapter 5) and the other made by its predecessor company, Varian (for chapters 4 and 5), which can measure over a range of 0.38-7.1 eV (3300–180 nm). Since the machine by Agilent Technologies was less-readily

*The given ranges merely serve as orientations since many different definitions and standards exist, especially, for the limits of visible light, naturally deviating as visual perception varies between human individuals. Therefore, e.g. the 800 nm NIR-vis border was chosen as it is fairly commonly used in spectrometer configurations.

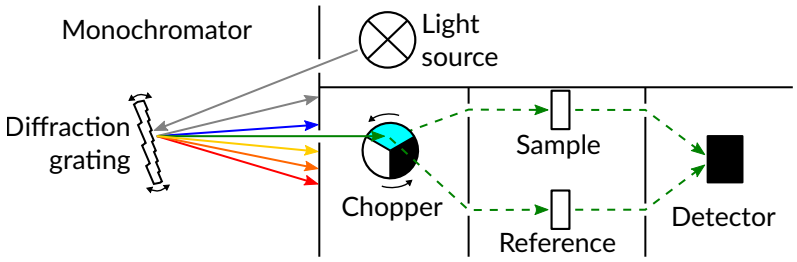


Figure 3.1: Typical double-beam configuration for the measurement of optical absorbance; drawn in a compact, simplified way thus missing: filters, additional monochromator gratings, variable slits for aperture control, and mirrors for collimation, focusing, or path-folding.

available to me, I only used it to proceed with my research while performing recurring troubleshooting and, eventually, repairs on the instrument by Varian.

### 3.1.1 Setup Fundamentals

In commonly used spectrometer setups, like the one employed here, *absorbance* is measured as a proxy to the investigated *absorption*. Absorbance $A$ is obtained from the ratio between incident beam intensity $I_0$ and the transmitted intensity $I$:

$$A = \log_{10}\left(\frac{I_0}{I}\right) \tag{3.1}$$

Absorbance only captures the attenuation in transmission (the ratio $I/I_0$ is the transmittance) and, therefore, it offers no distinction between absorption and reflection (including scattering) effects. Absorption can be isolated through use of an integrating sphere (sometimes called 'Ulbricht sphere'). A case where such a sphere could become essential, is demonstrated by the '100%' spectra of 2,3,5,6-tetrafluoro-7,7,8,8-tetracyanoquinodimethane (F4TCNQ), 2,5-difluoro-7,7,8,8-tetracyanoquinodimethane (F2TCNQ), 2-fluoro-7,7,8,8-tetracyanoquinodimethane (FTCNQ), and 7,7,8,8-tetracyanoquinodimethane (TCNQ) in figure 4.2, where a broad absorbance background-feature obscures the optical absorption onset between 2 and 3 eV. This broad feature is likely to be associated with Mie scattering from the adsorbate forming a granular structure—instead of a smooth film—with granules of varying dimensions close to the affected wavelengths [163], as the bright yet partially powdery-opaque appearance of the respective samples suggests. However, cost and effort to provide and install an integrating sphere to the available spectrometer was not justified here, since these spectra serve only as qualitative reference in chapter 4 because, e.g. the peak around 2.9 eV for F4TCNQ [164] can still be made out; as well, because any absorption features were sufficiently distinguishable in the rest of the data.

All measurement were done in double-beam mode, i.e. a three-section chopper periodically directs the incident beam either towards the sample (mirrored section), towards a reference (cut-out section), or blocks it to provide time to move to the next wavelength step in a scan (matte black section); the paths of sample and reference beams lead to

the same detector where they are recorded. A schematic depiction of this beam path is provided in figure 3.1.

### 3.1.2 Inert-Atmosphere Sample Holder

To enable measurements of samples in an inert atmosphere, a sample holder (figure 3.2 top) was designed by Melissa Berteau-Rainville and Eric Ferguson during a Concordia Undergraduate Summer Research Award (CUSRA) internship with our group, partly, under my supervision, and manufactured by the Science Technical Center of Concordia University. This sample holder consists of an aluminum base plate with long edges cut to form rails, which fit into the slot that the spectrometer provides for standard glass-slide sample holders. It has an inset quartz glass window that is sealed up by epoxy at its contact areas with the plate. A $1.0\,\mathrm{cm} \times 1.0\,\mathrm{cm} \times 0.5\,\mathrm{mm}$ sample can be placed on top of the window opening; it is secured by a 3D-printed plastic brace with only its inner bevels touching the edges of the substrate as to ideally avoid any contamination of and by the film deposited on it. The setup explained so far was used for work in ambient conditions. When working in inert atmosphere in a glovebox, the base plate can be sealed with an aluminum compartment using a flat gasket cut from a rubber sheet between them. The compartment, similarly to the base plate, holds a quartz glass window to allow the spectrometer beam to pass through. After its employment in several measurements for various projects throughout a year, some shortcomings of this design became clear to us. To address them, I devised a new sample holder with the help of William Chicoine of the Science Technical Center. However, due to a series of unfortunate events—including the COVID-19 pandemic—this new version could not be manufactured until after all spectroscopy measurements for this thesis had already concluded, and the old design was used, exclusively.

The improved sample holder takes the concept of one that I was provided with as a master student in the group of Prof. Norbert Koch at Humboldt-Universität zu Berlin, Germany, and adapts it to the slot-based system of the Cary 5000. Here, the sample is clamped by flexible metals strips to a holder that is perpendicularly attached to the base plate. The latter has a trench to accommodate a KF-25 o-ring to solve the foremost shortcoming of the previous design, namely, that the gasket cut from a rubber sheet may inhibit ambient gas diffusion only to some degree. Instead, KF o-rings are a proven method of sealing as they were developed for vacuum systems. That said, the previous design still provided vital—and apparently functional—sealing to record spectra of poly(3-hexylthiophene-2,5-diyl) (P3HT) doped with tris(pentafluorophenyl)borane in the work of Melissa Berteau-Rainville, where a marked difference between samples handled entirely under inert atmosphere and in ambient conditions were observed (data yet to be published).

As the sample is now oriented perpendicular to the base plate, the top-compartment now holds both windows. This solves the problem of the previous design where aluminum shavings would fall on the window while fixing the sample brace to the base plate with the bolts of the brace creating ever new shavings; bolts of softer material were, in turn, shaved by the base plate; the initially used bolt-less, friction-based sample brace of the previous design suffered from instability. The rails to fit the spectrometer slots are

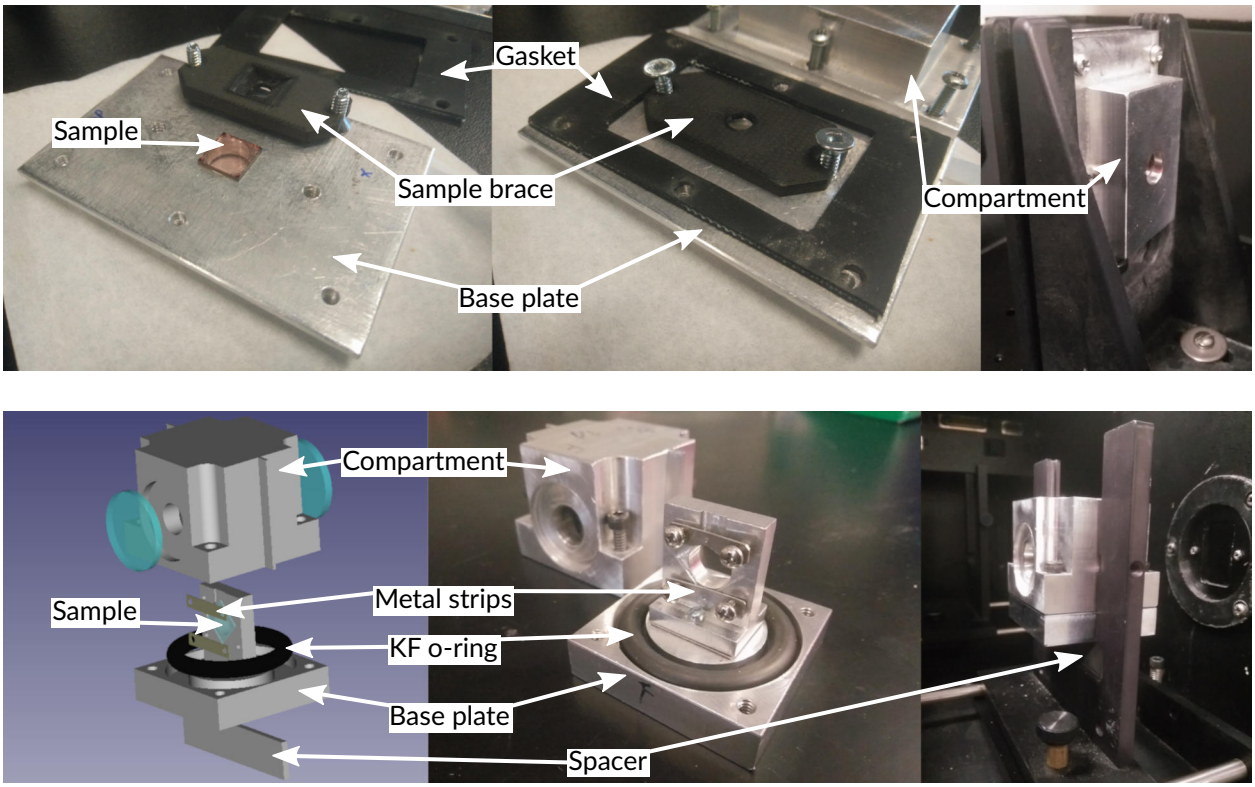


Figure 3.2: Sealable spectroscopy sample holders for measurements in inert atmosphere. Top: version as used for this thesis. Bottom: version as devised for this thesis but not manufactured until after all spectra were recorded.

now found at the compartment and they were made thinner to additionally accommodate each a bent metal strip that acts as a spring to ensure that the holder sits flush with the slot. This was done to reduce differences between measurements resulting from varied path-lengths through both windows and the sample as a consequence of varied angles with respect to the beam. Finally, a rectangular aluminum plate serves as a spacer to lift the holder into the beam path; while the height of the holder is adjustable through bolts in the spectrometer, the elevation range of this adjustment is limited.

### 3.1.3 Sample Spectra Acquisition and Treatment

In every measurement session, to remove features related to setup and substrate from the sample spectra, a baseline spectrum had been recorded that uses the same setup as the sample measurement except for the substrate being in the condition it has after cleaning and before film deposition. The acquisition software automatically subtracts the prerecorded baseline absorbance while recording the sample spectrum (i.e. sample transmission is divided by baseline transmission). This approach is the same as in single-beam mode which, however, would have the problem that it is more prone to artifact creation from fluctuations in irradiance from the lamp, stray light due to unaccounted mechanical slackness in the sample-holder system, and electronic noise in the detector signal. This

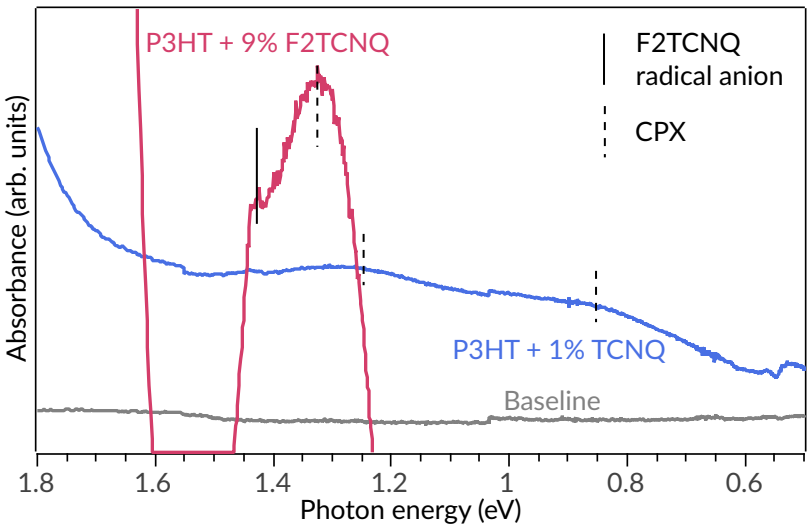


Figure 3.3: Comparison of the baseline with the smallest UV-vis/NIR features analyzed in this thesis, i.e. the radical anion feature in P3HT doped with 9% F2TCNQ and the charge-transfer complex (CPX) features of P3HT doped with 1% TCNQ (*cf.* figure 4.2). The P3HT + 9% F2TCNQ spectrum is shifted along the ordinate to focus on the radical anion feature; all spectra are on the same absorbance scale.

problem can be reduced by the double-beam geometry because reference and sample paths are measured at virtually the same time. Ideally, the reference path would have an identical sample holder holding a clean substrate to capture how the effects of the fluctuations are, in turn, affected by holder and substrate as additional components with their own response to the aforementioned fluctuation sources. (Note, this does not replace the need for baseline subtraction as the reference path is only up to some degree identical to the sample beam path.) However, here, the expense of manufacturing an identical sample holder (*vide supra*) was spared as baseline tests, i.e. measuring an empty substrate as a sample after recording the baseline, showed insignificant noise levels and measurement artifacts *versus* the magnitude of the investigated absorption peaks (see figure 3.3). An important improvement over the spectra acquired for my master's thesis [1], was the usage of shorter acquisition times causing less fluctuation between the recording of absorbance at each wavelength step of the spectrum, thus, increasing the signal-to-noise ratio.

UV-vis/NIR spectrometers commonly have separate lamps, diffraction gratings, and detectors to serve different spectral ranges. The Cary 5000 comprises two sets of gratings as well as a photomultiplier tube (PMT) and a PbS photocell as detectors for the UV-vis and NIR regions, respectively. Although automated and contained in a single instrument, this constitutes a significant alteration of the setup and the changeover from the NIR to the vis range must be seen as an interruption in the otherwise virtually continuous scan. (Hence, the choice to write 'UV-vis/NIR' with a slash to signify that effectively two different measurements are merged within one experiment.) This can become visible in the spectrum as both detector and grating changes can produce a sudden increase or

decrease in absorbance after passing their changeover wavelengths in the scan. Such a 'step' in the spectrum can potentially be mistaken for, e.g., faint radical anion peaks of the TCNQ-derivatives (*cf.* P3HT doped with 9% F2TCNQ in figure 4.2). Therefore, it is sensible to minimize the impact of the steps on the clarity of the spectrum by setting both changeovers to the same wavelength, here, 1.55 eV (800 nm); the latter is still close to the radical anion peaks at 1.45 and 1.63 eV (855 and 761 nm) [33, 34, 39, 122–124] but this choice constitutes a compromise with the increased noise levels when moving either or both changeover points past one of the peaks. The NIR-to-vis step is removed from the spectra presented in this thesis by linearly shifting the UV-vis absorbance curve to align the absorbance value at its highest wavelength with the value at the lowest wavelength of the NIR range—but this can be done *vice versa*. Note that this method may suffice for a qualitative assessments but precise quantification and comparison of absorbance values between UV-vis- and NIR-region features should be done under consideration that it is unclear which absorbance value at the step—that of the vis or the NIR region—is more accurate. Finally, another step could be observed when the instrument switches from its quartz halogen lamp to the deuterium lamp that is needed to reach the lowest wavelengths that the Cary 5000 is capable of detecting. However, the studies, here, did not demand investigations above 5.4 eV (<230 nm) and higher energies were avoided to prevent radiation damage to the samples in the ultraviolet; in fact, all spectra, here, are cut above 3.5 eV (<350 nm) to focus on relevant absorption features, only. Therefore, as spectroscopy at this upper energy-limit still worked reliably with the halogen lamp, the deuterium lamp was not employed to avoid the creation of another step in the spectra.

## 3.2 Fourier-Transform Infrared Spectroscopy (FTIR)

Complementary to UV-vis/NIR, the next-most important method employed for this thesis is Fourier-transform infrared spectroscopy (FTIR), here, with a focus on the mid-infrared range (MIR; 0.025–0.41 eV, 50000–3000 nm, 200–3300 $cm^{-1}$).[†] Careful merging of the FTIR and UV-vis/NIR spectra can be helpful in resolving the low-energy flank of doping-related electronic transition features around 4000 $cm^{-1}$ (0.50 eV) as, e.g. for the peak labelled 'A' in F4TCNQ-doped 'h10T' (spectrum figure 5.2) as discussed in section 5.3.1. Further, the MIR hosts a plethora of vibrational fingerprint bands like the C≡N and ring C=C stretching modes of TCNQ derivatives around 2200 and 1500 $cm^{-1}$, respectively, as mentioned in section 2.3.2. Their positions are helpful in determining the degree of charge transfer—an indicator of ion-pair (IPA) or ground-state charge-transfer complex (CPX) formation—sometimes complementary to ambiguous UV-vis/NIR features, but also being complemented by UV-vis/NIR data due to other conditions affecting these band position, as explained in section 2.3.2 and discussed in sections 4.3.2 and 4.4.1.

The employed Thermo Scientific (former Thermo Electron) Nicolet 6700 FT-IR Spectrometer was set up with an EverGlo glowbar infrared (IR) source, a KBr beam splitter, and an MCT-A liquid nitrogen-cooled HgCdTe detector which, in this combination, al-

[†]The spectrometer provides wavenumber values in $cm^{-1}$ (*vide infra*) which is also the common unit for vibrational bands in literature. Here, it is only converted to energy in eV when FTIR is used to extend UV-vis/NIR spectra while wavelengths are given for comparison with section 3.1.

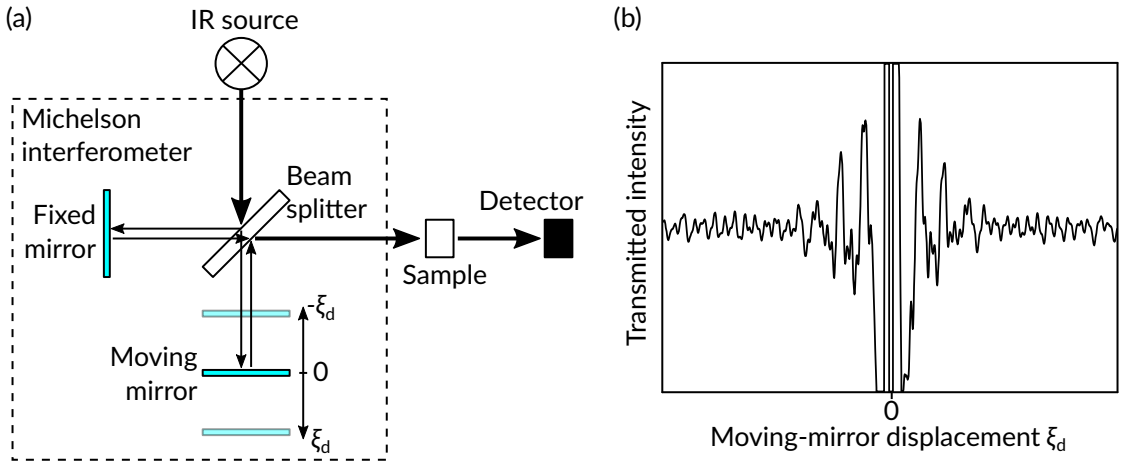


Figure 3.4: (a) Typical setup of a Fourier-transform infrared spectrometer in transmission configuration, employing a Michelson interferometer; drawn in a compact, simplified way thus missing: filters, aperture control, and mirrors for collimation, focusing, or path-folding; some spectrometers employ laser-interferometry in parallel to the depicted beam path for mirror positioning, the components of which are also not depicted. (b) Conceptual interferogram example; the peaks around the center burst are cut off for the sake of the visibility of the several orders of magnitude smaller signal details further away from the burst.

lows for optimal operation in the range of 650–4000 $cm^{-1}$ (0.081–0.50 eV) in transmission mode (range recommended as reliable by the acquisition software, Omnic 9 by Thermo Scientific; 400–7400 $cm^{-1}$ is the maximum range defined by the components). To minimize the occurrence of $CO_2$ and $H_2O$ peaks in the spectra, the instrument was periodically purged every 5 min from a purge-gas generator whereas 3 cycles showed sufficient effect for the spectra recorded, here. To enable measurements in inert atmosphere, sealable sample holders identical to the ones introduced in section 3.1.2 were manufactured with KBr-crystal windows (instead of quartz-glass) for transparency in MIR.

### 3.2.1 Setup Fundamentals

At the heart of FTIR lies the interferometer and, while a variety of other geometries can be found in various spectrometers, its workings are here exemplified on the Michelson interferometer (see figure 3.4(a)). This geometry consists of a beam splitter at 45° angle to the incident beam, a fixed mirror perpendicular to the beam reflected off the beam splitter, and a moving mirror perpendicular to the beam transmitted through the beam splitter. The moving-mirror displacement $\xi_d$, here, is defined with $\xi_d = 0$ being the position where the moving mirror has the same distance to the beam splitter as the fixed one. The beam parts reflected at the mirrors reunite again at the beam splitter and are transmitted and reflected off it, again, forming one beam path back to the source and, perpendicular to the fixed mirror, one that is passed towards the detector (passing through the sample chamber).

The portion that is directed to the detector *versus* that directed back to the source is depending on the phase differences after the second beam-splitter pass. With $\xi_d = 0$, the phase shifts at the beam splitter (90° for reflection, zero for transmission) add up such that the beam passed towards the detector results from fully constructive interference of the fixed and moving mirror-reflected beams, while the beam passed towards the source is effectively extinguished through destructive interference. When the moving mirror deviates from this position by $\xi_d$, the path difference $\xi = 2\xi_d$ effectively produces another phase shift. For a given wavelength $\lambda$ this means that increasing $|\xi|$ to $\lambda/2$ adds a 180° shift, leading to the reverse situation where all beam power is redirected at the source and none at the detector; displacing the moving mirror such that $|\xi| = \lambda$ then moves the beam power—for a specific $\lambda$—back to the detector.

Recording the intensity $I_\xi$ for continuous $\xi$ provides an *interferogram* which, assuming a monochromatic source for now, takes the form of a cosine with a wavelength of $\lambda/2$ and an offset[‡] $I_{const}$ aligning the otherwise negative cosine minima to $I = 0$. In IR spectroscopy, the reciprocal of the period is more commonly used, i.e. the number of waves per unit length, or in short, the wavenumber $\nu$; virtually always provided in $cm^{-1}$ which likely established itself because the reciprocal of the maximal $\xi$ in cm yields the spectral resolution in $cm^{-1}$ [165]. With $I_\nu$ as the intensity for the given $\nu$ as produced by the IR source and affected by mirror and beam-splitter efficiencies, any sample absorbance (if applicable), and detector sensitivity, $I_\xi$ becomes:

$$I_\xi(\xi) = I_{const} + I_\nu(\nu)\cos(2\pi\nu\xi) \tag{3.2}$$

Mathematically, $I_\nu$ represents the Fourier transformation (FT) of $I'_\xi = I_\xi - I_{const}$. For a non-monochromatic, continuous source, the interferogram becomes more complicated (see example in figure 3.4(b)) since each wavenumber obeys equation 3.2. Hence, $I'_\xi$ needs to be integrated over all wavenumbers:

$$I'_\xi(\xi) = \int_{-\infty}^{\infty} I_\nu(\nu)\cos(2\pi\nu\xi)\,d\nu \tag{3.3}$$

which forms a cosine FT pair with:

$$I_\nu(\nu) = \int_{-\infty}^{\infty} I'_\xi(\xi)\cos(2\pi\nu\xi)\,d\xi \tag{3.4}$$

This, in turn, can be re-written as follows due to $I'_\xi(\xi)$ being an even function [165], providing intensities for only the physically sensible, positive wavenumber values:

$$I_\nu(\nu) = 2\int_{0}^{\infty} I'_\xi(\xi)\cos(2\pi\nu\xi)\,d\xi \tag{3.5}$$

Both experimental impossibilities of infinitely long beam path difference $\xi$ and infinitesimally small sampling $d\xi$ are resolution- and range-limiting factors, respectively.

Regarding the range, the numerical counter part to the analytical $d\xi$, i.e. the sampling interval $\Delta\xi$, needs to become smaller to sample waves in the interferogram of shorter

[‡]In technical terms, $I_{const}$ would represent the dark current of the detector.

wavelength. This is due to the Nyquist theorem which states that, in present terms, $\Delta\xi \leq \lambda/2$ is necessary to resolve a sinusoidal wave with wavelength $\lambda$.

To mathematically realize the limitation of $\xi$, one can introduce a truncation function $D_\xi(\xi)$ which is unity between the maximal path differences $-\xi_{\max}$ and $\xi_{\max}$, and zero outside of it:

$$D_\xi(\xi) = \begin{cases} 1 & \text{for } |\xi| \leq \xi_{\max} \\ 0 & \text{for } |\xi| > \xi_{\max} \end{cases} \tag{3.6}$$

into equation 3.4:

$$I_\nu(\nu) = \int_{-\infty}^{\infty} D_\xi(\xi) I'_\xi(\xi) \cos(2\pi\nu\xi)\, d\xi \tag{3.7}$$

The FT of multiplied functions is the convolution of the FTs of the separate functions. The FT of $D_\xi(\xi)$ alone is a sinc function $D_\nu(\nu)$ with a full width at half maximum (FWHM) of $0.605/\xi_{\max}$:

$$D_\nu(\nu) = 2\xi_{\max} \frac{\sin(2\pi\nu\xi_{\max})}{2\pi\nu\xi_{\max}} = 2\xi_{\max}\mathrm{sinc}(2\pi\nu\xi_{\max}) \tag{3.8}$$

Each wavenumber involved in the non-truncated interferogram yields a discrete data point on the spectrum. Such a discrete point, when convoluted with any function, reproduces the very function but centered at the data point and scaled by its amplitude. Hence, with an interferogram truncated by $D_\xi(\xi)$, all the discrete wavenumbers become sinc-function distributions with a FWHM of $0.605/\xi_{\max}$; the FT of a truncation function is therefore called the *instrument line shape*. If the FWHM becomes too large, i.e. if $\xi_{\max}$ becomes too small, the two distributions can overlap such that they become indistinguishable, appearing as a single peak, ultimately, marking the resolution limit. Since the sinc function produces smaller side peaks that can be irritating in the spectral analysis, the interferogram commonly is *apodized*, i.e. it is further truncated numerically by a function whose FT forms negligible or no side peaks at all; of course, further truncation comes at the cost of resolution.

### 3.2.2 Advantages of FTIR

The rapid advancement of computer technology along with the development of fast FT algorithms in the second half of the 20th century eliminated the FT calculation effort as the major downside to FTIR. Today, practically all modern MIR spectroscopy is done with FTIR due to three distinct operational advantages over monochromator-based spectrometers like the one explained in section 3.1.1. Although setups based on quantum-cascade lasers are currently discussed as a FTIR-successor technology due to, in part, superior spectral resolution, broad enough spectral ranges are not (yet) available to fully replace FTIR spectrometers as a laboratory staple [166, 167]. Hence, the advantages mentioned here are only referring to the comparison with monochromator-based spectrometers.

The simultaneous measurement of spectral information from all wavelengths constitutes Fellgett's advantage (the multiplex advantage) [165]. This circumstance yields that a grating spectrometer needs up to $M$ times longer to achieve a signal-to-noise ratio as high as for a FT spectrometer when considering the same optical throughput and efficiency, and the same amount $M$ of resolution elements $\Delta\nu$ [165]. However, this advantage

is cancelled for shot noise-sensitive detectors like PMTs which deliver the feasibly best result for UV-vis spectra, hence, the FT approach is usually limited to IR spectroscopy (among some other applications).

Second, Jacquinot's advantage (the throughput advantage) lies with the potential of shorter integration times through significantly fewer losses by the mirrors and beam splitters in interferometers *versus* the mirrors, gratings, and slits in a grating monochromator [165].

Finally, Connes' advantage recognizes the superior ability of laser-interferometry to determine mirror position and alignment in an interferometer [165], which can be done in parallel with the actual sample measurements while grating positions need to be calibrated prior to the measurement and then need to rely on the precision of the motors moving the gratings. Particularly, due to the interferometer mirrors needing to be perpendicular to the primary beam, anyway, the laser beam can be passed in parallel to the latter, then be blocked from the primary detector and redirected to a separate one, as done in the Thermo Scientific Nicolet 6700 FT-IR Spectrometer employed in this thesis. In contrast, as the beam of a narrow-wavelength calibration source would need to hit a grating at the same spot and angle as the same-wavelength part of the primary beam, the calibration beam could not be singled-out and used during a measurement; the calibration of the aforementioned Varian Cary 5000 UV-vis/NIR spectrometer had been part of setting up the instrument following the troubleshooting that I did frequently, and not a standard procedure in measurement preparations.

### 3.2.3 Sample Spectrum Acquisition and Treatment

The removal of non-sample features from the sample absorbance spectrum is done by subtraction of a background spectrum with a blank substrate in the sample holder, as explained for UV-vis/NIR in section 3.1.3. However, in contrast to the latter, the lack of a reference beam means that FTIR spectra are more susceptible to artifacts from fluctuations in source energy, stray radiation, beam intensity, and electronic noise. It is therefore advisable to record background spectra before and after; one has to be aware that this is to merely gauge any such fluctuations since both spectra still do not represent the situation *during* sample measurement. This leaves it up to the spectroscopist to decide upon the validity of any background subtraction, especially, regarding expected broad features of the sample itself and highlights the necessity to constantly evaluate data during data acquisition.

Within the scope of this thesis, this is particularly true for doping-related electronic transitions around 4000 $cm^{-1}$ (0.50 eV), e.g. the CPX peak in F4TCNQ-doped P3HT (*vide supra*) and the lowest-energy polaron transitions ('P1' in figure 2.6), whose low-energy flank can extend deep into the MIR range. To be able to identify the peaks instead of just the flanks of these bands, FTIR spectra were, here, converted from wavenumber to energy scale in eV and connected with UV-vis/NIR spectra, gaining the full feature shape. However, this procedure has to be done cautiously, not only, because of the fluctuation issue, but because of three fundamental differences between FTIR and UV-vis/NIR experiments: (i) different substrates employed due to their complementary transparency ranges, (ii) variation in sample film-thickness beyond the precision of the deposition pro-

tocol, and (iii) the instrument setup differing even more between FTIR and NIR than the UV-vis–*versus*–NIR case explained in section 3.1.3. Therefore, in addition to the alignment by a linear-shift along the ordinate, as done between UV-vis and NIR spectra, the FTIR spectrum also needs to be scaled such that the merged curves appear continuous. Note that this method should only be used for qualitative analysis as, again, some fluctuations are not accounted for in FTIR which could add a skewed baseline that, if subtle enough, goes unnoticed in the curve-merging process. Therefore, the qualitative nature of merging the spectra is remarked in the figure captions where relevant.

A skewed baseline, however, is less problematic when zooming in on the spectrum. All broader background features, regardless of origin, need to be removed to properly analyze much smaller and narrower peaks like, e.g. those originating from the C≡N and ring C=C stretching modes. To achieve this, it usually suffices to focus on the relevant range and subtract a linear or low-order polynomial function that has been fitted through points assumed to have no feature other than the background. This provides a virtually flat baseline to fit the narrower peaks and extract their parameters as, e.g. in figure C.4.

One type of artifacts that appears in the spectra of this thesis, are sinusoidal modulations, so-called *interference fringes*, owing to multiple internal reflections within the sample film and substrate. These fringes are often removed by deleting bursts in the interferogram that correspond to the frequency of the fringe in the spectrum, or, if the fringes have a high frequency, by applying a low-pass filter (i.e. greater $|\xi|$ are attenuated before FT). However, these easy-to-implement approaches have to be treated with much caution as the burst removal can destroy relevant spectral details that rely on interferogram information at the burst position, while the application of a low-pass filter effectively reduces the $\xi$ range and, subsequently, the $\nu$ resolution (*vide supra*). Any efforts for setup-wise or, alternatively, more sophisticated data-processing fringe removal as recently outlined by Konevskikh et al. [168] were not warranted for any data in the present thesis as the relevant features were still easily to be made out (*cf.* 100% TCNQ spectrum in figure 4.3). The next-most affordable strategy would have been the film deposition on the rough side of a single-side polished Si wafer to reduce the internal reflections causing the fringes. However, I was unable to test this idea due to material unavailability and time constraints. As of writing this thesis, such wafers had been purchased and Somaiyeh Charoughchi, a member of our research group, found signal throughput to be diminished to a point where the peaks of interest partially start to blend in with the background noise. Likely, this is a result of the beam being scattered at the unpolished surface, thus, having a smaller fraction of the beam directed at the detector, leading to less contrast between background and sample features. Therefore, using single-side polished wafers for fringe removal does not seem to be a feasible solution.

## 3.3 Cyclic Voltammetry (CV)

A common method to estimate the ionization energy $IE$ and electron affinity $EA$ of host and dopant materials in OSC research is to derive these quantities from redox potentials $V_{\text{redox}}$ measured by cyclic voltammetry (CV). Besides being a low-cost alternative to (inverse) photoelectron spectroscopy, it was recently shown that, empirically, it also

provides values better able to predict host-dopant ion-pair formation [48]—this finding is discussed in sections 4.3.5 and 4.4.2.

CV data presented in this thesis (voltammogramms in figure C.9) were either provided by Somaiyeh Charoughchi (F2TCNQ, FTCNQ, TCNQ), recorded in close collaboration with her (F4TCNQ, P3HT), or acquired by myself ('h*x*Ts'—full names in section 5.2). A CH Instruments CHI604d potentiostat was employed with a Pt-wire counter electrode, an Ag-wire pseudo-reference electrode, and 0.1 M tetrabutylammonium hexafluorophosphate as the electrolyte dissolved in acetonitrile. In the case of the TCNQ derivatives, a glassy carbon working electrode and a scan rate of 0.05 V/s were employed. For the h*x*T compounds, a Pt-disk working electrode and dichloromethane as the solvent were used instead, due to electrode's availability in the lab and the orthogonal solubility to the TCNQ cases. For both P3HT and h10T, the compound was spin-coated onto an indium-tin-oxide (ITO)-coated glass slide, functioning as the working electrode since trials with P3HT in solution provided no sufficient signal; a scan rate of 0.02 V/s was employed. All measurements were done under $N_2$ atmosphere in a glovebox and potentials were referenced against the ferrocene/ferrocenium ($Fc/Fc^+$) redox couple as an internal standard.

### 3.3.1 Setup Fundamentals

The typical CV setup (figure 3.5) consists of an electrochemical cell holding a solution of the analyte, i.e. the compound under investigation, and a supporting electrolyte into which a working electrode, a reference electrode, and a counter electrode are immersed; commonly, during operation the cell is purged with an inert gas (e.g., Ar) to avoid involuntary chemical reactions [169, 170] but, here, this part of the setup could be omitted as all measurements were done in a $N_2$ glovebox. The measurement is based on the idea that a potential difference $V_{\text{appl}}$ is applied between two electrodes within the cell, inducing charge transfer between the working electrode and the molecular orbital of the analyte under investigation, e.g. the highest occupied molecular orbital in the ground state (HOMO) and lowest unoccupied molecular orbital in the ground state (LUMO). This leads to a measurable change in current $I$ which, in turn, is indicative of $V_{\text{redox}}$ that can, subsequently, be converted to $IE$ or $EA$ values.

A potentiostat is used to control $V_{\text{appl}}$ between working and counter electrode and to measure $I$ through the circuit they form with the electrochemical cell. $I$ is then recorded as a function of the potential $V$ which is sensed separately through the reference electrode. The use of a counter electrode to provide current allows the reference electrode to sense $V$ without an ohmic drop at the electrode interface, i.e. the activities of the species that determine the potential of the reference electrode, are kept well below any limitation by electrode surface area and species availability [170]. The bulk solution resistance poses as another source for an ohmic drop and is commonly minimized by the addition of an electrolyte providing ionic charge carriers [169, 170]. In CV, $V_{\text{appl}}$ is set by the potentiostat such that $V$ is swept linearly and in alternating direction between two preset potentials at a preset scan rate. Increasing $V$ constitutes an anodic scan providing insight on oxidizing reactions, probing the occupied states; analogously, reducing reactions probing the unoccupied states can be observed through a cathodic scan, done with decreasing $V$.

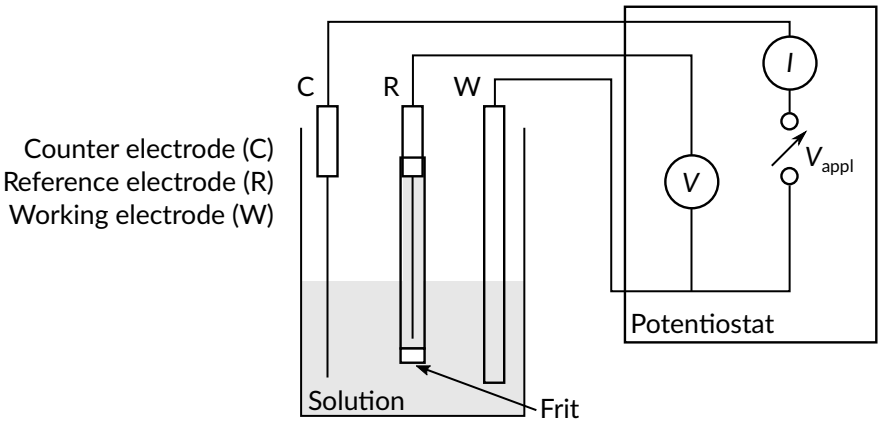


Figure 3.5: Cyclic voltammetry (CV) setup diagram (excluding inert-gas purging facilities). The potentiostat circuit is depicted by functions of potential $V_{\text{appl}}$ application, and current $I$ and potential $V$ measurement; it is not representative of the actual circuit.

$V$ is measured as relative to a well-defined redox reaction that the material in the reference-electrode assembly undergoes. However, such reference electrodes are commonly unavailable when working with dry organic solvents [170], as required by the compounds investigated here. In this case, a pseudo-reference is used, often made of simple Ag or Pt wires in the same electrolyte solution, separated from the analyte solution by a porous glass frit; they provide a reference potential that is dependent on the electrolyte and solvent employed [170]. Therefore, a compound with a well-defined redox couple such as $Fc/Fc^+$ is added to the solution during or right after the sample measurement as an internal standard, providing a reproducible reference potential to align the data, post-measurement.

Finally, solvent, electrolyte, and electrodes must be chosen such that the $V$ range of interest lies within their so-called electrochemical windows, i.e. they do not undergo any electrochemical reaction themselves.

### 3.3.2 Data Acquisition and Treatment

The recorded $I(V)$ curve—the *voltammogramm*—is subject to the charge-carrier density and kinetics in the solution, i.e. the ionic charge-carrier spatial distribution and movements [170]. Therefore, crossing a $V_{\text{redox}}$ threshold does not yield an immediate response but a more gradual increase in current and subsequent drawn-out decrease while the $V$ sweep continues. Hence, on the anodic scan, an oxidation peak is observed at $V_{\text{p,a}} > V_{\text{redox}}$ and, when the direction switches to the cathodic scan, this behaviour is mirrored in both $V$ and $I$ and a negative reduction peak at $V_{\text{p,c}} < V_{\text{redox}}$ occurs (see figure 3.6(a)).

When corresponding oxidation and reduction peaks are of comparable magnitude and well resolved, $V_{\text{redox}}$ can be estimated by the so-called half-wave potential $V_{1/2} = (V_{\text{p,a}} + V_{\text{p,c}})/2$ [169, 170]. However, in the case of the P3HT film, the peaks are insufficiently defined due to close overlap of adjacent ones. Hence, to derive the $IE$, $V_{\text{redox}}$ is estimated from the onset of the oxidation features (see figure 3.6(b)), in line with previous $V_{\text{redox}}$

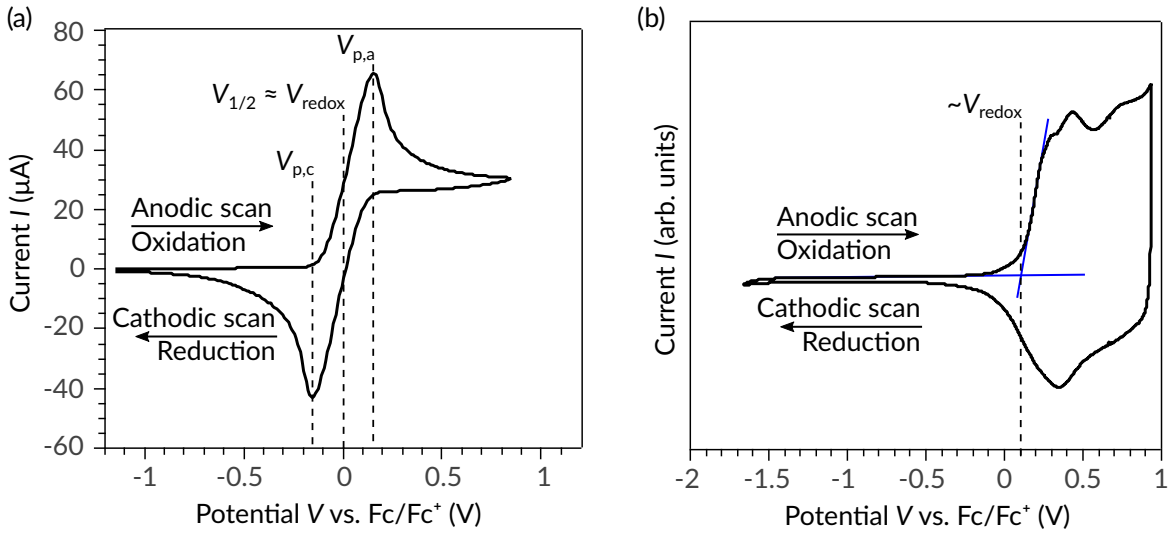


Figure 3.6: Exemplary voltammogramms (a) of ferrocene/ferrocenium ($Fc/Fc^+$; in solution) with oxidation and reduction peaks at $V_{p,a}$ and $V_{p,c}$, respectively, to determine the half-wave potential $V_{1/2}$ as an estimate for the redox potential $V_{redox}$ and (b) of P3HT (solid film on an ITO-coated working electrode) with the oxidation-feature onset as an estimate for $V_{redox}$.

determination for P3HT in literature [76]; for consistency, this approach was also applied to the h10T film.

To this point, all $V_{redox}$ values would be derived with respect to the pseudo-reference potential which offers insufficient reproducibility between experiments[169, 170]. Therefore, here, Fc was added to the solution after measurement of the analyte—without any changes to the setup—and the $V$ scale was subsequently zeroed on $V_{1/2} \approx V_{redox}$ of the $Fc/Fc^+$ redox couple, following the notion that Fc is regarded as a choice of *internal standard* that is inert to reactions with most analytes [171].

Finally, as $IE$ and $EA$ values are commonly preferred in OSC-doping narratives, the redox potentials in Volt (V) were converted to energies in eV by multiplication with the elementary charge e and zeroing on the vacuum energy. While multiple values for $V_{redox}$ of $Fc/Fc^+$ *versus* vacuum energy are accepted across CV users, −5.1 eV [75] was chosen for the data in this thesis in line with key literature values [64]; a minimum uncertainty of ±0.1 eV [75] was assumed for all values. While some publications handle $IE$ and $EA$ as negative numbers, they are here provided as positive values to associate higher $EA$ with higher dopant strength. Consequently, the conversion follows:

$$IE \text{ or } EA = 5.1\,\text{eV} + \text{e}\,V_{redox} \tag{3.9}$$

## 3.4 Grazing-Incidence X-Ray Diffraction (GIXRD)

For the characterization of crystalline structures in thin films, as investigated in this thesis, grazing-incidence x-ray diffraction (GIXRD) is a commonly employed technique. As highlighted in chapter 4, the spatial arrangement of the molecules plays an important

role in the competition between IPA and CPX formation; while GIXRD only probes crystalline phases, conclusions on amorphous parts in semi-crystalline films—as commonly formed by P3HT—can be drawn by comparison with data from techniques probing the entire make-up of the sample, e.g. UV-vis/NIR and FTIR.

The first GIXRD dataset in this thesis (presented in figure C.7) was recorded by Dr. Wolfgang Bodlos (TU Graz, Graz, Austria) at the Elettra Sincrotrone Trieste, Italy on beamline XRD1 [172]. The primary beam in this setup had a wavelength $\lambda$ of 1.4 Å (8.9 keV), an incidence angle $\alpha$ of 0.2°, and a 400 $\mu m^2$ beam diameter. Data was acquired using a stationary Dectris Pilatus 2M detector and samples were rotated 360° around their surface normal during acquisition to achieve radially homogeneous powder patterns. The second dataset (presented in figures 4.4 and C.8) was recorded by Melissa Berteau-Rainville (INRS, Varennes, QC, Canada) and Somaiyeh Charoughchi (Concordia University, Montreal, QC, Canada) at the Canadian Light Source Saskatoon, SK, Canada on beamline BXDS-IVU. The primary beam with $\lambda = 0.92$ Å (14 keV) was employed at $\alpha = 0.15°$ (close to the critical angle of total reflection) and exhibited beam dimensions of 100 µm vertical, 2 mm horizontal. Data acquisition was done using a stationary Rayonix MX300 detector and without sample rotation since the preliminary data in the first set showed the films to exhibit no relevant texture.

### 3.4.1 Setup Fundamentals

While x-rays can be categorized as ionizing radiation, the interaction with matter that is exploited in x-ray diffraction, is Thompson (elastic) scattering, i.e. the photon energy is preserved and not transferred to the electron that serves as the scatterer. Instead, the incoming and outgoing wavevectors $\mathbf{k_i}$ and $\mathbf{k_o}$, respectively, only undergo a momentum transfer defined by the scattering vector $\mathbf{q} = \mathbf{k_o} - \mathbf{k_i}$ with $|\mathbf{k_i}| = |\mathbf{k_o}| = 2\pi/\lambda$ [173]. For an incident plane wave, scattering at a point-charge scattering center creates a spherical wave around it. For multiple scattering centers, the difference in path length for each one leads to phase shifts between the outgoing spherical waves which, in turn, form patterns of constructive and destructive interference. For scattering centers on a regular lattice, like the electron clouds of atoms in a crystal, constructive interference occurs when the path difference is an integer $m$ multiple of $\lambda$ [173]. When considering a lattice plane with angle $\theta$ towards $\mathbf{k_i}$ and its plane normal $\mathbf{n}_{\text{lat}}$ parallel to $\mathbf{q}$ (see figure 3.7(a)), the condition for constructive interference is described by the Bragg equation:[§]

$$2d \sin\theta = m\lambda \tag{3.10}$$

The lattice plane distance $d$ is therefore connected to $\theta$ as an experimentally accessible parameter to be scanned for intensity maxima of the outgoing beam, i.e. the *Bragg reflections* or *Bragg peaks*.

[§]While the Bragg equation can be readily derived from the geometry depicted in figure 3.7(a), it can also be arrived at by summation of the scattering waves from all scattering centres as, e.g. demonstrated in section 1.1 of [173].

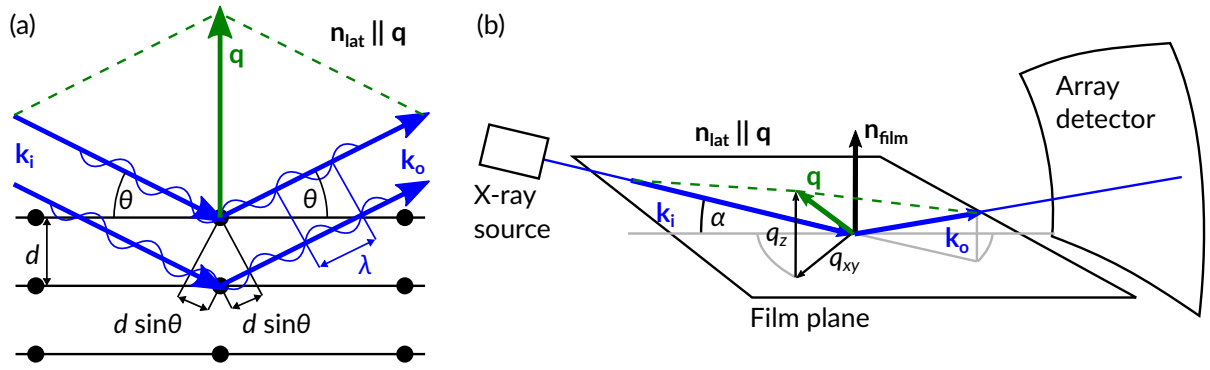


Figure 3.7: (a) Visualization of the Bragg equation; shown are the incoming and outgoing wavevectors $\mathbf{k_i}$ and $\mathbf{k_o}$, respectively, their angle $\theta$ with the lattice plane, the lattice plane distance $d$, the lattice normal $\mathbf{n}_{\mathrm{lat}}$, and the scattering vector $\mathbf{q}$. (b) Geometry of grazing-incidence x-ray diffraction (GIXRD) with respect to the sample film plane; $\mathbf{k_i}$, $\mathbf{k_o}$, $\mathbf{n}_{\mathrm{lat}}$, and $\mathbf{q}$ are the same as in (a); additionally shown are the $\mathbf{q}$-components $q_z$ perpendicular and $q_{x,y}$ parallel to the film plane, the angle $\alpha$ between $\mathbf{k_i}$ and the film plane, and the film-plane normal $\mathbf{n}_{\mathrm{film}}$.

More generally, $d$ can be connected to the scattering-vector length $q = |\mathbf{q}|$ under geometrical consideration of $\sin\theta = m\frac{q/2}{|\mathbf{k_i}|}$ and the wavevector length $|\mathbf{k_i}| = 2\pi/\lambda$:

$$d = m\frac{2\pi}{q} \tag{3.11}$$

This equation becomes relevant in setups where $\theta$ is not directly measured and data based on a more complex geometry is commonly made accessible by providing intensities in *reciprocal space*, i.e. as a function of $\mathbf{q}$ (*vide infra*).

Looking at the overall lattice, with its unit cell defined by the vectors $\mathbf{a_1}$, $\mathbf{a_2}$, $\mathbf{a_3}$, a lattice plane designated '$(hkl)$' can be set up by three points $\mathbf{a_1}/h$, $\mathbf{a_2}/k$, $\mathbf{a_3}/l$, featuring the Miller indices $h$, $k$, $l$ (see (111) and (221) as examples in figure 3.8). Within the framework of this thesis, changes in the spacing of the (100), (200), (300), and (020) planes in crystalline P3HT, as defined by Kayunkid et al. [174], are investigated (see section 4.3.3).

It must be noted that equation 3.10 or 3.11 only considers the $\theta$ or $q$ *position*,[¶] respectively, of the Bragg reflections. However, the actual intensity of a certain Bragg peak is due to the number of electrons in the atoms that serve as scattering centers and the shape of the electron distribution, contributing the *atomic form factor* [173, 175]. The intensity is further governed by the *structure factor* which considers the arrangement of the atoms in the unit cell [173, 175]. With the latter causing characteristic lattice-plane dependent variations in peak intensity, molecular species can be identified if their crystal structure has been previously resolved by, e.g., single-crystal x-ray diffraction (*cf.* figure C.8). Notably, these intensity variations can also result in certain Bragg peaks becoming undetectably weak (without being systematically extinct).

[¶]As $\theta$ and $q$ are scalar quantities, they serve as 'positions' strictly with respect to the geometry focused on parallel lattice planes as depicted in figure 3.7(a), not in the overall geometry of setup and sample.

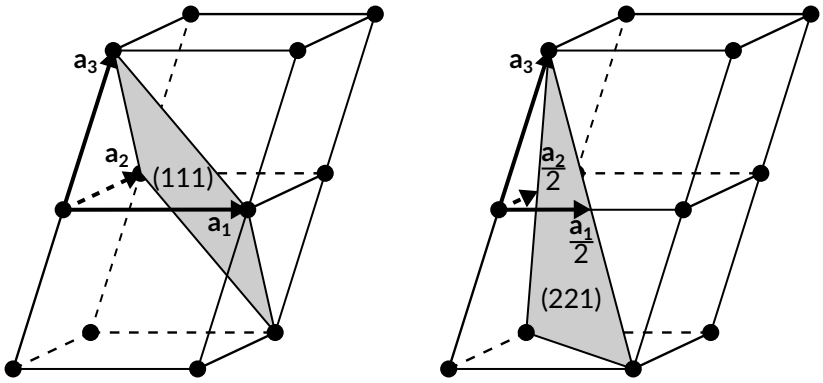


Figure 3.8: Examples of lattice planes with Miller indices (111) (left) and (221) (right) within an arbitrary unit cell defined by the vectors $\mathbf{a_1}$, $\mathbf{a_2}$, $\mathbf{a_3}$, and one adjacent cell.

In *specular* x-ray diffraction, equation 3.10 is directly applied by lining up the lattice planes of interest such that $\theta$ can be scanned. This is commonly achieved in a so-called $\theta/2\theta$ setup where the sample is rotated by $\theta$ around an axis perpendicular to $\mathbf{n}_{\text{lat}}$ of the investigated set of parallel lattice planes, thus, controlling their angle with $\mathbf{k_i}$ while the detector concomitantly moves by $2\theta$ around the same axis to form an angle of $\theta$ between the planes and $\mathbf{k_o}$ [173].

Firstly, however, considering the low degree of crystallinity of the P3HT thin films studied in chapter 4, the $\theta/2\theta$ geometry would pass the beam through too little sample material, i.e., too small/few crystalline phases. To address this issue, in GIXRD, a very small incidence angle $\alpha$ between $\mathbf{k_i}$ and the film plane (see figure 3.7(b)), close to the angle of total reflection, is set to make the beam travel the furthest part through the film; e.g. at $\alpha = 0.15°$ the beam could travel through a 0.5 µm film for up to 190 µm before meeting the substrate. This technique, however, has its limitations as the drawn-out beam footprint means that diffracted beams can now come from a wide area on the sample causing an instrumental broadening of the Bragg peaks. In principle, this issue can be countered by using secondary slits which are, however, incompatible with the use of an area detector (as used in the setup at the Canadian Light Source BXDS-IVU beamline). For such high precision measurements a line- or point-detector must be used instead, fixed on a detector arm and moved to record the desired $q$-space, which tremendously increases data acquisition time [176, 177] as well as the time the sample is exposed to the primary x-ray beam which can cause significant beam damage [178].

Secondly but not of lesser importance, the $\theta/2\theta$ geometry demands that only the sets of parallel lattice planes with $\mathbf{n}_{\text{lat}}$ in the $\theta/2\theta$-plane can be measured at a time. In contrast, the fixed $\alpha$ in GIXRD means that $\theta$ is fixed for all lattice planes parallel to the film plane which, therefore, cannot be probed in this configuration, making it a technique complementary to specular x-ray diffraction. To conveniently cover diffraction from all lattice planes accessible in this configuration and to reduce sample exposure, 2-dimensional array detectors are commonly employed to record the Bragg reflections, producing a *reciprocal space map* after conversion of the angular data into reciprocal space [175]; note that azimuthal rotation of the sample is still needed (*vide infra*). Under consideration of the actual instrument geometry, the pixels of the array can be mapped to

the coordinates of $\mathbf{q}$, namely, its components in parallel and perpendicular to $\mathbf{n}_{\text{film}}$, $q_z$ and $q_{xy}$, respectively (see figure 3.7(b)). Using these coordinates, $q = |\mathbf{q}| = \sqrt{q_z^2 + q_{xy}^2}$ can then be entered into equation 3.11 to calculate $d$ [179].

The GIXRD configuration also entails that the sample can only be rotated around the film-plane normal $\mathbf{n}_{\text{film}}$ through which, in turn, $\theta$ only changes for lattice planes where $\mathbf{n}_{\text{lat}}$ has a non-zero component perpendicular to $\mathbf{n}_{\text{film}}$. Such rotation is commonly omitted to reduce sample exposure and experiment time when it is known that the the crystalline domains of a sample have a preferred orientation towards the film plane but are randomly rotated around $\mathbf{n}_{\text{film}}$, i.e., when the film exhibits a *fiber texture* [173]. This is the case for the P3HT samples investigated in [7], i.e. chapter 4, as evident from the first dataset (Elettra Sincrotrone Trieste; *vide supra*) where sample rotation yielded no change in the recorded Bragg-peak positions. Subsequently, sample rotation was omitted for the second dataset (Canadian Light Source; *vide supra*).

### 3.4.2 Data Treatment

The treatment of reciprocal space maps was mainly executed using the software GIDvis [179]. Under provision of the beamline specifications and geometry (as obtained in-situ from a reference scan using a NIST standard of $LaB_6$ [180]) it can, among other functions, convert the pixel data of the detector into $q_z$,$q_{xy}$ coordinates. To reduce signals from air scattering, data had been recorded with a blank substrate to recreate the same geometry as in a sample measurement and was subsequently subtracted from any sample data, using a custom Mathematica script.

To gain better insight on peaks with focus on (near-)out-of-plane (small $q_{xy}$) and (near-)in-plane (small $q_z$) features, integrated line scans along constant $q = \sqrt{q_z^2 + q_{xy}^2}$ within 3-13° off the $q_z$ and $q_{xy}$ axis, respectively (see figure 4.4), were extracted using GIDvis; such integrated line scans over limited range are often called 'cake slices', 'cake (slice) integrations' and similar names. Peak fitting on these line scans was done in a manner similar to that employed with FTIR data. With focus on the direct vicinity of the investigated peak, the background was flattened by subtraction of a linear or low-polynomial fit through data points around the features identified as peaks (*cf.* figure4.4(b) 'F4TCNQ' and figure C.6).

Finally, GIDvis was also employed to identify the occurrence of crystalline F4TCNQ, F2TCNQ, FTCNQ, and TCNQ by loading the known structure files published for these compounds and aligning the structure-factor weighted intensities from the files with the peaks observed in the present data (see figure C.8).

## 3.5 Thin-Film Conductivity

Application-related effectiveness of doping, as addressed in this thesis, is easiest shown through an increase in thin-film conductivity. Here, sample films where spin-coated onto glass slides that have a patterned layer of ITO acting as electrodes. The film is deposited

on top and the electrodes are patterned in such a way that the portion of the film that lies between the electrodes is probed (see figure 3.9(a)).

To measure current-voltage ($I$-$V$) curves, a Keithley 2400 source-measure unit was employed together with an Ossila OFET test board to contact the patterned-ITO substrates purchased from Ossila. Voltage sweeps were applied from −1 to 1 to −1 V set to a total of 101 voltage steps at 0.06 s settling time on the Keithley 2400. All measurements were done in a glovebox under $N_2$ atmosphere. Dimensions of the film probed were measured using optical and atomic force microscopy, as explained in section 3.6.

### 3.5.1 Setup Fundamentals

The electrical conductivity $\gamma$ is, from a charge-carrier perspective, defined by the elementary charge e, the charge-carrier density $n$ and their mobility $\mu$ as [73]:

$$\gamma = e n \mu \tag{3.12}$$

However, it can also be determined from the resistance $R$ of a sample with well-defined dimensions, i.e. the cross-section $A$ and the channel length $L$ between electrodes through which charge carriers have to travel. For an electrode setup as depicted in figure 3.9, $A$ is defined by the channel width $w$ and the film thickness $t$. The conductivity is, thus, given by:

$$\gamma = \frac{L}{RA} = \frac{L}{Rwt} \tag{3.13}$$

### 3.5.2 Data Acquisition and Treatment

While it seems straightforward to obtain $R$ through Ohm's law $V = RI$ by measuring a single $V$ and $I$ data point, this approach provides no knowledge of whether the applied $V$ is within the ohmic regime, i.e. whether $V(I)$ follows a linear trend and, thus, conforms to Ohm's law, in the first place. Therefore, a symmetrical voltage sweep around $V = 0$ is done and $R$ is retrieved from the slope of a linear fit, if applicable to the measured curve.

Commonly, 4-point probe setups are used wherein $V$ is sensed with a separate pair of electrodes since the current-providing ones may suffer from contact resistance $R_{\text{contact}}$ as an unknown contribution to the measured resistance $R_{\text{measured}} = R + R_{\text{contact}}$. However, proper contacting can be problematic in this configuration with soft materials like P3HT. Therefore, the patterned-ITO substrates chosen from Ossila offer a different approach. They provide a set of electrode pairs with 5 different $L$ values on one substrate to resolve $\gamma$ with minimal influence of $R_{\text{contact}}$, as follows.

Employing equation 3.13 on $R_{\text{measured}}$ provides:

$$R_{\text{measured}} = (\gamma w t)^{-1} L + R_{\text{contact}} = m_{R(L)} L + R_{\text{contact}} \tag{3.14}$$

with $m_{R(L)}$ being the slope that can be retrieved through linear regression through the $R_{\text{measured}}(L)$ data points. The conductivity can subsequently be determined through:

$$\gamma = (m_{R(L)} w t)^{-1} \tag{3.15}$$

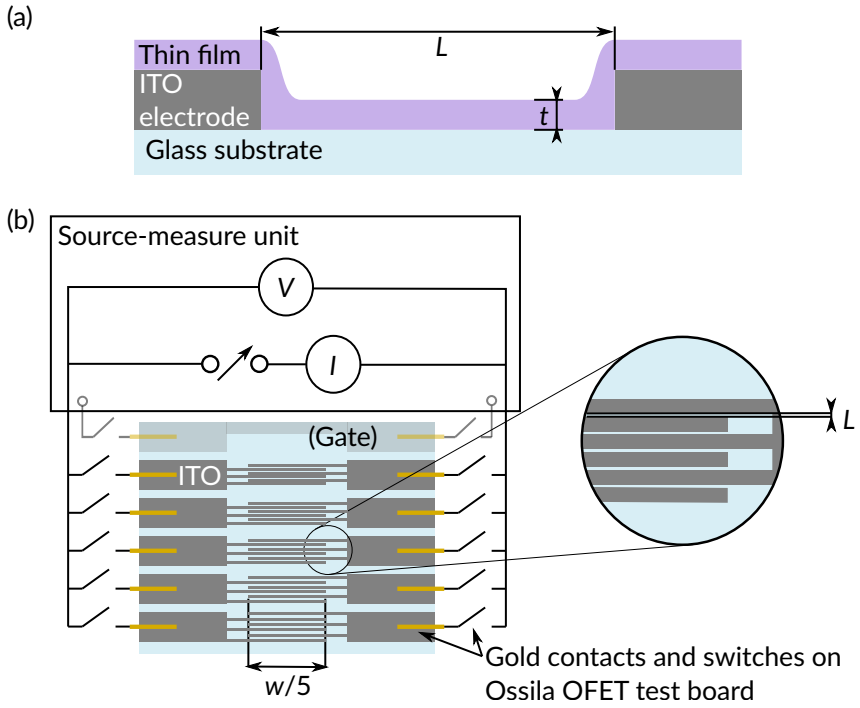


Figure 3.9: Visualization of relevant sample dimensions in the thin-film conductivity measurements, namely, film thickness $t$, channel length $L$, and channel width $w$. (a) Side view into the channel between electrodes. (b) Top view onto the substrate, additionally, showing connections with the source-measure unit (no thin film shown, here, for clarity). Where the 3 fingers of each electrode interdigitate, they form 5 electrically parallel channels whose widths add up to $w$.

Its uncertainty $\Delta\gamma$ is propagated through:

$$\Delta\gamma = \frac{1}{wt}\sqrt{\Delta m_{R(L)}^2 + m_{R(L)}^2\left(\frac{\Delta w^2}{w^2} + \frac{\Delta t^2}{t^2}\right)} \tag{3.16}$$

with $\Delta m_{R(L)}$, $\Delta w$, and $\Delta t$ being the uncertainty of $m_{R(L)}$, $w$, and $t$, respectively.

## 3.6 Atomic Force Microscopy (AFM)

While the exploration of surface morphologies is the common target of atomic force microscopy (AFM), this technique is exclusively employed here to determine the relevant dimensions for thin-film conductivity calculations, as mentioned in the previous section. The film thicknesses $t$ of the samples investigated in this thesis lie in the range of 1–100 nm, which can be well characterized by so-called tapping-mode AFM [181], as applied here. In addition, lateral scanning sizes up to several tens of µm (with the employed instrument) mean that the smallest of the channel lengths $L$ could be measured and was compared to values obtained via optical microscopy.

A Bruker Dimension Icon AFM in its proprietary PeakForce QNM mode was employed with a silicon nitride tip (AppNano ACTA-50) under ambient conditions. $L$ values were acquired using the optical microscope that is part of the same AFM; the channel width $w$ was also confirmed via optical microscope.

### 3.6.1 Setup Fundamentals

AFM is a raster-imaging technique where a surface structure is scanned with a stylus-type probe (schematic depiction in figure 3.10) interacting on the atomic scale. A cantilever parallel to the sample surface holds a force-sensing tip at its end, directed towards the surface. At tip-surface distance $r$, when not in direct atomic contact, thus, not under the influence of atomic repulsion following a $r^{-12}$ dependency, surface-tip interaction is dominated by attraction through the van-der-Waals force whose potential follows a $r^{-6}$ dependency [182]. This would constitute a rapid sensitivity loss with increasing $r$. However, in a reasonable electrostatic approximation of the tip as a hemisphere (10–50 nm radius) encountering an infinite sample plane, a $r^{-1}$ dependency is encountered instead, explaining why AFM is feasible, in the first place [182]. Due to the $r$-dependent pull on the tip, the cantilever gets deflected, and the deflections are measured and used to calculate the sample height at the raster point. Most commonly, the deflection is measured by reflecting a laser beam off the back of the cantilever and registering the reflection movement on a quadrant photodiode while probe height $z$ over the sample is controlled by piezoelectric elements moving the probe.

The AFM mode employed in this thesis is Bruker's proprietary PeakForce QNM—an evolution of tapping mode. Here, the $z$ scanner oscillates the probe at few kHz and the dampening response is analyzed to derive tip-proximity to the surface; as the name suggests, special emphasis is placed on peak-force analysis. This improves $z$ scanner control towards reduced energy dissipation into the sample which is crucial for maintaining the integrity of soft samples like polymers throughout the experiment. 'QNM' designates a more in-depth quantitative nano-mechanical analysis of force curves extracted from the oscillation response, but is not of relevance here, as only film thicknesses where measured but not their mechanical properties.

### 3.6.2 Data Acquisition and Treatment

To measure the polymer-film thickness, small trenches were softly dragged into them using soft, flexible syringe needles. AFM scans where done on 1 µm × 20 µm areas with the long axis perpendicular to the trench edge and within the channel of the central and the two outermost electrode pairs (*cf.* substrate in figure 3.9) to account for film inhomogeneity causing a standard deviation to average $t$ of 10%–40%.

Data was treated and analyzed in Gwyddion (GNU General Public License (GPL) v2.0; http://gwyddion.net/). The images were semi-automatically flattened by manually fine-tuning of the parameters of the to-be-subtracted 2-dimensional polynomial while comparing of flatness in both the trench bottom and the pristine film, and under omission of debris at the trench edge which was easily identified by its location and its at least one order of magnitude higher thickness. The film thickness $t$ was then taken from

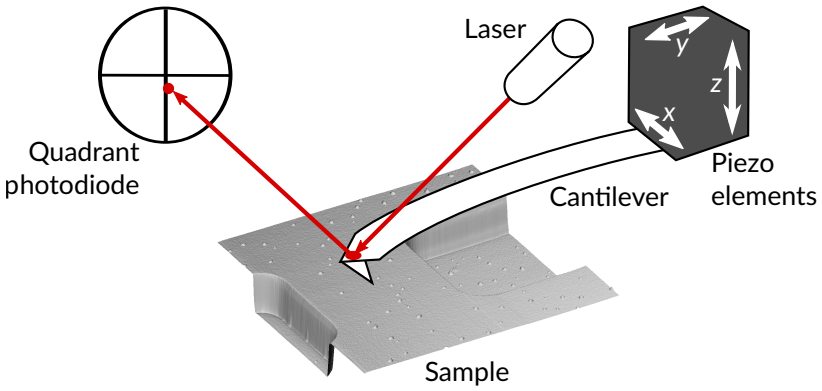


Figure 3.10: Schematic depiction of an atomic force microscopy (AFM) setup. Cantilever deflection due to interaction between tip and sample is measured by reflecting a laser beam off the back of the cantilever and registering the reflection movement on a quadrant photodiode. Probe height $z$ over the sample is controlled by piezoelectric elements moving the probe.

a profile cut through the image and averaged over the values from the three electrode pairs probed; due to limited instrument access colliding with the large amount of images to be taken for the entire conductivity series analyzed in section 4.3.4, image capture was stopped as soon as an image was produced that offered an area without imaging artefacts large enough to lay the profile through.

A preliminary measurement using a 50 µm × 50 µm scan captured the entire channel length of the closest electrode pair with a nominal $L = 50\,\mu\text{m}$ but was, here, observed as almost 10 µm shorter; the optical microscope that is part of the same AFM, provided the same finding. Subsequently, the calibration was tested by the maintainer of the instrument, Patricia Moraille (Laboratoire de la caractérisation des matériaux, Université de Montréal). As the calibration was confirmed to be correct, I reached out to the substrate manufacturer Ossila and the product, as of writing this thesis, was thereafter provided with a batch-dependent deviation on $L$ of ±10 µm on their website (2023-02-04 16:24 EST, https://www.ossila.com/en-ca/products/interdigitated-ito-ofet-substrates?variant=1200244917). As a consequence, I verified the $L$ values of all samples using the optical microscope.

# Chapter 4

# Manuscript [7]: Critical Dopant Concentrations Govern Integer and Fractional Charge-Transfer Phases in Doped P3HT



H. Hase, M. Berteau-Rainville, S. Charoughchi, W. Bodlos, E. Orgiu, and I. Salzmann, "Critical Dopant Concentrations Govern Integer and Fractional Charge-Transfer Phases in Doped P3HT," *Journal of Physics: Materials*, vol. 6, no. 1, p. 014004, Jan. 2023.

In contrast to the published version, the present chapter adds a Foreword between Abstract and 4.1 Introduction to point out additional information of relevance in the framework of this thesis; section and reference numbering have been adapted to this thesis; the caption of figure 4.2 now additionally references section 3.2.3 for the merging of spectroscopic data.

## Abstract

The conjugated polymer poly(3-hexylthiophene) (P3HT) p-doped with the strong acceptor tetrafluorotetracyanoquinodimethane (F4TCNQ) is known to undergo ion-pair (IPA) formation, i.e. integer-charge transfer, and, as only recently reported, can form ground state charge-transfer complexes (CPXs) as a competing process, yielding fractional charge transfer. As these fundamental charge-transfer phenomena differently affect doping efficiency and, thus, organic-semiconductor device performance, possible factors governing their occurrence have been under investigation ever since. Here, we focus on the role of a critical dopant concentration deciding over IPA- or CPX-dominated regimes. Employing a broad, multi-technique approach, we compare the doping of P3HT by F4TCNQ and its weaker derivatives F2TCNQ, FTCNQ, and TCNQ, combining experiments with semi-

classical modeling. IPA, CPX, and neutral-dopant ratios (estimated from vibrational absorption spectroscopy) together with electron affinity and ionization energy values (deduced from cyclic voltammetry) allow calculating the width of a Gaussian density of states (DOS) relating to the highest occupied molecular orbital in P3HT. While a broader DOS indicates energetic disorder, we use grazing-incidence x-ray diffraction to assess spatial order. Our findings consider the proposal of nucleation driving IPA formation and we hypothesize a certain host-dopant stoichiometry to be key for the formation of a crystalline CPX phase.

# Foreword

In addition to the topics brought up in the abstract, it should be mentioned that, due to the broad, multi-technique approach used in the study, the manuscript published as ref. [7] serves as a comprehensive reference dataset on P3HT doped with the series of 7,7,8,8-tetracyanoquinodimethane (TCNQ) and its derivatives (referred to as'FxTCNQs'), i.e. F4TCNQ, 2,5-difluoro-7,7,8,8-tetracyanoquinodimethane (F2TCNQ), 2-fluoro-7,7,8,8-tetracyanoquinodimethane (FTCNQ). This was highlighted by one of the Referees in the peer-review process, pointing out that "[t]he properties of doped polymer thin films depend critically on the raw materials and the processing conditions, which makes it difficult to compare literature data. Therefore, the manuscript can somehow serve as a database for doped P3HT thin films [...]". As such, in addition to providing a vast amount of original data, the study becomes reminiscent of a small review and three side-discussions are embedded within the main storyline: (i) The recent proposal of bipolaron formation (*cf.* section 2.3) in P3HT for high F4TCNQ content [130] and its spectroscopic identification are briefly discussed in sections 4.3.1 and 4.4.1 while its implications on conductivity trends is considered in section 4.3.4. The comparison with own spectroscopic data and that in other literature points to the ambiguity of this proposal, mainly, due to overlap with CPX features [39, 58] not accounted for in that publication [130]. (ii) With TCNQ derivatives, the peak position of the C≡N stretching absorption bands is often used to determine the degree of charge transfer (*cf.* section 2.3.2); in sections 4.3.2 and 4.4.1 the reader is reminded that the peak position is more generally impacted by the electrostatic *environment* of the C≡N groups as well, e.g. it is also affected by the polaron delocalization on the P3HT backbone [58]. Further, a comparison with the ring C=C stretching-mode peaks demonstrates an over-representation of the CPX dopant population by the C≡N modes which, consequently, is taken into consideration in this study by regarding the C≡N mode-derived IPA dopant percentage as a low-limit estimate. (iii) Wegner et al. [48] found that, for the prediction of IPA formation, cyclic voltammetry (CV)-derived $IE$ and $EA$ values are superior to those derived from ultraviolet/inverse photoelectron spectroscopy (UPS/IPES; *cf.* section 2.1); sections 4.3.5 and 4.4.2 briefly discuss the general conditions in CV and UPS/IPES measurements that likely lead to this observation, thus, advocating for our own use of CV data.

Due to the comprehensive and seminal character of the presented study [7] regarding the doping processes at work with the FxTCNQ series, I became involved in two related works. One of them, conducted by Hu et al. [9], virtually expands [7] through UPS data

to investigate changes in the occupied DOS and Fermi-level shifts upon doping P3HT with F4TCNQ, F2TCNQ, and TCNQ, i.e. cases of IPA formation with a dopant with a strong *EA*, a weak *EA*, and of CPX formation, respectively. For improved comparability with [7], I shared my sample preparation technique with the researchers conducting the experiments (the group of Dr. Steffen Duhm, Soochow University, China) and assisted in the drafting of the publication (currently under review). In that work, the occupied DOS widths differ from the HOMO-DOS width calculated within the present thesis as it includes the HOMO levels regardless of their occupation upon doping, hence, different perspectives on the DOS are offered in both works.

The second study, conducted by Charoughchi et al. [8], characterizes a novel p-dopant (referred to as PFP3CN3-CP) based on a cyclopropane core (instead of the quinoid core in the FxTCNQ series) that is sterically shielded by three perfluorophenyl rings. Its performance is tested on P3HT and compared to that of F2TCNQ and F4TCNQ using the conductivity values, optical and vibrational spectroscopy data found in the present chapter. Again, to improve data comparability and to collaboratively share my experience, I was involved in the measurement of the according data regarding the novel dopant and contributed to the writing of the manuscript for publication. The key finding of this study is that while PFP3CN3-CP exhibits virtually the same *EA* as F2TCNQ, in marked contrast to F2TCNQ, its steric shielding inhibits CPX formation with P3HT (*cf*. section 2.4). Consequently, it produces a greater increase in P3HT thin-film conductivity than F2TCNQ does and, at lower doping ratios, even matches that achieved using F4TCNQ.

In the context of this thesis, it should not remain unmentioned that three works paved the way to the present manuscript [7]. Firstly, I already collected a preliminary dataset on P3HT doped with FxTCNQs at varied dopant loading for my master's thesis [1]. However, due to experimental limitations resulting in limited data range and reliability, I was not able to draw conclusions other than supporting previous findings put forward by ref. [34] that F2TCNQ and FTCNQ can form IPAs with P3HT despite their unfavorable *IE-EA* relations. Subsequently, it became a primary task of the present thesis work to create a more reliable and complete dataset, meaning: (i) The experimental uncertainty on the dopant molar ratio $\chi$ could now be quantified at all (see $\chi$ values in section 4.2.1). (ii) The influence of unintentional $O_2$-doping on conductivity results (as previously identified [1]) was eliminated by performing all measurements (except grazing-incidence x-ray diffraction (GIXRD)) under inert $N_2$ atmosphere. (iii) Carefully improved optical spectroscopy (UV-vis/NIR) settings (e.g., shorter acquisition times meaning less signal fluctuation; *cf*. section 3.1.3) enhanced the signal-to-noise ratio significantly, thus, low-absorption features of small IPA or CPX populations became identifiable. (iv) The creation of Fourier-transform infrared spectroscopy (FTIR) and GIXRD datasets that completely match all dopant concentrations used in UV-vis/NIR and conductivity measurements to allow for comparability. Only under these conditions it became possible to provide the comprehensive benchmark database that this manuscript [7] constitutes, and to create the hypothesis of crystalline CPX-phase formation based on stoichiometry (see section 4.4.4).

Secondly, in contrast to my master's thesis [1], the new extent and quality of the FTIR data allowed for the assessment of the doping-induced broadening of the Gaussian-shaped DOS related to the highest occupied molecular orbital (HOMO) in P3HT (see sections 4.2.6, 4.3.6, and 4.4.2). While still resolving issues on the experimental uncer-

tainty of $\chi$, a reliable sub-set of the data was published [6], comprising only F4TCNQ, FTCNQ, and TCNQ at a single $\chi$ value of 2%. The present manuscript [7] constitutes a fundamental extension of this publication [6] but still comprises all its findings for the reader's convenience and, therefore, its inclusion as a manuscript into the present thesis would not have provided the reader with additional information but rather would have introduced redundant elements into this work.

Thirdly, the fact that this manuscript [7] highlights the ongoing discussion around the C≡N stretching modes, has its origin in data I had acquired for my master's thesis [1], which I carefully re-analyzed and prepared for publication [2] in the first year of my PhD program. However, this work is not included in the present thesis as it is mainly based on data already acquired before. Its key finding is that upon thermal annealing of an F4TCNQ-doped P3HT film at different temperatures, we observed reproducible and characteristic changes in diffraction data which were correlated with a distinctly shifted $F4TCNQ^{\bullet-}$ C≡N-mode peak in vibrational spectroscopy. By combining these findings we assigned this phenomenon to the formation of different P3HT-F4TCNQ mixed-crystal structures. Section 4.4.1 summarizes how subsequent studies that focused more directly on this peak, have gone into different directions putting forward alternative interpretations ever since.

Finally, it should be noted that the original manuscript [7] does not elaborate on reproducibility, aside from section 4.3.4 mentioning alternative conductivity data. Since the latter originate from an incomplete set, they were not statistically included into the present data points, hence, the conductivity error-bars in figure 4.5 may appear too small, at first sight. However, since section 4.3.4 identifies the discrepancy between conductivity values of two P3HT films with—nominally—17% TCNQ to be an issue of concentration precision (*vide supra*), figure 4.5 accounts for this by featuring concentration error-bars. In general, for time constraints, the exact experiments behind the present data were not repeated. Confidence in the data was rather drawn from these measurement already being repetitions of previous experiments but with improved parameter and instrument precision (*vide supra*); the fundamental finding of which dopant at which concentration undergoes IPA/CPX formation is in agreement with the previous data.

## 4.1 Introduction

Organic semiconductors (OSCs) are commercially highly successful in organic light-emitting diodes (OLEDs) [13, 14, 183] and have shown significant recent progress in areas as diverse as photovoltaics [20], flexible electronics [21], and thermoelectric energy harvesting [17, 18]. As for their inorganic counterparts, electrical doping as a method to generate mobile charge-carriers (electrons and holes) and spatially control their density is key for organic and hybrid devices, as it allows engineering efficient electron/hole injection, transport, and blocking layers. For the fundamental process of doping, that is, electron transfer between the OSC host and its molecular dopant, two complementary phenomena have been identified to occur, namely, the formation of spatially separated ion-pairs (IPAs) *via* integer charge transfer, and the formation of ground state charge-transfer complexes (CPXs) with only fractional charge transfer [25, 32, 33]. On the one

hand, IPA formation is energetically favorable for the system if, in first approximation, the electron affinity $EA$ of the p-dopant, typically a strong electron acceptor, matches or exceeds the ionization energy $IE$ of the donor, that is, the conjugated molecule/polymer forming the OSC host; n-doping proceeds in analogy (with an electron donor) but is not the focus of this present work. On the other hand, CPX formation is based on the spatial overlap and rehybridization between the frontier molecular orbitals, i.e. the lowest unoccupied molecular orbital in the ground state (LUMO) of the acceptor and the highest occupied molecular orbital in the ground state (HOMO) of the donor. Figure 4.1(a) shows a simple energy-level diagram for IPA and CPX formation. Notably, the two complementary processes do not exclude each other for a given system but can prevail in certain ratios governed by parameters yet to be fully identified. To maximize the mobile charge carrier density in an OSC, in most cases, suppressing CPX and promoting IPA formation is desired [25, 33, 34]. However, some examples exist where a moderate CPX fraction optimizes hole-transport in polymer-OLEDs [35] or maintains the performance of thermoelectric devices over time [36]. As such, achieving an in-depth understanding of the charge transfer processes upon doping and resilient knowledge of the parameters favoring one phenomenon over the other is of high application-related relevance for organic and hybrid electronics. The system of the conjugated polymer poly(3-hexylthiophene) (P3HT) p-doped with the strong molecular acceptor tetrafluorotetracyanoquinodimethane (F4TCNQ), seems to be ideal to address this issue, as it has long been assumed to form only IPAs, while recent studies have also reported CPX formation under certain conditions [36, 39, 49, 55, 56, 60]. In the following, we first provide a comprehensive overview of the vast literature addressing the doping behavior of this prototypical system and then suggest a model to rationalize charge transfer by differently strong dopants.

Figure 4.1(b) shows the possible spatial arrangements of P3HT and F4TCNQ as agreed upon by numerous studies. To begin with, Neelamraju et al. [49] reported increased CPX-prevalence in regio-random (rra) *versus* regio-regular (rr) P3HT, as well as with increasing dopant molar ratio $\chi$, creating an essentially pure CPX system with rra-P3HT at $\chi = 17\%$. In this study, the investigation of rra-P3HT suggests the importance of amorphous P3HT regions—and their effectively higher $IE$ (5.42 *versus* 5.13 eV in rr-P3HT [76]; values from redox potentials, see section 4.2 for conversion)—to promote CPX over IPA formation. In contrast, Jacobs et al. [39] created a crystalline, essentially CPX-only precedence in low-molecular weight rr-P3HT for $\chi = 13\%$ and 17%, which was possible by keeping the blend dissolved throughout the deposition *via* spin-coating and holding solution, pipette tips, and substrates constantly at 80°C. While this system turned out to be unstable as it reverts to IPA-prevalence under ambient conditions in <1 h (and in 1 d under $N_2$), Watts et al. [55] observed in IPA-dominated samples the CPX fraction to increase over the course of weeks. Most recently, Stanfield et al. [57] largely reconciled these discrepancies by studying the thermal annealing of F4TCNQ-doped rr-P3HT with different degrees of crystallinity. They concluded that there exists, indeed, a kinetically unstable, crystalline CPX polymorph, as found by Jacobs et al., in addition to a stable CPX phase in the amorphous regions. These findings were followed up by Wu et al. [184] employing all-atom molecular dynamics simulations which demonstrated that the IPA and CPX crystalline phases in this system are respectively entropy- and enthalpy-driven. There, however, the

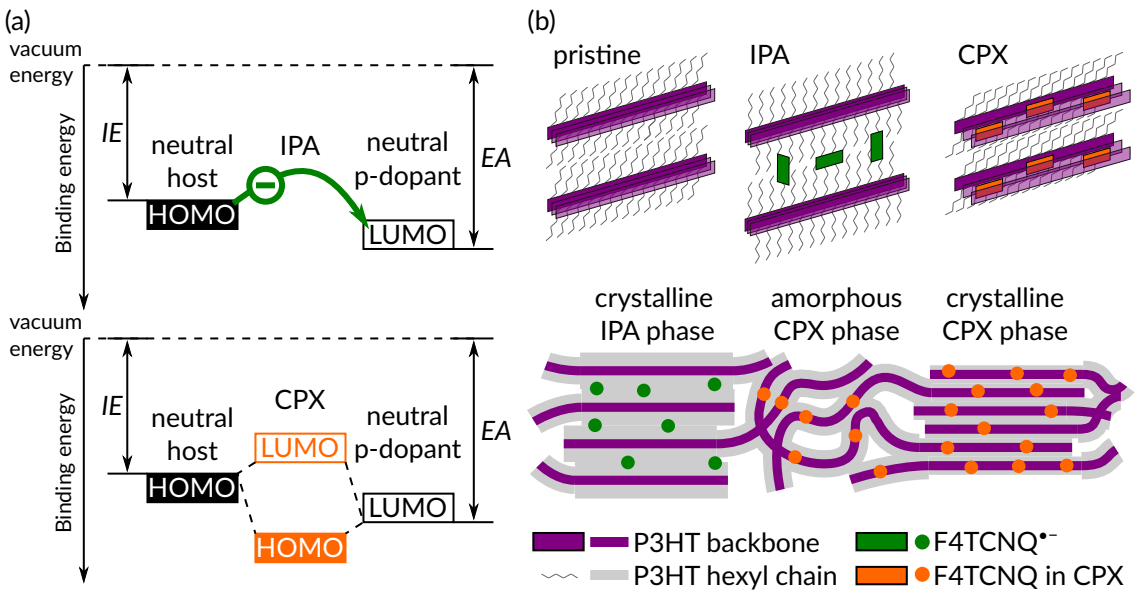


Figure 4.1: (a) Energy levels in p-doping for ion-pair (IPA) and charge-transfer complex (CPX) formation. (b) Spatial arrangements of P3HT and F4TCNQ discussed, here. Top: F4TCNQ intercalation with respect to the P3HT backbone and hexyl side-chain; $F4TCNQ^{\bullet-}$ rotation is still subject to debate [139, 140]. Bottom: Crystalline and amorphous phases discussed, here.

key mechanism favoring IPA formation was suggested to be a nucleation process starting with as few as 2–3 dopant radical anions as critical nucleus among the simulated 1728 P3HT monomer units while, in contrast, no critical nucleus was found for the crystalline CPX phase up to the maximum dopant loading that was investigated (144 CPX-forming dopants).

In an own previous study [6] we doped rr-P3HT with $\chi = 2\%$ F4TCNQ in comparison with FTCNQ and TCNQ—two derivatives with lower degree of fluorination and, hence, lower $EA$. Besides the full ionization of the F4TCNQ content, we observed that 88% of the FTCNQ and none of the TCNQ dopant molecules underwent IPA formation (the remainder forming CPXs). The stark contrast in ionization percentage between the latter two dopants, while their $EA$ values differ disproportionately little, led us to assume a self-amplifying effect: an initially small percentage of ionized dopants drives a structural disorder (e.g. polarization energy) and conformational disorder (local conjugation length-dependent $IE$) induced broadening of the host-HOMO density of states (DOS). This, in turn, provides more states at lower $IE$, hence, allowing to ionize a greater content portion of weak-$EA$ dopants such as FTCNQ.

Here, we now aim to determine the extent to which the nucleation process put forward by Wu et al. [184] can be consistent with a process of initial ionization that triggers further IPA formation. For $\chi > 8\%$, that is for dopant loadings higher than those investigated by Wu et al. [184], we study whether crystalline CPX-phase nucleation-sites may occur. This possibility has been suggested by the authors and appears likely because CPX-formation in rr-P3HT-F4TCNQ is typically found for high $\chi$ values [39, 49, 55]. To

this end, we build upon our previous study [6] by adding F2TCNQ as an intermediate *EA*-case between F4TCNQ and FTCNQ, extending the $\chi$ range to values of 1%, 2%, 5%, 9%, 17%, and performing all relevant analysis on that multitude of systems at a time, which we regard as inevitable in order to establish a consistent picture of the parameters governing the charge transfer processes at work. We first employ optical absorption spectroscopy in the ultraviolet to near-infrared range (UV-vis/NIR; section 4.3.1) supported by Fourier-transform infrared spectroscopy (FTIR; section 4.3.2) to quantify IPA and CPX occurrence. Then, we use grazing-incidence x-ray diffraction (GIXRD; section 4.3.3) to assess structural aspects and, subsequently, the influence of IPA and CPX formation on thin film conductivity (section 4.3.4). Finally, we use our FTIR data to determine the percentage of ionized dopants, perform cyclic voltammetry (CV) to estimate the $IE$ and $EA$ of P3HT and the dopant series, respectively (from the redox potentials [75], see section 4.3.5), and finally pursue semi-classical modeling of the density of states (DOS) (section 4.3.6). The latter is motivated by recent publications using energy resolved–electrochemical impedance spectroscopy (ER-EIS) [64, 185] and an improved analysis of time-of-flight photocurrent transients [186], which found a very narrow distribution of the P3HT HOMO-DOS of only 0.06–0.07 eV (Gaussian standard deviation $\sigma$)—a value at least four times smaller than that inferred from ultraviolet photoelectron spectroscopy (UPS) [64, 187]. This finding was explained by the UPS deduced DOS being convoluted with the electron escape function while the ER-EIS DOS is the result of direct electron transfer with electrolyte molecules [64]. Assuming $IE$ and $EA$ as the onsets of the Gaussian HOMO- and LUMO-DOS, respectively, and calculating $\sigma$ such that theoretical IPA occurrence agrees with our experimental data (see section 4.2 for details), we interpret larger $\sigma$ to result from greater disorder in the sample. With our calculations showing that the percentage of IPA-forming dopants concomitantly increases with $\sigma$, we can then find the initial $\sigma$ required to start the aforementioned nucleation effect. Our comprehensive data from multiple experimental techniques allows us, further, to assess the validity of using shifts of the F4TCNQ C≡N stretching-modes in FTIR (see section 4.3.2) for deriving the degree of charge transfer, which is a common practice in the field but subject of debate [2, 54, 58–60]. Thereby, we heed the initial advice from the seminal 1986 paper by Meneghetti and Pecile [53] that the ring C=C stretching mode would better serve that purpose—albeit often being masked by host-related peaks—as the C≡N modes are particularly sensitive to the molecular environment. We show that reliable conclusions about the degree of charge transfer can only be drawn if these data are interpreted very cautiously.

## 4.2 Methods

### 4.2.1 Sample Preparation

All samples were prepared and, if not specified otherwise, measured under inert $N_2$ atmosphere in a glovebox ($H_2O$ <2 ppm, $O_2$ <6 ppm). Anhydrous chloroform (Sigma-Aldrich, amylenes as stabilizer, purity ≥99%) was used as the common solvent. Tetrafluorotetracyanoquinodimethane (F4TCNQ), 2,5-difluoro-7,7,8,8-tetracyanoquinodime-

thane (F2TCNQ), 2-fluoro-7,7,8,8-tetracyanoquinodimethane (FTCNQ), and 7,7,8,8-tetracyanoquinodimethane (TCNQ) were used as purchased from Tokyo Chemical Industry Co., Ltd. (TCI) (all: purity >98.0%) and dissolved at a concentration of 1.2 mM through stirring on a heater at 60°C for 1 h and left to cool at room temperature for at least 1 h before further use. Poly(3-hexylthiophene-2,5-diyl) (P3HT; $M_W$ >45 kDa; 93% regioregularity) was used as purchased from Luminescence Technology Inc. (Lumtec) and dissolved at 60 mM immediately prior to use. Doped blends were made immediately before film deposition from pure-compound solutions, aiming at molar ratios of 100, 50, 20, 10, and 5 P3HT repeat units per dopant molecule, achieving dopant molar ratios $\chi$ of $(0.99 \pm 0.06)$%, $(2.0 \pm 0.2)$%, $(4.8 \pm 0.3)$%, $(9.1 \pm 0.6)$%, and $(17 \pm 1)$%, being referred to as 1%, 2%, 5%, 9%, and 17%, respectively. For UV-vis/NIR, 50 µL solution were drop-cast onto 1 cm × 1 cm quartz slides. For FTIR and GIXRD, 50 µL solution were drop-cast onto 1 cm × 1 cm double-side polished undoped Si wafer pieces. For CV on P3HT, 150 µL solution were spin-coated (static dispense, 30 s at 1000 rpm) onto 1 cm × 2 cm ITO coated glass. For conductivity measurements, 150 µL solution were spin-coated (static dispense, 30 s at 1000 rpm) onto 1.5 cm × 1 cm pre-patterned ITO electrodes on glass substrates. The latter were manufactured by Ossila and have a 3 cm electrode width and 5 electrode pairs with different channel lengths of $(40.4 \pm 0.6)$, $(64.7 \pm 0.6)$, $(90.7 \pm 0.6)$, $(140.5 \pm 0.6)$, and $(189.8 \pm 0.6)$ µm (measured as explained further below). Drop-casting was chosen to improve the signal-to-noise ratio where required, otherwise, spin-coating was performed to assure homogeneous coverage. Prior to use, substrates were cleaned in chloroform, acetone, deionized water, and isopropyl alcohol (in that order) each 10 min in an ultrasonic bath and left to dry for a few seconds on a precision wipe.

### 4.2.2 Optical and Vibrational Absorption Spectroscopy

UV-vis/NIR absorbance spectra were recorded on an Agilent (ex. Varian) Cary 5000 while keeping the samples under inert $N_2$ atmosphere in custom-built sealed boxes with quartz windows. Likewise, FTIR absorbance spectra were recorded on a Thermo Scientific Nicolet 6700 using a liquid-nitrogen cooled mercury cadmium telluride detector with the samples under inert $N_2$ atmosphere in sealed boxes with KBr windows. To assess the impact of ambient conditions in situations where the inert atmosphere could not be maintained, that is, atomic force microscopy (AFM) and GIXRD, FTIR was done once in the sealed spectroscopy box and then again after storing the samples in simple plastic boxes which were exposed to ambient conditions for one week (Parafilm-sealed under inert $N_2$ atmosphere), and fully exposing the samples to air 1 h prior to measurement. The observed changes do not significantly influence our results (see figure 4.3).

### 4.2.3 Grazing-Incidence X-Ray Diffraction (GIXRD)

Grazing-incidence x-ray diffraction (GIXRD) data were collected at Canadian Light Source Saskatoon, SK, Canada on beamline BXDS-IVU employing a Rayonix MX300 detector, 0.92 Å primary beam wavelength, an incidence angle of 0.15°, and beam dimensions of 100 µm vertical, 2 mm horizontal.

Preliminary data was collected at Elettra Sincrotrone Trieste, Italy on beamline XRD1 [172] employing a stationary Dectris Pilatus 2M detector, 1.4 Å primary beam wavelength, an incidence angle of 0.2°, and 400 $\mu m^2$ beam diameter. In that setup, the samples have been rotated by 360° during acquisition to achieve radially homogeneous powder patterns; data analysis however did not reveal relevant texture.

With $q_{xy}$ and $q_z$ being the in-plane and out-of-plane components of the scattering vector $\mathbf{q}$, intensities in figure 4.4(a) and (b) have been obtained through cake slice-integration along constant $q = |\mathbf{q}| = (q_{xy}^2 + q_z^2)^{1/2}$ within 3-13° of the $q_{xy}$ and $q_z$ axis, respectively, of the reciprocal space maps depicted in figure C.8 (only Canadian Light Source data). The error margin on the calculated lattice spacing $d = 2\pi/q$ was estimated from half of the largest full width at half maximum (FWHM) that we observed among the associated $q$ peaks, i.e. ±1.9 Å for $d_{100}$ and ±0.13 Å for $d_{020}$.

### 4.2.4 Conductivity

I-V measurements were done employing a Keithley 2400 source measure unit connected to an Ossila OFET test board to collect conductance data. For conductivity calculation, film thicknesses were determined by AFM on a Bruker Dimension Icon with a silicon nitride tip in its proprietary PeakForce QNM mode under ambient conditions. The channel length between electrodes and the electrode width were acquired using the optical microscope that is part of the same AFM. Trends in conductivity were reproduced three times, however, only the last series was fully analyzed in the present study as it was prepared with much improved experimental accuracy in $\chi$.

### 4.2.5 Cyclic Voltammetry (CV)

Cyclic voltammetry (CV) measurements were recorded employing a CH Instruments CHI604d potentiostat, $Ag/Ag^+$ reference electrode, Pt-wire counter-electrode, glassy carbon working electrode (where applicable), and a scan rate of 0.05 V $s^{-1}$. The glassy carbon working electrode was consecutively polished using 1.0, 0.3, 0.05 µm alumina powder before each measurement. Likewise, the counter electrode was polished using using 0.05 µm alumina powder, only. Before running CV, a blank voltammogram without analyte has been recorded to confirm the absence of contamination. Solution CV experiments on the dopants were done in 0.1 M tetrabutylammonium hexafluorophosphate (TBAHFP) in acetonitrile (ACN). Reduction potentials were recorded as half-wave potentials between corresponding anodic and cathodic peak potentials, representing the electron affinity $EA$ of the dopants. Further, CV was done with a spin-cast P3HT film on ITO as the working electrode using an electrolyte solution of 0.1 M TBAHFP in ACN and a scan rate of 0.02 V $s^{-1}$. Because of the great overlap between peaks, the half-wave potential could not be determined for the P3HT film and the oxidation onset in the anodic sweep was taken to represent the ionization energy $IE$ of P3HT. All redox potentials were measured against $Fc/Fc^+$ internal standard which, for broader comparability with literature values, was estimated as the commonly used −5.1 eV *versus* vacuum energy [75]. This number was chosen for best agreement of our value for the $IE$ of P3HT with its HOMO-DOS onset as determined by Bässler et al. through ER-EIS (the publication provided the

Gaussian distribution center $E_0 = -5.21$ eV and standard deviation $\sigma = 0.06$ eV while applying the onset definition of $E_0 + 2\sigma = -5.02$ eV) [64]. Note that $EA$ and $IE$ values in our work are given as positive numbers for the sake of clarity by associating higher $EA$ with higher dopant strength.

### 4.2.6 Density of States (DOS) Calculations

For the modeling of the occupation of the DOS in mixed host-dopant systems, we closely followed the method introduced in [62] and also detailed in [6, 33, 34, 63]. The molecular volume densities were taken from single-crystal structures: 4.0, 3.8, 3.9, and $3.7\times10^{21}$ cm$^{-3}$ for TCNQ [188], FTCNQ [189], F2TCNQ [190], and F4TCNQ [191], respectively, as well as $4.1\times10^{21}$ cm$^{-3}$ for P3HT [174]. The energy distribution of the HOMO and LUMO levels of each compound were assumed to follow a Gaussian distribution [62, 64, 107, 185] described by the position of its center and of $\sigma$, the standard deviation, equal to half the FWHM. Our experimental $IE$ and $EA$ values, as determined by CV, served as the distribution onsets of the host HOMO and the dopant LUMO, respectively, in the pristine materials, i.e. $IE$ ($EA$) lie higher (lower) than the center by twice the standard deviation $\sigma$.

For pristine P3HT, $\sigma$ values between 0.06 and 0.07 eV have been reported [64, 185, 186], notably, with the most recent study placing $\sigma$ to the lowest value of $\sigma_{\text{pristine}} = 0.06$ eV [64]. No such study exists for the other materials in our study, however, the same work by Bässler et al. which yields $\sigma_{\text{pristine}}$ for P3HT, provides $\sigma$ values for other OSCs as well. They report the smallest value for the polyphenylene MeLPPP with 0.05 eV and the largest one for the fullerene derivative $PC_{60}BM$ with 0.10 eV [64]. While MeLPPP is a polymer, it yields the lowest value reported by the authors; we therefore assume 0.05 eV as well for the FxTCNQ series since it can be expected that small molecules incur only limited geometrical disorder due to their rigid structure as compared to a polymer such as P3HT, which can undergo a plethora of conformational changes [192] and where geometrical disorder is a leading cause of DOS broadening; note that a greater diversity of conformations also affects the supramolecular structure, which presumably leads to a greater diversity of local polarization energies as well, broadening the DOS. This is also the very reason for keeping $\sigma$ fixed for the dopants in our calculations and for exclusively investigating the broadening of the host HOMO-DOS. We stress that this approach is different to related works where charge separation was studied between both small-molecule dopants and hosts [193, 194].

While we eventually find the occupancy of the dopant HOMO-DOS and host LUMO-DOS to be negligibly small (see figure C.10), these levels were still taken into account in our modeling, again, assuming $\sigma = 0.05\,eV$ except for P3HT. We used $IE = 9.50$ and 8.30 eV for TCNQ [195] and F4TCNQ [196], respectively. The values for FTCNQ and F2TCNQ were estimated by subtracting from our CV-derived $EA$ of FTCNQ and F2TCNQ the average energy gap between our recorded $EA$ and the reported $IE$ of TCNQ and F4TCNQ. For the P3HT LUMO-DOS we followed the findings of [64] which already provided $\sigma$ for the HOMO-DOS, i.e. $EA = 2.50$ eV with $\sigma = 0.17$ eV.

Having the Gaussian DOS defined, it was then imposed that the system be neutral. The occupancy of each energy level as well as the Fermi level were found self-consistently.

States were filled up to the Fermi level which was initialized at the midpoint between the host and dopant frontier energy levels; then the calculated charge density was used to solve the Poisson equation. The latter was done using a finite difference method (variable grid; second order, central-difference scheme; mixed Dirichlet and von-Neumann boundary conditions). The calculated potential was used to shift the Fermi level; a new charge density was generated from the updated Fermi level and then used for a new solution of the Poisson equation. These iterations were repeated until the change between iterations was less than one elementary charge per layer and meter squared. To explore the role of the host DOS broadening as a function of the dopant and its concentration $\chi$, these calculations were repeated for all systems using $\sigma$ values for the host ranging from 0.05 to 0.50 eV while keeping the center of the distribution fixed. For the dopant, the width of the DOS was held constant at a value of 0.05 eV, thus, essentially assuming all the broadening to occur in the host DOS. For all systems, calculations were done for $\chi$ from 0.001% to 50%.

### 4.2.7 Molecular Dipole and Quadrupole Moments DFT Calculation

Molecular structures for the TCNQs in their neutral form and in their radical anionic form were optimized using the $\omega$B97X-D functional [197] with 6-31+g(d,p) as the basis set. The ground state nature of the optimized molecules was verified *via* the absence of negative vibrational frequencies. These calculations were carried out in the Gaussian computational package (version 09 revision E.01) [198]. The wave functions were exported to calculate the molecular dipole and quadrupole moments analytically using the software Multiwfn [199].

### 4.2.8 Free Open-Source Software (FOSS)

For experimental data analysis and general figure creation, the following free/libre open source software released under the GNU General Public License (GPL) and other free-software licenses was employed. GIDvis (GPL v3.0; https://www.if.tugraz.at/amd/GIDVis/) was used for general GIXRD data analysis [179]. GIXRD cake slice-integrated intensity and FTIR fitting was done in Fityk (GPL v2.0; https://fityk.nieto.pl) [200]. Further data analysis and plotting was done in SciDAVis (GPL v2.0; http://scidavis.sourceforge.net/index.html) and Matplotlib for Python (under various BSD-compatible licenses; https://matplotlib.org) [201]. Figures were fine-tuned for publication using Inkscape (GPL v2.0; https://inkscape.org) and the Gnu Image Manipulation Program (GIMP; GPL v3.0; https://gimp.org).

## 4.3 Results

### 4.3.1 Optical Absorption Spectroscopy

A first idea of the host-dopant interactions at work can be inferred from optical absorption features in figure 4.2 which shows pristine and doped P3HT-FxTCNQ film

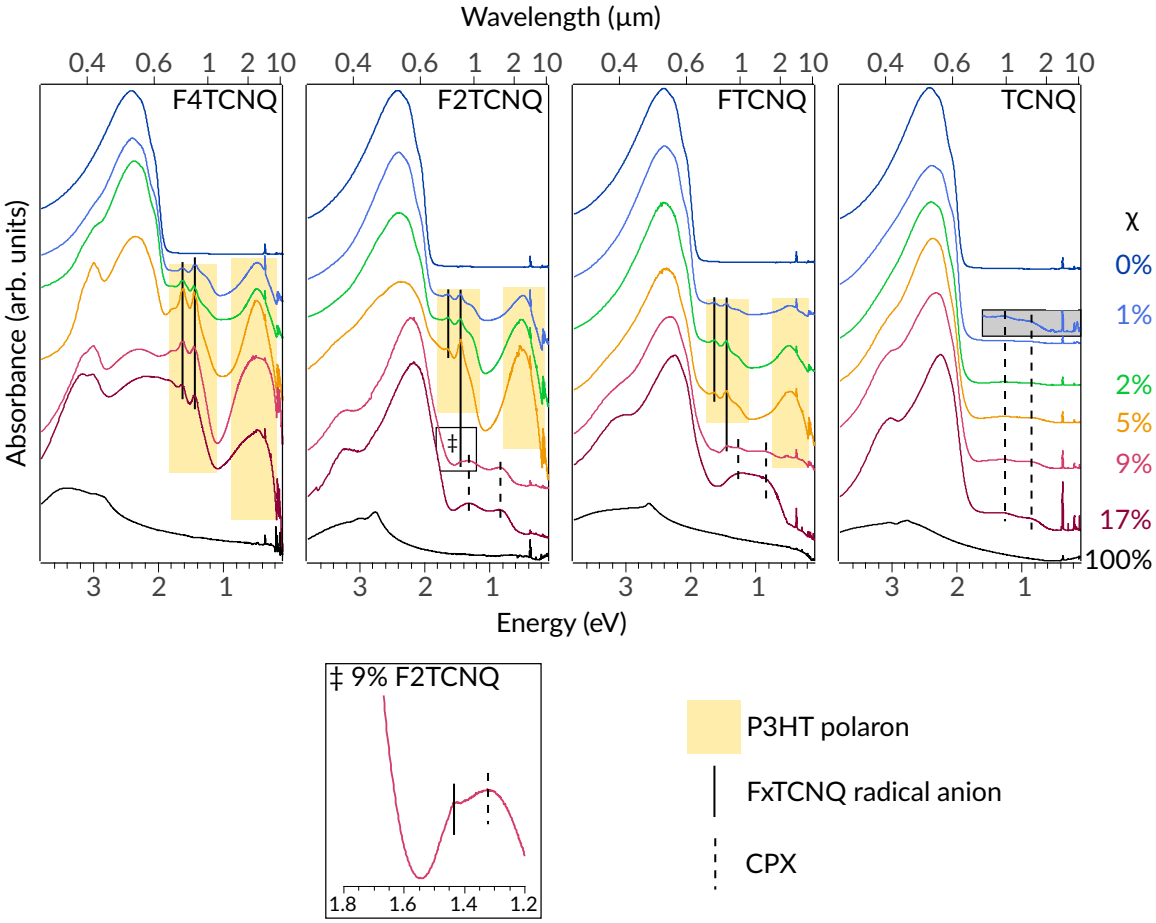


Figure 4.2: UV-vis/NIR data merged with FTIR thin-film absorbance spectra of P3HT doped with FxTCNQ (x=0,1,2,4) at increasing dopant molar ratios $\chi$ as well as those of the corresponding pure compounds. The gray box shows the four times magnified NIR region of the 1% TCNQ spectrum, highlighting the CPX peaks; sharp peaks below 0.5 eV are due to vibrational transitions in the mid infrared. All P3HT-containing spectra are normalized to the P3HT main absorption maximum centered around 2.4 eV; spectra of the pure dopants are scaled for the sake of clarity. Note that the FTIR data below 0.5 eV should only be regarded as a qualitative addition to the UV-vis/NIR data due to the differences between the two experiments that are explained in section 3.2.3.

absorbance spectra from UV-vis/NIR merged with the respective FTIR data. The fundamental absorption of pure P3HT has its onset at 1.95 eV which defines the optical gap. In the sub-gap region, distinct IPA features emerge in the spectrum for 1% F4TCNQ-doping, namely, two broad absorption bands around 0.5 and 1.6 eV stemming from the P3HT positive polaron (yellow shaded areas in figure 4.2) [34, 124–126], and two prominent features from the F4TCNQ radical anion at 1.45 and 1.63 eV [33, 34, 39, 122–124]. Another peak at 3.0 eV also is due to the F4TCNQ radical anion [34, 122], but cannot be regarded as a strong IPA indicator for its overlap with the fundamental transition of neutral F4TCNQ. These radical anion related features gain in magnitude with increasing F4TCNQ concentration, however, decrease again for 17%. Analogue IPA indicators simi-

lar to those in P3HT-F4TCNQ are also seen for F2TCNQ and FTCNQ, however, reduced to a small radical anion peak at 1.44 eV for $\chi$ = 9% and absent for 17%. In the range of 1%–5% where they appear prominently, these features show a trend of being weaker for dopants of lower *EA* [34]. Further, they are completely absent for doping with TCNQ, where the radical anion related absorption would be expected at 1.45 eV [123].

On the one hand, our 17% F4TCNQ spectrum is similar to that of P3HT sequentially doped with F4TCNQ in chloroform as investigated by Stanfield et al. [57] who confirmed the presence of IPA formation alongside CPX in their sample. The pure-CPX P3HT-F4TCNQ system isolated by Jacobs et al. [39] shows a red-shifted main P3HT absorption, which we also observe along a decrease in IPA features, as well as two broad CPX-assigned peaks at 0.66 & 1.15 eV, which are likely masked by the prominent polaron peaks in our data. For both F2TCNQ and FTCNQ, however, these CPX indicators are dominant at $\chi$ = 9% and make up the only sub-gap transitions for the 17% films. Likewise, they are the only sub-gap bands observed for all TCNQ concentrations, clearly rising in intensity with the dopant loading. These CPX peaks are observed at very similar energies for the different dopants (centered at 0.82 and 1.31 eV for F2TCNQ, 0.86 and 1.31 eV for FTCNQ, 0.87 and 1.28 eV for TCNQ; see vertical dashed lines in figure 4.2). The blue-shift of the lower energy peak with decreasing dopant *EA* is in line with previous work on quarterthiophene (4T) for the same dopant series (4T-FxTCNQ: 0.8, 1.0, 1.1, 1.2 eV for x = 4, 2, 1, 0, respectively) and stems from the larger energy offset between the hybridizing orbitals, i.e. the HOMO of 4T and the LUMO of the weaker dopants [34]. Then, the overall higher energies with 4T *versus* P3HT are explained as these transitions occur at lower energy for oligothiophenes of larger conjugation length (F4TCNQ-doped hexylated oligothiophenes: 0.9, 0.7, 0.7, 0.6 eV for 4, 6, 8, 10 repeat units, respectively [4]) as their *IE* scales inversely with the number of the thiophene repeat units [143].

On the other hand, our 17% F4TCNQ spectrum also compares to that reported by Tsokkou et al. [130] by drop-casting from common solution (but using chlorobenzene as solvent). They used an advanced deconvolution technique in combination with spectra of electrochemically doped P3HT to ascribe a broad peak at 0.92 eV to the formation of bipolarons. We do not observe any such indication of bipolaron formation for F2TCNQ, FTCNQ, or TCNQ, which is not surprising as even F4TCNQ has been long viewed as incapable of producing (measurable) amounts of bipolarons, restricting this phenomenon rather to stronger dopants or electrochemical doping [129–132]. For our 17% F4TCNQ spectra we find that the absorbance is less attenuated between the polaron peaks, as compared to the lower dopant concentrations (see also figure C.1), but no new distinct features can be made out. We recall that the CPX peaks are expected at 0.66 & 1.15 eV [39] and could be held for this additional absorbance, but also a possible bipolaron related contribution at 0.92 eV [130] would be situated directly between the polaronic transition energies and explain this absorbance. Another sign of bipolaron formation—rarely observable due to the often limited experimental spectral ranges—would be a peak around 0.35 eV (inferred from electrochemical doping [131] and computational analysis thereof [202]), which again would largely coincide with the broad low-energy polaron peak. We note, however, that the latter slightly shifts towards lower energy with increasing dopant loading which would indeed be in line with an additional bipolaron contribution. However, a bathochromic (hypsochromic) shift in the low-energy polaron peak has also been

attributed to an increase (decrease) in the polaron coherence length [58, 203, 204], which we cannot assess from our present data, overall making an assignment of bipolaron features too speculative for our data.

### 4.3.2 Vibrational Absorption Spectroscopy

Complementing optical absorption, insights into the charged state of FxTCNQs are commonly extracted from their vibrational modes, where an empirical relation between the degree of charge transfer and the shift of certain peaks was proposed [4, 33, 34, 36, 39, 49, 51–58]. While the $b_{2u}$ ring C=C stretching mode (occurring around 1600 $cm^{-1}$ for pristine F4TCNQ and at lower values for lesser fluorination [54, 205]; figure C.5) had been proposed as a highly reliable probe for the degree of charge transfer already decades ago [53], the $b_{1u}$ C≡N stretching mode (around 2200 $cm^{-1}$) has been commonly employed for that purpose [4, 33, 34, 36, 39, 49, 55–58]. This is likely because it is typically not masked by vibrational bands of common OSCs such as oligo- and polythiophenes [146, 147] (see '0%' spectra in figure 4.3).

Figure 4.3 shows the FTIR spectra in the region of the C≡N modes for the pristine materials alongside F4TCNQ-, F2TCNQ-, FTCNQ-, and TCNQ-doped P3HT (ring C=C stretching modes in figure C.5); it further includes spectra of the same samples after one week of aging (see section 4.2 for details) to assess possible degradation on the timescale of experiments that could not be done under inert atmosphere (discussion in appendix A). Peak positions reported for the C≡N modes of the neutral dopant ($\nu_0$) and the dopant radical anions ($\nu_1$) are $\nu_0 = 2227\,cm^{-1}$ and $\nu_1 = 2194\,cm^{-1}$ for F4TCNQ [53], $\nu_0 = 2227\,cm^{-1}$ and $\nu_1 = 2183\,cm^{-1}$ for TCNQ [51], and $\nu_0 = 2231$ and $2224\,cm^{-1}$ for F2TCNQ and FTCNQ, respectively [34]; as the F4TCNQ and TCNQ $\nu_0$-positions coincide and show a comparable shift upon ionization, we assume the $\nu_1$ values to be similarly shifted from $\nu_0$ for both FTCNQ and F2TCNQ.

In good agreement with the $\nu_0$ values, we find the neutral dopant peaks (dotted vertical lines in figure 4.3) at 2226, 2231, 2223, and $2225\,cm^{-1}$ in the 100% spectra of F4TCNQ, F2TCNQ, FTCNQ, and TCNQ, respectively. Notably, these peaks are also present in 17% F2TCNQ and FTCNQ which indicates overdoping, i.e. the limit of how many dopants can undergo charge-transfer interactions with P3HT is exceeded; the same is potentially true for 17% TCNQ as well, however, the peak cannot be resolved unambiguously as it is masked by the neighboring CPX peak (see figure C.4). While the ring C=C modes are not as easily interpreted as the C≡N modes due to the presence of P3HT features in the spectral vicinity, our data is exceptionally clear on the 17% F4TCNQ sample. Most remarkably, although taken from the very same FTIR spectrum, the ring C=C stretching in 17% F4TCNQ provides a clear peak for the neutral dopant ($1597\,cm^{-1}$ in figure C.5; cf. [53, 145, 205]) while the charge neutral C≡N modes are not observed.

Regarding the indicators for IPA (marked by vertical solid lines in figure 4.3), no $\nu_1$ peak is seen with TCNQ-doping. In contrast, 1% F4TCNQ-, F2TCNQ-, and FTCNQ-doped films show $\nu_1$ at 2192 ($\nu_{1A}$), 2184, and 2181 $cm^{-1}$, respectively, which shift to 2185 ($\nu_{1B}$), 2178, and $2179\,cm^{-1}$ for $\chi = 9\%$; $\nu_{1A}$ and $\nu_{1B}$ are labelled for a later discussion (*vide infra*). The $\nu_1$ position for 17% is not considered in the analysis for $\nu_{1B}$ because it only appears as a shoulder to other peaks. Such a weak appearance, again, is quite astonishing

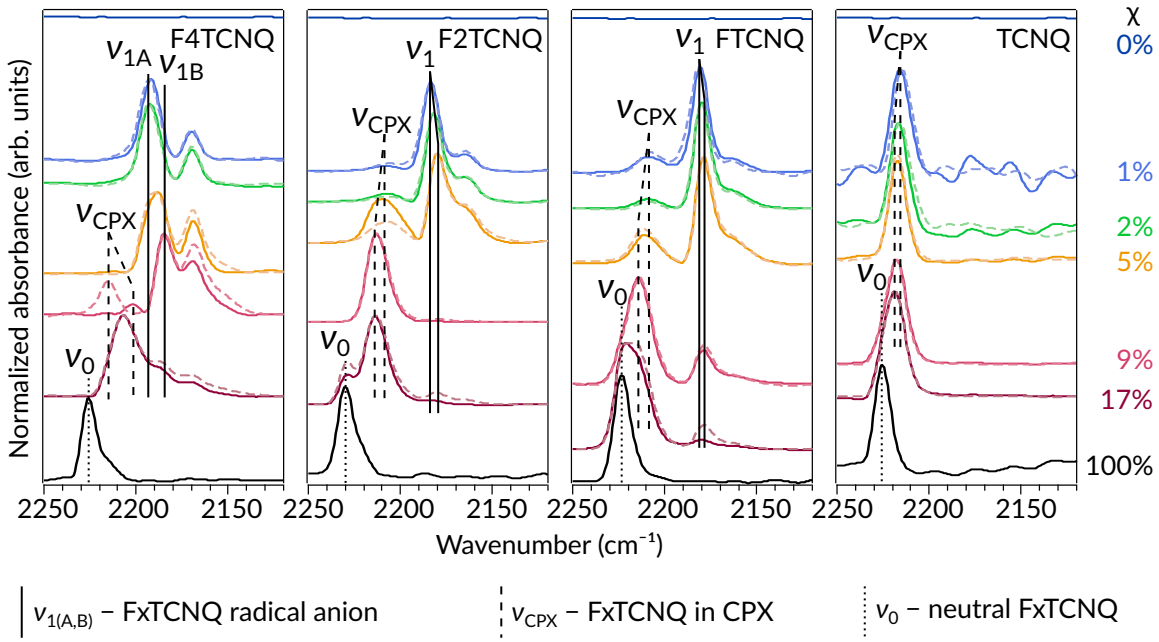


Figure 4.3: FTIR thin-film absorbance spectra of P3HT doped with FxTCNQ (x=0,1,2,4) at increasing dopant molar ratios $\chi$ as well as those of the corresponding pure compounds (in the region of the dopant C≡N stretching modes). Solid-line spectra were recorded under inert $N_2$ atmosphere and faded dashed-line spectra stem from the same samples after one week of aging and 1 h of full exposure to ambient conditions (see section 4.2 and a discussion in appendix A); peak positions compared in the text are marked by vertical lines. All spectra recorded for doped films are normalized to their respective absorption maxima. The pure-P3HT spectra (0%) are magnified by the same factor as the spectrum of the 1% doped film; the raw data are given in figure C.3.

for F4TCNQ since both optical absorption and the ring modes (1530 and 1500 cm$^{-1}$ in figure C.5) speak for a stronger presence of the radical anion at that dopant loading.

Additional peaks $\nu_{CPX}$ (dashed vertical lines) can be observed in-between our so-far assigned $\nu_0$ and $\nu_1$ values. F2TCNQ-, FTCNQ-, and TCNQ-doping yield $\nu_{CPX}$ at 2208, 2209, and 2216 cm$^{-1}$ for $\chi$ = 1% which shift with increasing dopant loading towards 2214, 2215, and 2219 cm$^{-1}$ for 17%, respectively. For F4TCNQ we find $\nu_{CPX}$ = 2202 cm$^{-1}$ for 9% and 2207 cm$^{-1}$ for 17% which are in good agreement with literature values on CPX formation in P3HT-F4TCNQ [39, 49, 55–58, 60], most importantly, with the work by Jacobs et al. [39] where optical absorption data showed virtually no IPA features. The correlation of $\nu_{CPX}$ with the CPX features of our optical absorption spectra is trivial for TCNQ. It is also safe to assume all our other $\nu_{CPX}$ values to stem from CPX formation since their presence rises with $\chi$ like the CPX optical absorption features, and because their position in-between the $\nu_0$ and $\nu_1$ values suggests fractional charge transfer [51, 52]. Nevertheless, we would like to highlight the nontriviality of the latter assessment as, e.g. $\nu_1$ for F4TCNQ had also been found at higher wavenumbers, mostly depending on its cationic partner species [53, 54].

Overall, our combined optical and vibrational data are generally in line with previous reports indicating that higher F4TCNQ content in P3HT films favors the formation of CPX over IPA beyond a threshold in dopant concentration [39, 49] and shows the same to be true for F2TCNQ and FTCNQ.

### 4.3.3 Grazing-Incidence X-Ray Diffraction (GIXRD)

To gain insight into the differences in crystal structure between IPA, CPX, and mixed IPA/CPX systems we collected GIXRD data on both doped and pure P3HT films. Considering the semi-crystalline nature of P3HT, it must be kept in mind that while the spectroscopic methods above probe the whole sample, both amorphous and crystalline regions, GIXRD provides information exclusively on the latter. We find the pure P3HT films to be in a preferential edge-on orientation where the out-of-plane features represent the ($h$00) lattice planes (reciprocal space maps in figures C.8 and C.7), which is a common finding for such films [206]. This feature corresponds to the lamellar stacking direction and translates into a lattice spacing of $d_{100}$ = 16.5 Å. The present in-plane feature is assigned to the (020) $\pi-\pi$ interchain stacking with $d_{020}$ = 3.83 Å (with two P3HT chains in the unit cell [174], '$d_{020}$' effectively describes half the unit cell in [010] direction, here). This is also in line with similarly processed P3HT films in literature [2, 34, 39, 49, 56, 57, 141, 207] and representative of the so-called type-I structure with the stacked polymer backbones tilted by approximately 26° toward the crystallographic $b$-axis, notably, without side-chain intercalation [174, 208].

For enhanced comparability between the doping cases, a select range of cake slice-integrated intensities in the vicinity of the $q_z$ (out-of-plane) and $q_{xy}$ (in-plane) axis in figure C.8 are depicted in figures 4.4(a) and (b), respectively. Upon doping with F4TCNQ we observe $d_{100}$ to increase gradually with $\chi$ to a value of 18.5 Å for 5%. From there it again decreases to 17.0 Å at 17% where the corresponding peak is joined by a very strong shoulder yielding 14.2 Å. In turn, $d_{020}$ gradually decreases with $\chi$ to 3.43 Å for 17%. The smaller $d$ values for $\chi$ = 17%, i.e. $d_{100}$ = 14.2 Å paired with $d_{020}$ = 3.43 Å, can be assigned to a crystalline CPX phase and are well in line with the 17% F4TCNQ-doped P3HT sample reported by Jacobs et al. [39] which exclusively showed CPX, as well as the prominent presence of $\nu_{\mathrm{CPX}}$ in our FTIR data at this dopant loading. The according (020) peak for 17% F4TCNQ and that of pure P3HT are remarkably sharper, with a FWHM smaller by about 30% than that of the 1%-9% cases. It is therefore likely that the decrease in $d_{020}$ from 9% to 17% is not a continuous trend but the leap to another polymorph of higher crystalline quality. Indeed, a smaller $d_{020}$ is also expected resulting from a reduced backbone tilt in a non-mixed $\pi-\pi$ stack of P3HT backbones as a consequence of dopant radical anions residing in the hexyl chain region; the latter being commonly indicated by the increased $d_{100}$ [2, 36, 56, 58, 138–142] which we also observe for $\chi = 1\% - 9\%$, again in line with our spectroscopic data showing dominant IPA representation.

For 5%-17% F4TCNQ an additional peak appears corresponding to a lattice spacing of 3.88 Å. This peak is small and consistent for all three $\chi$ values, but it showed increased relative intensity for higher dopant content in recent studies [49, 207]. As discussed in detail in section 4.4.1, we assign this peak to $d_{020}$ of P3HT regions that did not include any dopant molecules during their growth.

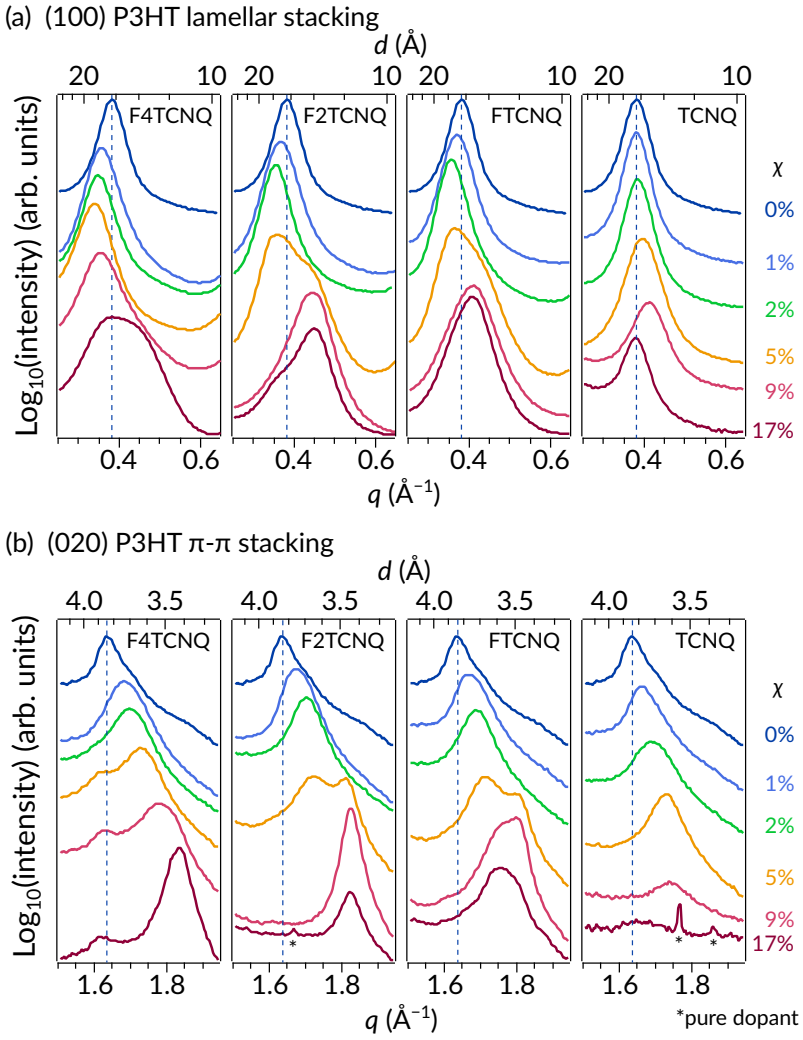


Figure 4.4: GIXRD intensities from integrated cake slices in the vicinity of the (a) $q_z$ and (b) $q_{xy}$ axis from reciprocal-space maps in figure C.8 on films of pure P3HT as well as doped with FxTCNQ (x=0,1,2,4) at increasing dopant molar ratios $\chi$; focused on the (a) (100) and (b) (020) peaks; dashed vertical lines serve as a guide to the eye, indicating the pure-P3HT peak; pure TCNQ and FTCNQ features are indicated according to [209] and [189], respectively.

As with F4TCNQ, also in our F2TCNQ- and FTCNQ-doped samples we see a gradual increase in $d_{100}$ with $\chi$, now, to 17.8 and 17.5 Å for 5% where its peak is joined by a shoulder indicating 14.1 and 15.3 Å, respectively. This shoulder then becomes the only observed peak for 9% and 17% FTCNQ as well as 9% F2TCNQ; for 17% F2TCNQ it is again accompanied by a small shoulder corresponding to 17.8 Å. The $d_{020}$ values are found to decrease with increasing $\chi$ from 3.83 Å (pristine P3HT) to 3.65 Å (5% F2TCNQ) and 3.68 Å (5% FTCNQ), where a prominent shoulder appears for 3.46 and 3.47 Å, respectively. For 9% and 17% F2TCNQ this shoulder turns into the only peak, but for FTCNQ it is still accompanied by a feature corresponding to a spacing of 3.59 Å. In general, we can assign the (100) features yielding 17.5 to 17.8 Å to IPA formation as they mirror rather IPA

than CPX occurrence according to the FTIR results (C≡N stretching modes), especially, the disappearance and return of the IPA peak at 9% and 17% F2TCNQ, respectively; complementarily, the features yielding 14.1 to 15.3 Å can be associated with CPX formation. The gradual increase in $d_{020}$ with $\chi$ towards a value of $\approx 3.7$ Å *versus* the sudden appearance of a shoulder at $\approx 3.5$ Å reminds of the association with crystalline IPA *versus* CPX phases, respectively, suggested for our F4TCNQ-doped samples (*vide supra*). With these assignments and considering their similarity in $d$ values, it is sensible to assume that the assignments of the IPA and CPX crystalline phases in F4TCNQ-doped P3HT are equally applicable to the F2TCNQ and FTCNQ cases.

In our CPX-only system of P3HT-TCNQ, $d_{100}$ and $d_{020}$ gradually decrease up to 9% to values of 15.1 and 3.60 Å, respectively, but then abruptly recover the values of pure P3HT for 17%, where the (020) peak is found largely attenuated for $\geq$ 9%. The trend up to 9% TCNQ matches that observed with the fluorinated dopants interpreted as the emergence of a crystalline CPX phase, but with $d$ values dependent on the dopant loading and peak widths consistently larger than those of the pristine film, thus indicating less order. We note that, in general, all our dopants show Bragg reflections of pure-dopant crystals at 17% (best seen in the 2D reciprocal space maps, figures C.8 and C.7) which is clear evidence for pure dopant precipitation.

### 4.3.4 Conductivity

In order to understand how the occurrence of IPA and CPX formation impacts the charge transport in P3HT, we recorded the thin-film conductivity (figure 4.5(a), table C.1). For increasing $\chi$, a maximal rise in conductivity by over five orders of magnitude from pure P3HT to $\chi$ = 9% F4TCNQ is observed. For the weaker dopants we observe maximal increases of four and two orders of magnitude for 5% F2TCNQ and FTCNQ, respectively. Notably, conductivity saturates for higher F4TCNQ content. Recalling the discussion of our UV-vis/IR data (figures 4.2 and C.1) this can both be due to unfavorably high bipolaron-to-polaron ratios [129, 210] and the increased CPX occurrence which reduces the doping efficiency. For the other dopants, the trends are not so clear at higher $\chi$ since their values decrease when increasing the dopant loading towards 9% F2TCNQ and 17% FTCNQ. For TCNQ, the conductivity only decreases with increased dopant concentration until 9% where it reaches an even one-order-of-magnitude lower value than that of pure P3HT.

At 17%, F2TCNQ and TCNQ show significant conductivity increases over their 9% data point. However, since the presence of neutral dopants is indicated by the 17% FTIR spectra and the signature of pure dopant precipitation in the respective GIXRD data, the corresponding conductivity values should be taken with caution because pure-dopant domains can also contribute to the conduction in that low range of conductivity [188]; those films are, in fact, at the threshold between FxTCNQ-doped P3HT and 'P3HT-doped FxTCNQ' and using the term 'doping' does not appear entirely justified anymore. Note that, while highly reproducible up to 9% dopant loading, at 17% we found conductivity values to become less reliable for nominally identical preparation parameters, e.g. we once observed a further, though slight, decrease for 17% TCNQ over its 9% data point, which points to a subtle dependency of the film morphology on parameters beyond the control of our experimental setup in highly doped systems.

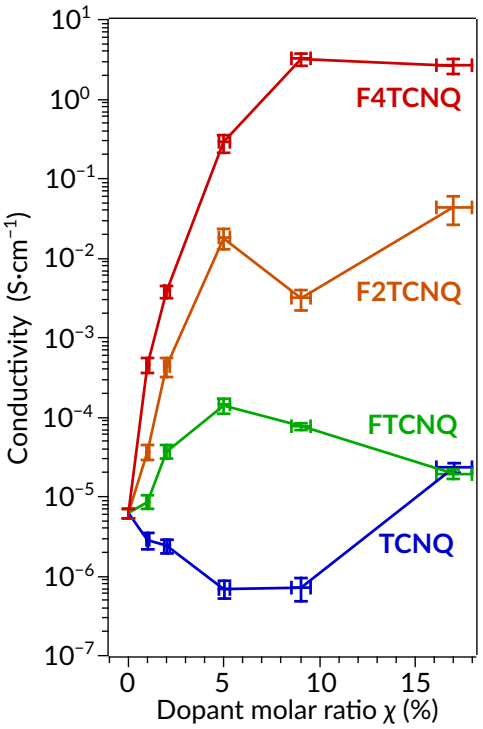


Figure 4.5: Thin-film conductivity of pure P3HT and of FxTCNQ (x=0,1,2,4) doped P3HT at increasing dopant molar ratios $\chi$; lines connecting the data points serve as a guide to the eye; values provided in table C.1.

With this in mind, in terms of both dopant strength and concentration, stronger IPA signals in our spectroscopic data clearly correlate with an increase in conductivity while more prevalent CPX formation is detrimental to it, yielding a saturation in conductivity with F4TCNQ and even (relative) decreases with the weaker dopants.

### 4.3.5 Cyclic Voltammetry (CV)

To further investigate the IPA and CPX occurrence in P3HT for the TCNQ derivatives, we investigated their $EA$ values in relation to the host $IE$. To this end, we employed CV-derived redox potentials $V_{\text{redox}}^{\text{HOMO}}$ and $V_{\text{redox}}^{\text{LUMO}}$ of host and dopant as a proxy for $IE$ and $EA$, respectively (see section 4.2 for conversion between $V_{\text{redox}}$ *versus* ferrocene/ferrocenium ($Fc/Fc^+$) and $EA/IE$ values *versus* vacuum energy). A recent publication by Wegner et al. [48] found the $V_{\text{redox}}$ values derived from CV to be more reliable for predicting IPA formation than $IE$ and $EA$ obtained from UPS and inverse photoelectron spectroscopy (IPES), respectively. They saw the greatest agreement in solution and argued that, while UPS and IPES are subject to the collective electrostatic properties of the sample, the charge transfer between analyte and electrode/electrolyte in CV occurs on the molecular level, similar to the doping process. For the solid state, the authors observed that the percentage of ionized dopants was systematically larger than in solution and, thus, deviated from the prediction based on CV data, but it remained still superior to UPS/IPES

derived values. This might seem counter-intuitive as the latter are solid-state techniques, in contrast to CV done in solution, however, their pronounced surface-sensitivity and the orientation dependence of these values [79] together with final-state effects [80] can provide a large spread in these values. In contrast, Sweetnam et al. [76] argued that, if the analyte is deposited as a thin film on the working electrode, solid-state influences are effectively probed by the migration of electrolyte into the film; more recently, electrolyte-anion intercalation into the P3HT side-chain region had been shown [78], which once more highlights the value of CV. For the present study, we performed CV on the dissolved dopants thus obtaining *EA* values largely based on a molecular level, combined with CV performed on a P3HT thin film providing an *IE* value which does include solid-state effects. Clearly, also this approach is only an approximation to the actual effects experienced by each individual dopant molecule but, in our view, probably the most justified one.

We recently published the present data obtained for F4TCNQ, FTCNQ, TCNQ, and P3HT in [6] and provide them for the reader's convenience together with data on F2TCNQ (corresponding voltammograms in figure C.9). On that basis, F4TCNQ, F2TCNQ, FTCNQ, and TCNQ exhibit an *EA* ($V_{\text{redox}}^{\text{LUMO}}$ *versus* $Fc/Fc^+$) of 5.31 eV (0.21 V), 5.01 eV (−0.09 V), 4.97 eV (−0.13 V), and 4.91 eV (−0.19 V), respectively; our pristine P3HT film on ITO shows an *IE* ($V_{\text{redox}}^{\text{HOMO}}$) of 5.21 eV (0.11 V). Within the error margin expected for energy levels derived from CV (±0.1V) [75], our data is in very good agreement with literature values of both the dopants [48] and P3HT [76], where $Fc/Fc^+$ was employed as a reference standard as well. The corresponding IPES derived *EA* values of TCNQ, FTCNQ, F2TCNQ, and F4TCNQ in literature are 4.23, 4.55, 4.59, and 5.08 eV, respectively [47], while UPS yields 4.8 eV for the *IE* of P3HT [148]. We note that all CV-derived values hinge on the the *IE* of Fc and because there is no conclusive consensus on the potential of the $Fc/Fc^+$ redox pair *versus* vacuum [75]; using 4.8 instead of 5.1 eV for the *IE* of Fc would bring above IPES values into good agreement with our CV-derived ones. For P3HT good agreement is also maintained by employing the linear correlation between $V_{\text{redox}}^{\text{HOMO}}$ from CV and *IE* from UPS as formulated by D'Andrade et al. [211]. Notably, while the fact that FTCNQ and F2TCNQ are very close in *EA* in our dataset is well reflected in the IPES data of [47], the *EA* of TCNQ is significantly lower in the latter, which might result from orientation effects common to UPS/IPES relevant for ordered molecular assemblies [79, 212, 213].

### 4.3.6 Density of States (DOS) Calculations

Based on our CV data, only the *EA* of F4TCNQ would exceed the *IE* of P3HT and, thus, allow for IPA formation. However, there is no doubt from our spectroscopic data that integer charge transfer occurs with F2TCNQ and FTCNQ as well. In a recent study [6], we followed the idea that this is due to a broadening of the host HOMO-DOS as a result of doping-induced disorder [214] and performed semi-classical modeling to assess how IPA formation can be triggered by disorder, leading to greater variance in polarization energy and polymer conjugation length [107]. Our calculations were based on the common assumption that both the HOMO and LUMO DOS are well-represented by Gaussian distributions [62, 64, 107, 185]; for further details see section 4.2. We focused on the

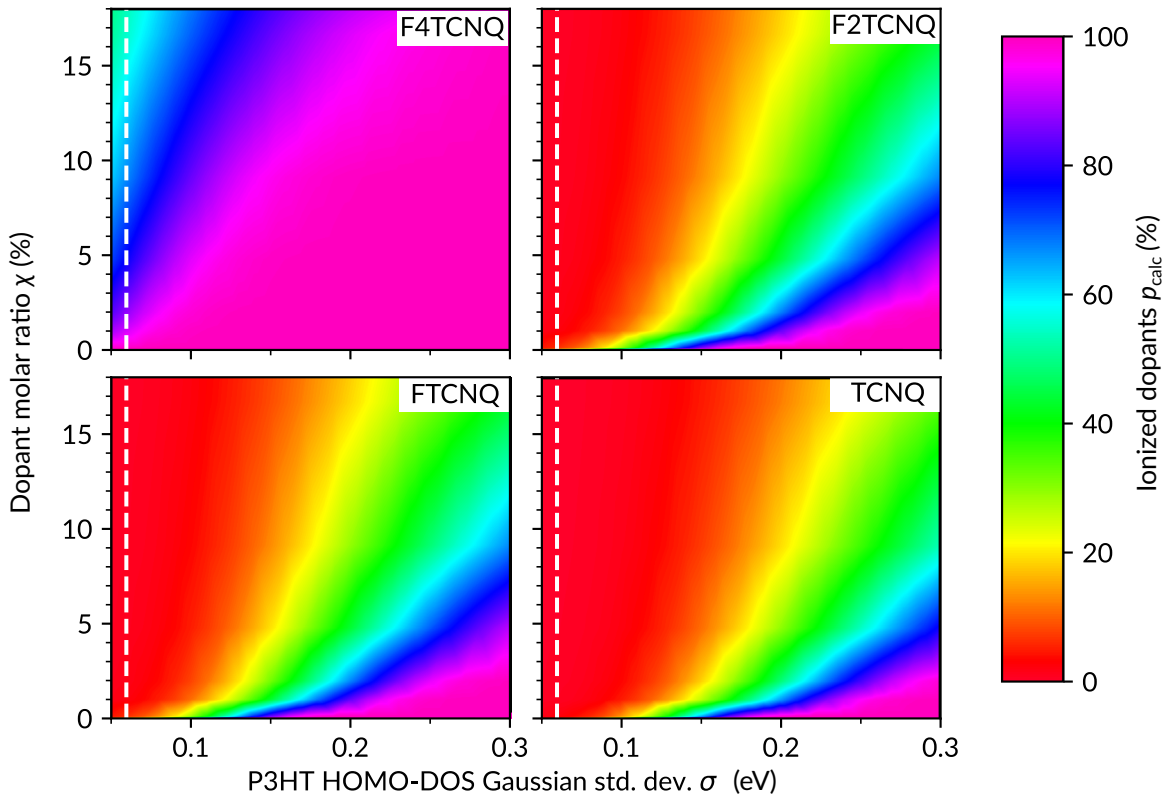


Figure 4.6: Ionized dopant percentage $p_{\text{calc}}$ as calculated for increasing P3HT Gaussian HOMO-DOS width (standard deviation) $\sigma$ for doping with FxTCNQ (x=0,1,2,4) with increasing dopant molar ratios $\chi$. Vertical dashed lines mark $\sigma = 0.06\,\text{eV}$, the experimentally obtained value for pristine P3HT [64].

low-doping regime only and investigated P3HT doped with 2% F4TCNQ, FTCNQ, and TCNQ. Here, we now provide more comprehensive and systematic data by modeling all experimentally studied cases of the previous sections, that is, 1%, 2%, 5%, 9%, and 17% F4TCNQ-, F2TCNQ-, FTCNQ-, and TCNQ-doped P3HT. F2TCNQ, FTCNQ, and TCNQ with their gradual decrease in $EA$, lying just 0.2-0.3 eV below the $IE$ of P3HT, appear ideally-suited to probe the extent of Gaussian HOMO-DOS tailing of P3HT in the doping process.

All calculated percentages of ionized dopants $p_{\text{calc}}$ resulting from our modeling are visualized in figure 4.6; colors represent $p_{\text{calc}}$. Within the range of our experimental data, our modeling clearly highlights three trends that lead to higher $p_{\text{calc}}$: (i)increased host HOMO-DOS $\sigma$ (less order), (ii) lower $\chi$ (fewer dopants) for (iii) higher dopant $EA$ (stronger dopants).

We then investigate $p_{\text{CN}}$, the ionized dopant percentage estimated from FTIR deduced from the area of the main C≡N stretching mode peak of the dopant anion relative to that of the CPX and/or neutral main peaks (if present). Table 4.1 lists the $\sigma$ values for which $p_{\text{calc}} \approx p_{\text{CN}}$; $\sigma = 0.06\,\text{eV}$ is the value for pristine P3HT, as recently determined experimentally [64] (dashed line in figure 4.6). The highest value, $\sigma = 0.23\,\text{eV}$, is obtained for

Table 4.1: Dopant ionization percentage $p_{CN}$ as estimated from the relative fitted area of the radical anion main C≡N stretching-mode *versus* the CPX and neutral peaks in FTIR (figure 4.3), and P3HT HOMO-DOS Gaussian standard deviation $\sigma$ as calculated to yield that $p_{CN}$; 0.06 eV is the experimentally obtained value for pristine P3HT [64].

| | F4TCNQ | | F2TCNQ | | FTCNQ | | TCNQ | |
|---|---|---|---|---|---|---|---|---|
| $\chi$ (%) | $p_{CN}$ (%) | $\sigma$ (eV) | $p_{CN}$ (%) | $\sigma$ (eV) | $p_{CN}$ (%) | $\sigma$ (eV) | $p_{CN}$ (%) | $\sigma$ (eV) |
| 1 | 100 | 0.10 | 90 | 0.19 | 80 | 0.19 | 0 | ≤0.06 |
| 2 | 100 | 0.11 | 80 | 0.20 | 88 | 0.23 | 0 | ≤0.06 |
| 5 | 100 | 0.14 | 53 | 0.20 | 32 | 0.18 | 0 | ≤0.06 |
| 9 | 88 | 0.11 | 0 | <0.06 | 14 | 0.15 | 0 | ≤0.06 |
| 17 | 32 | <0.06 | 2 | 0.08 | 9 | 0.15 | 0 | ≤0.06 |

Table 4.2: P3HT HOMO-DOS Gaussian standard deviation $\sigma$ calculated for the threshold to IPA nucleation as recently modeled [184]. It is represented here by the ionized dopant molar ratio $\chi_{IPA} \approx 0.1\%$, excluding non-ionized dopants from the total dopant molar ratio $\chi$; 0.06 eV is the experimentally obtained value for pristine P3HT [64].

| $\chi$ (%) | $\sigma$ (eV) for $\chi_{IPA} \approx 0.1\%$ | | | |
|---|---|---|---|---|
| | F4TCNQ | F2TCNQ | FTCNQ | TCNQ |
| 1 | <0.06 | 0.08 | 0.10 | 0.12 |
| 2 | <0.06 | 0.07 | 0.09 | 0.11 |
| 5 | <0.06 | 0.06 | 0.08 | 0.10 |
| 9 | <0.06 | <0.06 | 0.07 | 0.09 |
| 17 | <0.06 | <0.06 | 0.06 | 0.09 |

2% FTCNQ which is comparable to the 0.26 eV suggested in previous studies on molecular doping [193, 194]. Note that, while the high-$p_{CN}$ samples of 1%-2% F2TCNQ and FTCNQ content yield about twice the $\sigma$ value of the respective F4TCNQ samples, one must keep in mind that $p_{calc}$ is calculated with the minimum $\sigma$ required, thus, all three fluorinated dopants might well induce similar amounts of DOS broadening. Generally, we can say that $\sigma$ must increase significantly over its pristine-P3HT value to explain the experimentally found $p_{CN}$ for F4TCNQ-, F2TCNQ-, and FTCNQ-doped P3HT, with only few exceptions (17% F4TCNQ, 9% F2TCNQ). Thus, broadening of the P3HT HOMO-DOS up to a factor of three upon doping emerges as a natural explanation for this finding in order to rationalize the observed $p_{CN}$ values (see section 4.4.3 below).

In our previous study [6] we hypothesized that an initially small percentage of IPA content causes $\sigma$ broadening and, subsequently, ionization of further dopants. In the same vein, we also consider the nucleation effect for IPA formation at its threshold-concentration $\chi_{IPA} \approx 0.1\%$ (excluding non-ionized dopants from the total dopant molar ratio $\chi$), as postulated in the aforementioned study by Wu et al. [184]. As $\chi_{IPA}$ regards only ionized dopants *versus* P3HT, it best corresponds to our data when we only

consider the ionized portion at the dopant molar ratio $\chi$, which we can calculate since the respective $p_{\mathrm{calc}}$ values provide us with the fraction of ionized dopants:

$$\chi_{\mathrm{IPA}} = p_{\mathrm{calc}} \left( \frac{p_{\mathrm{calc}}}{100\%} + \frac{100\%}{\chi} - 1 \right)^{-1}. \tag{4.1}$$

$\sigma$ data points where the $\chi_{\mathrm{IPA}} \approx 0.1\%$ threshold is reached, are listed in table 4.2. Most remarkably, less broadening is needed for higher dopant loading, suggesting a higher probability for the crystalline IPA phase—a trend opposite to our experimental data which shows increased CPX formation, instead.

## 4.4 Discussion

### 4.4.1 Interpretation of C≡N Stretching Modes

Due to the exposed position of the C≡N bonds at the periphery of the dopants, their vibrations are highly sensitive to the environment [2, 53, 54, 58–60]. This includes strong influence of the countercharge location [54], of hydrogen transfer towards the dopant [59, 60], and the vibrational Stark effect from varied degrees of polaron delocalization [58]. Therefore, to deduce IPA, CPX, and neutral dopant content from the C≡N modes despite the convolution of these various influences, correlations with other experimental data such as optical absorption features must be taken into account.

In this light, we bring attention to our previous interpretation [2] of the gradual shift of the F4TCNQ radical anion C≡N modes from $\nu_{1\mathrm{A}} = 2192\,\mathrm{cm}^{-1}$ for $\chi = 1\%$ to $\nu_{1\mathrm{B}} = 2185\,\mathrm{cm}^{-1}$ for 9%. In that work, we assigned the GIXRD feature yielding $d_{020} = 3.88\,\text{Å}$ (here, seen for 5%-17% F4TCNQ) to a crystalline IPA phase with a host-dopant mixed stack and observed that its occurrence correlated with the $\nu_{1\mathrm{A}}$ peak in FTIR. However, our present data shows no such correlation because of its weak, consistent appearance independent from the dopant loading, which is in contrast to the concomitant reduction we observe in $\nu_{1\mathrm{A}}$. Further, forcing the dopant into backbone stacking by using a P3HT derivative with branched-out hexyl substitutions was shown to exclusively result in CPX formation [215] and the placement of the dopant next to a conjugated polymer backbone instead of the alkyl-chain region has recently been shown to come with >0.5 eV penalty to the effective dopant *EA* [69]. Subsequently, we rather consider that this lattice spacing lies within the error margin of the pristine P3HT $d_{020}$ and, therefore, is indicative of regions that did not include dopant molecules during growth. As for the interpretation of the C≡N modes, we follow the recent study by Stanfield et al. [57] ascribing the peak shift to the vibrational Stark effect which the C≡N groups of the dopant are susceptible to; the authors reported that the P3HT polaron delocalization must increase from 6 monomer units, marked by the $\nu_{1\mathrm{A}}$ peak position in figure 4.3, to 7.5 monomer units, marked by $\nu_{1\mathrm{B}}$, hence, changing the electric field causing the Stark effect. However, we note that Stanfield et al. based their view partially on the shift of the low-energy polaron peak which, as discussed above, can not only be interpreted as a change in polaron coherence but also be due to bipolaron formation. Therefore, it is conceivable that the latter is the basis for this electric-field change and that $\nu_{1\mathrm{B}}$ is another hint of bipolaron formation.

We also want to highlight here the discrepancy between the C≡N (figure 4.3) and the ring C=C modes (figure C.5) in 17% F4TCNQ found in our data. The C≡N modes exhibit only a small peak of the radical anion ($\nu_1$) and no peak of the neutral dopant ($\nu_0$), in marked contrast to the ring C=C vibrations providing clear indication of the dominance of IPA and of neutral dopants being present—the latter being supported by the pure-dopant crystallite occurrence in our GIXRD data. This suggests that the oscillator strengths are incomparable, likely, as different molecular environments impact the vibrational modes [54]; this makes the magnitude of the CPX peak ($\nu_{\mathrm{CPX}}$) in the C≡N modes potentially overestimate the CPX population in comparison to the ring C=C modes. This discrepancy once more reminds us that the assignment of these IPA/CPX indicators and, in particular, their use for quantifying the relative population of IPA *versus* CPX in a given system must be handled with great prudence.

### 4.4.2 The Scope of our DOS Calculations

The potential over-representation of the CPX population by the C≡N stretching modes (*vide supra*) entails that the derived percentages of ionized dopants $p_{\mathrm{CN}}$ and, subsequently, the P3HT HOMO-DOS widths $\sigma$ associated with them through our modeling, must both be regarded as lower limits; e.g. we cannot exclude that TCNQ does induce $\sigma$ broadening as this cannot be captured by our data. For 9% F2TCNQ and 17% F4TCNQ, $p_{\mathrm{CN}}$ would be associated with a $\sigma$ value well below the 0.06 eV that had been determined experimentally for pristine P3HT [64]. Such an obvious underestimation of $\sigma$ for these cases of high CPX occurrence is likely due to the fact that no explicit driving force that is intrinsic to CPX formation and counters IPA formation, is modeled in our approach. Therefore, the host HOMO-DOS broadening as a driving force behind IPA formation will be underestimated. An additional CPX driving force would be required to be modeled such as the aforementioned work by Wu et al. [184], where they suggest the formation of crystalline IPA and CPX phases being subject to nucleation effects and the overall change in free energy, which however goes beyond the scope of our work. Consequently, in our discussion of the drivers behind IPA and CPX formation, we essentially employ the results of our DOS modeling only in IPA-rich cases and lean more firmly on our experimental findings when significant CPX formation occurs.

On a different note, while our $\sigma$ values in IPA-dominated cases align well with recent studies focusing on charge transport [193, 194], we acknowledge that our approach focusing on DOS modeling is agnostic of shifts in the effective $IE/EA$ not directly related to the DOS *per se*. On the one hand, Li et al. [70] had recently calculated that the $EA$ of F4TCNQ is effectively reduced by up to 0.7 eV when placed into an electron-donor host-matrix, exemplified by pentacene and $N$,$N'$-di(1-naphthyl)-$N$,$N'$-diphenyl-(1,1′-biphenyl)-4,4′-diamine (known as NPB or NPD). On the other hand, a more recent publication by Comin et al. [69] showed that F4TCNQ residing in the alkyl side-chain region of poly(2,5-bis(3-tetradecylthiophen-2-yl)thieno[3,2-*b*]thiophene) (known as PBTTT) effectively gains >0.5 eV in its $EA$ as compared to a mixed $\pi-\pi$ stack of F4TCNQ with the polymer backbone. Therefore, as our GIXRD data indicates the dopant radical anion residing in the hexyl-chain region, it is plausible to assume the latter effect on $EA$ to (partially) compensate for the former. We stress that we might import such

effects into our model by using an $IE$ value derived from CV on solid-state P3HT (*vide supra*) while the anion ($PF_6^-$) of the electrolyte we employ here was found to be located in the side-chain region [78], thus, emulating the environment of integer-charge transfer between P3HT and the TCNQ derivatives.

### 4.4.3 Drivers of IPA Formation—FTCNQ *versus* TCNQ

It is remarkable that FTCNQ at low $\chi$ has a much higher ability to ionize P3HT compared to TCNQ despite their $EA$s being only different by 0.1 eV. We already mentioned this observation in our previous study on the low doping regime [6] where we hypothesized the reason could lie in the significantly higher molecular dipole moment of FTCNQ—as the most obvious difference between the two dopants—which might drive disorder [216]. Through density functional theory (DFT) calculations, we found a molecular dipole moment $Q = 0.908$ D for FTCNQ, while it is negligible in F4TCNQ and TCNQ ($Q < 0.001$ D). However, by now adding F2TCNQ in our present study which bears an equally small $Q < 0.001$ D, we learn that the molecular dipole moment must rather be regarded as a negligible driver for the effect, based on the very similar $EA$ and $p_{CN}$ compared to FTCNQ. We further note that all the TCNQ derivatives employed feature only negligible differences in their molecular quadrupole moments, largely ruling out this factor as well. (See table C.2 for calculated molecular dipole and quadrupole moments.)

In the following, we discuss the nucleation effect for IPA formation, postulated by Wu et al. [184], as a potential way to explain the differences between the doping phenomenology of FTCNQ and TCNQ. When assigning a host HOMO-DOS width $\sigma$ to the nucleation threshold-concentration $\chi_{IPA} \approx 0.1\%$ of ionized dopants for each *total* dopant molar ratio $\chi$, we observe less broadening for higher $\chi$, suggesting a higher probability for the occurrence of the crystalline IPA phase, all while our experimental data shows increased CPX formation. This apparent discrepancy speaks, again, for an independent, competing CPX-formation mechanism. With this in mind, we turn our focus to the $\chi = 2\%$ cases as they yield the strongest contrast in IPA occurrence between FTCNQ and TCNQ, all while demanding the highest initial DOS broadening. While $\chi_{IPA} > 0.1\%$ is readily obtained for all F4TCNQ data points with the pristine-P3HT $\sigma = 0.06$ eV, the threshold would only be reached with $\sigma \geq 0.07$, 0.09, and 0.11 eV for F2TCNQ, FTCNQ, and TCNQ, respectively. Again, observing virtually the same, high ionization percentage $p_{CN}$ for F2TCNQ and FTCNQ while TCNQ only shows CPX formation, the nucleation effect does not seem to demand too different conditions in the three cases. It can therefore not be considered as the reason why IPA formation is possible with the $EA$ of FTCNQ but not with that of TCNQ, unless crystalline IPA-phase nucleation in P3HT substantially differs between the TCNQ derivatives.

Subsequently, we resort to the other reasoning which we had put forward in our previous study [6], considering a *self-amplifying effect* where only a small difference in initially ionized content with FTCNQ or F2TCNQ *versus* TCNQ would suffice to cross a threshold toward causing effective host HOMO-DOS broadening, thus, enabling more ionization and even further broadening. We note that this loop of broadening stops when further disorder is associated with a sufficiently high energetic cost such that CPX formation becomes more favorable than IPA formation following disorder.

### 4.4.4 Drivers of CPX Formation

Clearly, CPX formation cannot be handled as a mere fall-back mechanism when IPA formation is energetically not viable but requires drivers of its own that compete with IPA-favoring factors.

To begin with, the idea of preferential CPX formation in the amorphous phase of P3HT due to its effectively higher $IE$ detrimental to IPA formation [49] is supported by the lack of GIXRD features related to the crystalline CPX phase at lower $\chi$, while our spectroscopic data clearly show CPX indicators. Note that, beyond the higher $IE$ in amorphous phases, the intermolecular binding energies upon CPX formation are substantial and represent an appreciable driving force for the preferential formation of such complexes [38].

Regarding crystalline CPX phases, we again return to the computational study by Wu et al. [184] which showed that, while crystalline IPA and CPX phases yield similar changes in free energy, the IPA scenario profits from a nucleation threshold as low as 2-3 dopant radical anions among the simulated 1728 P3HT monomer units, i.e. $\chi_{\mathrm{IPA}} \approx 0.1\%$ to 0.2%. In turn, no CPX nucleation sites where seen even for the highest dopant loading they investigated, which was 144 CPX-forming dopants, i.e. $\chi_{\mathrm{CPX}} \approx 8\%$. (Wu et al. studied pure IPA and pure CPX systems, hence, $\chi$ in our mixed system is the convolution of $\chi_{\mathrm{IPA}}$, $\chi_{\mathrm{CPX}}$, and neutral dopant content.) Where the dopant $EA$ is sufficiently high for IPA formation, as it is the case for F4TCNQ, F2TCNQ, and FTCNQ, we can therefore speculate that a nucleation effect for the crystalline CPX phase does still occur at high ratios, because we observe a crystalline CPX portion for $\chi = 9\%$ and 17%. Alternatively, we can hypothesize that, in terms of enthalpy, a well-defined CPX polymorph only prevails over the IPA phase for a certain stoichiometry, e.g. $\chi = 14.2\%$ as reported by Jacobs et al. [39]; hence, we are to see the GIXRD CPX feature for the fluorinated FxTCNQs only at certain well-defined values instead of the gradual shift in the TCNQ case. For F2TCNQ, the loss of IPA related features in spectroscopy for 9% would then indicate this ratio to be close to such a stoichiometry, and any additional dopant loading to then form IPAs (or stay neutral) as we increase $\chi$ to 17%. For TCNQ, in contrast, its low $EA$ readily inhibits competition with IPA formation and, thus, makes CPX formation favorable even if no specific stoichiometry is met, which allows observing intermediate crystalline phases with changing $d$ values between pure P3HT and a fully mixed crystal.

Finally, we take a look at the potential response of conductivity to these different scenarios of CPX occurrence. In contrast to the absolute conductivity decrease we observe for our CPX-only system of P3HT-TCNQ, the conductivity was reported to increase significantly for other CPX-only systems such as quarterthiophene (4T)-F4TCNQ [34], which can probably be understood by the fact that conductivity is a convolution of carrier density and their mobility. For 4T-F4TCNQ, CPX crystallites (growing in co-crystal structure with 4T) were found embedded into an equally crystalline 4T matrix, which is potentially less detrimental to mobility as it is for the semi-crystalline P3HT system. Further, the broader peaks in x-ray diffraction for the P3HT case, their gradual shift with the TCNQ loading, and a loss of diffraction features at high $\chi$ (*cf.* figure 4.4(b)), all together indicate less order in the CPX phases themselves, in contrast to the 4T-F4TCNQ case. In further contrast, although CPX-rich, F2TCNQ thin film conductivity is still three orders of magnitude higher for 9% dopant loading than for pure P3HT; this could be ac-

counted to the CPX polymorph that is subject to a certain host-dopant stoichiometry, as we hypothesize.

## 4.5 Conclusion

To better understand conditions and mechanisms underlying IPA *versus* CPX formation in molecularly doped OSCs, we analyzed the doping of P3HT with F4TCNQ, F2TCNQ, FTCNQ, and TCNQ using optical and vibrational spectroscopy, x-ray diffraction, and conductivity data to serve as the basis for semi-classical modeling of the DOS. Our study shows that the ratio between IPA and CPX formation in P3HT yields higher IPA content by using TCNQ derivatives of higher degree of fluorination and for lower dopant concentrations. As a result from our combined analysis we can state that beyond a certain host-dopant stoichiometry, $\chi \geq 9\%$ for P3HT-FxTCNQ, crystalline CPX formation undergoing partial charge transfer can compete with integer charge transfer forming IPAs.

Juxtaposing the vast body of knowledge in literature to our own comprehensive data obtained from various experimental techniques all applied to the same systems in one study, we highlight challenges in providing consistent information on the occurrence of the different dopant scenarios, that is, CPX or IPA formation. Our data suggests that this is due to differences in oscillator strength between these scenarios and the respective spectral regions studied, as well as the fact that amorphous and crystalline phases are not equally probed by diffraction and spectroscopy. Especially FTIR stands out in that regard since the C≡N stretching modes of the TCNQ derivatives—commonly utilized to quantify the degree of charge transfer—appear to largely over-represent CPX formation, while the ring C=C stretching modes—mostly neglected in pertinent literature—provide conclusions that are more in line with the neutral and ionized dopant occurrence deduced from optical spectroscopy and diffraction data. Thereby, our work strongly supports a number of studies, recent and as far back as the 1980s, which highlight that interpretations of the C≡N stretching modes are complex as the origins of their shift can go far beyond the sole impact of charge transferred to the dopant.

We ultimately aimed to explore the energetics behind IPA formation in our experimental data as competing mechanism to CPX formation, starting with a comparison of host $IE$ with dopant $EA$ values as deduced from own CV results. We confirmed that the pure materials' $EA$ and $IE$ are no sufficient predictors for IPA formation alone, because it is well observed also for $EA < IE$. Going beyond our previous study assuming doping-induced broadening of a Gaussian DOS for the P3HT host material in the low doping regime [6] we applied semi-classical modeling that mimics the experimentally found trends of increased IPA content with lower dopant loading and higher dopant $EA$. Despite our caution in deducing the doping scenario *via* the C≡N stretching modes in FTIR, we could estimate the IPA content such that conclusive results for the DOS width emerged from our modeling. We found that for the $EA < IE$ cases of P3HT doped with F2TCNQ and FTCNQ, the host HOMO-DOS must broaden by about three to four times the width recently reported for pristine P3HT [64].

Still, our approach could not conclusively explain why TCNQ forms a CPX-only system with P3HT while FTCNQ can yield high percentages of ionization despite not having

a significantly stronger $EA$. On the one hand, we hypothesize that this is due to a self-amplifying effect where low initial ionization causes DOS broadening which supports further ionization. Its activation threshold would need to lie between the $EA$ values of TCNQ and FTCNQ, explaining their stark difference regarding IPA formation. Alternatively, the current lack of explicit CPX modeling in our approach neglects potential driving forces towards CPX formation that could suppress IPA formation for TCNQ, but less so for FTCNQ. To explicitly include CPX formation, the spatial arrangement of host and dopant as well as effects of the surrounding bulk must be included into the modeling, which requires information that cannot be deduced for intrinsically semi-crystalline P3HT and goes beyond the scope of our current study [69, 184, 216–218].

The direction of future work naturally emerges from our present data. While the crystalline IPA phase shows a variable lattice-spacing in the stacking direction which decreases with increased dopant loading, the crystalline CPX phase has an even smaller spacing that appears to be impossible to be gradually reached, but is fixed and independent of dopant concentration. Furthermore, that phase shows a significantly sharper peak than the corresponding IPA feature, which indicates higher order. Identifying host systems, polymeric and small molecular, where the mutual arrangement with the dopant can be precisely resolved for both scenarios of IPA and CPX formation is therefore part of our current dedication to this field.

# Chapter 5

# Approaching the Integer-Charge Transfer Regime in the Doping of Oligothiophenes

## 5.1 Introduction

The previous chapter investigated poly(3-hexylthiophene-2,5-diyl) (P3HT) p-doped with a series of 'FxTCNQs', i.e. 2,3,5,6-tetrafluoro-7,7,8,8-tetracyanoquinodimethane (F4TCNQ), 2,5-difluoro-7,7,8,8-tetracyanoquinodimethane (F2TCNQ), 2-fluoro-7,7,8,8-tetracyanoquinodimethane (FTCNQ), and 7,7,8,8-tetracyanoquinodimethane (TCNQ). It concluded that additional drivers behind the formation of ground-state charge-transfer complexes (CPXs) over integer charge transfer must exist besides simply the ionization energy $IE$ of the organic semiconductor host and the electron affinity $EA$ of the p-dopant being not favorable to ion-pair (IPA) formation. The host molecule conjugation length (*cf.* section 2.1) was suspected as a parameter that favors CPX formation below a certain limit, and investigated accordingly in one of our publications [4] by juxtaposing P3HT with oligomer equivalents of increasing length and their response to doping with F4TCNQ. This idea extends that put forward by Méndez et al. [34] who reported that the F4TCNQ-doped oligomer $\alpha$-quarterthiophene (4T) exclusively undergoes CPX formation while the polymer P3HT exhibits IPA formation when doped with, e.g., FTCNQ despite the $IE$-$EA$ relation being similarly favorable in both cases. This led to the consideration of an oligomer *versus* polymer regime where the conjugation length *per se* was decisive for CPX *versus* IPA formation, respectively. While that assessment was done according to $IE/EA$ data derived from ultraviolet/inverse photoelectron spectroscopy (UPS/IPES), Wegner et al. [48] found that energies derived from cyclic voltammetry (CV) are, in fact, more suitable for IPA prediction (see section 4.3.5). Since they published their finding around the time of our manuscript submission, their work was not considered in our publication [4] but will be in the present chapter. In addition, data that could not be acquired in a timely manner for publication, are analyzed in this chapter as well.

The present study employs a library of hexylated linear oligothiophenes labeled 'h$x$T' with $x$ = 4, 6, 8, 10 thiophene units of which all but the central two units comprise a hexyl

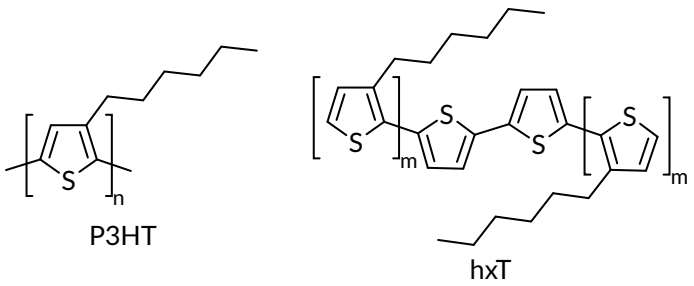


Figure 5.1: Skeletal structure of P3HT (left) in comparison to the hexylated oligothiophenes (right) discussed in this chapter. Compound shorthands follow the form 'h$x$T' with $x = 2 + 2m$, i.e. h4T, h6T, h8T, and h10T.

side-chain (see figure 5.1). Such an arrangement of thiophene rings with and without side chains came as a result of finding the ideal, commercially available starting material for h$x$T synthesis through decarboxylative cross-coupling. The latter was one of the main topics of our publication [4] and part of the first author's (Jiang Tian Liu) master's thesis [219] (see Contribution of Authors); consequently, for the sake of conciseness in this thesis, the present chapter is not manuscript-based like the previous one, but entirely rewritten providing a focus on the doping aspects of the study rather than on the synthesis of h$x$T.

In that regard, the use of oligomers with increasing conjugation length provides materials of decreasing $IE$ [143, 220] and can, therefore, be seen as a counter piece to the previous chapter where dopant $EA$ was increased with dopant fluorination. Further, the well-defined molecular length of oligomers in contrast to polymers can be seen as beneficial to reproducibility in device applications [65, 66, 68], where the materials are usually in their solid state. While the present h$x$Ts are viscously liquid at room temperature, they can be seen as a proof-of-concept for future solid-state derivatives. Moreover, this property mostly allows probing the local interaction between dopant and oligomer in the absence of driving forces brought about by the tendency of the latter to form a certain crystal structure—with the exception of h10T where partial precipitation is observed upon doping with F4TCNQ.

In this study, optical absorption spectroscopy in the ultraviolet to near-infrared range (UV-vis/NIR, section 5.3.1) is used, first, to confirm increasing conjugation length with oligomer length. Further, in tandem with FTIR (section 5.3.2), it allows to assess IPA and CPX populations upon doping with F4TCNQ and, in the special case of h10T, with F2TCNQ* as well. $IE$ values of the h$x$T compounds are derived from CV* (section 5.3.3) and put into perspective against conclusions drawn before [34] where UPS/IPES-based values [34, 47, 113, 148, 221] had been employed, instead. In this study, exclusive CPX formation is observed in all cases but for h10T-F4TCNQ, where additional IPA formation occurs and potential reasons for this threshold in oligomer length are discussed.

*These data were not included in the original publication [4].

## 5.2 Experimental Methods

3,3‴-dihexyl-2,2′:5′,2″:5″,2‴-quarterthiophene (h4T, also known as isoDH-4T [83]), 3,3‴,3⁗,4′-tetrahexyl-2,2′:5′,2″:5″,2‴:5‴,2⁗:5⁗,2⁗⁗-sexithiophene (h6T), 3,3⁗,3⁗⁗,3⁗⁗⁗,4′,4″-hexahexyl-2,2′:5′,2″:5″,2‴:5‴,2⁗:5⁗,2⁗⁗:5⁗⁗,2⁗⁗⁗:5⁗⁗⁗,2⁗⁗⁗⁗-octithiophene (h8T), and 3,3⁗⁗,3⁗⁗⁗,3⁗⁗⁗⁗,3⁗⁗⁗⁗⁗,4′,4″,4‴-octahexyl-2,2′:5′,2″:5″,2‴:5‴,2⁗:5⁗,2⁗⁗:5⁗⁗,2⁗⁗⁗:5⁗⁗⁗,2⁗⁗⁗⁗:5⁗⁗⁗⁗,2⁗⁗⁗⁗⁗:5⁗⁗⁗⁗⁗,2⁗⁗⁗⁗⁗⁗:5⁗⁗⁗⁗⁗⁗,2⁗⁗⁗⁗⁗⁗⁗-decithiophene (h10T) were synthesized through decarboxylative cross-coupling reaction (as the key transformation), characterized through $^{1}$H and $^{13}$C nuclear magnetic resonance spectroscopy (NMR), and provided by Jiang Tian Liu; for details see [4] and [219].

All samples were prepared and, if not specified otherwise, measured under inert $N_2$ atmosphere in a glovebox ($H_2O$ <2 ppm, $O_2$ <6 ppm). All samples involving P3HT are the same as in chapter 4 and details are given in section 4.2. Anhydrous chloroform (Sigma-Aldrich, amylenes as stabilizer, purity ≥99%) was used as the common solvent. F4TCNQ and F2TCNQ were used as purchased from Tokyo Chemical Industry Co., Ltd. (TCI; purity >98.0%). F4TCNQ was dissolved at a concentration of 3.6 mM by stirring and heating at 60°C for >24 and <48 h. F2TCNQ was dissolved at a concentration of 1.2 mM through stirring on a heater at 60°C for 1 h and left to cool at room temperature for at least 1 h before further use. The change in protocol is a result of higher reliability found with the latter during the measurements performed for the study discussed in chapter 4 which, due to the time needed to produce further amounts of h10T, occurred between the F4TCNQ and F2TCNQ doping series with h$x$T. Each oligothiophene species was dissolved at a concentration of 3 g/l (20.0, 20.6, 21.7, 24.1 mM for h10T, h8T, h6T, h4T, respectively) directly prior to use; doped solutions were also mixed directly prior to use. To facilitate structural comparison between doped systems with differently large oligothiophenes, dopant molar ratios $\chi$ relate to the number of thiophene rings $x$ per dopant molecule rather than entire molecules, i.e. $\chi = (1 + x)^{-1}$, e.g. $\chi$ = 9% means a ratio of one dopant per 10 P3HT repeat units (see also section 4.2), 1 h10T, 10/8 = 1.2 h8T, 10/6 = 1.7 h6T, or 10/4 = 2.5 h4T molecules.

20 µl of the respective solution were drop-cast[†] onto 1 cm×1 cm quartz and Si (undoped, native oxide layer) for UV-vis/NIR and FTIR, respectively. No more than 10 min passed between deposition and measurement. UV-vis/NIR absorbance spectra were recorded on an Agilent Technologies Cary 5000 Spectrophotometer while keeping the samples under inert $N_2$ atmosphere in custom-built sealed boxes with quartz windows (see figure 3.2 top). Likewise, FTIR absorbance spectra were recorded on a Thermo Scientific Nicolet 6700 using a liquid-nitrogen cooled mercury cadmium telluride detector with the samples under inert $N_2$ atmosphere in sealed, equally custom-made boxes with KBr windows.

CV measurements follow the same protocol as outlined in section 4.2.5 with the difference of using a Pt-disk instead of a glassy carbon working electrode (as a result of availability). Further, dichloromethane was used instead of acetonitrile for better solubility in the solution CV setup where half-wave potentials between corresponding anodic

[†]No film at all could be produced through spin-coating.

and cathodic peak potentials were used to represent the $IE$ values of h10T, h8T, h6T, and h4T. CV was done additionally with a drop-cast h10T film on indium tin oxide (ITO) as the working electrode using an electrolyte solution of 0.1 M tetrabutylammonium hexafluorophosphate in acetonitrile and a scan rate of $0.1\,\mathrm{V\,s^{-1}}$. In alignment with the P3HT film analyzed in the previous chapter, the half-wave potential was not determined for the h10T film and the oxidation onset in the anodic sweep was taken to represent its $IE$. In further accordance with the previous chapter, all redox potentials $V_{\mathrm{redox}}$ were measured against ferrocene/ferrocenium ($Fc/Fc^{+}$) internal standard which, again, was estimated as the commonly used $-5.1\,\mathrm{V}$ *versus* vacuum energy [75]. Likewise, $EA$ and $IE$ values are again given as positive numbers for the sake of clarity by associating higher $EA$ with higher dopant strength.

Due to limited h$x$T compound availability, no measurements could be repeated.

## 5.3 Results and Discussion

### 5.3.1 Optical Absorption Spectroscopy

The top part of figure 5.2 shows the optical absorption spectra of pristine h4T, h6T, h8T, h10T, and P3HT films. The energies of the fundamental transition—from the highest occupied molecular orbital in the ground state (HOMO) to the lowest unoccupied molecular orbital in the ground state (LUMO)—decrease with increasing chain length [65, 82–85] as identified by the low-energy absorption onsets. The latter values are plotted in the top right of figure 5.2, exhibiting a $1/x$ dependency of the optical gap with the number $x$ of thiophene repeat units; a linear regression converges on 1.89 eV for $x \to \infty$ which fits the P3HT absorption onset within the error margin. This $1/x$ dependency indicates that there are no significant differences in planarity between the h$x$Ts [85], i.e. a break in conjugation through chain-segment torsion or chemical defects (*cf.* section 2.1) is equally (un)likely in all h$x$Ts. In other words, the conjugation length increases linearly with the oligomer backbone length.

In addition to their different positions, the main absorption peaks in the pristine h$x$T spectra appear free of subfeatures, in contrast to that of pristine P3HT. The latter shows hints of the vibronic substructure known to be more prominent the more a P3HT film consists of crystalline phases [222–224]. The smoothness of the h$x$T spectra is therefore likely a result of the aforementioned viscously liquid consistency of these compounds at room temperature, producing a fully amorphous film.

At the bottom of figure 5.2 UV-vis/NIR merged with FTIR spectra of F4TCNQ- and F2TCNQ-doped h$x$T films are compared with their P3HT counterparts at a dopant molar ratio $\chi = 9\%$ *versus* thiophene-ring unit (see section 5.2). The F4TCNQ-doped h4T spectrum is very similar to previously reported spectra of non-alkylated 4T doped with F4TCNQ [34], showing a prominent peak at 0.89 eV in the fundamental gap of the pristine material which can be assigned to the transition from the HOMO to the LUMO of the CPX (*cf.* figure 2.7) that is formed between the oligothiophene and F4TCNQ; the vibronic progression of this transition is known to result in the shoulder observed around 1.10 eV [34]. The according doped h6T and h8T spectra are, in turn, similar to h4T but

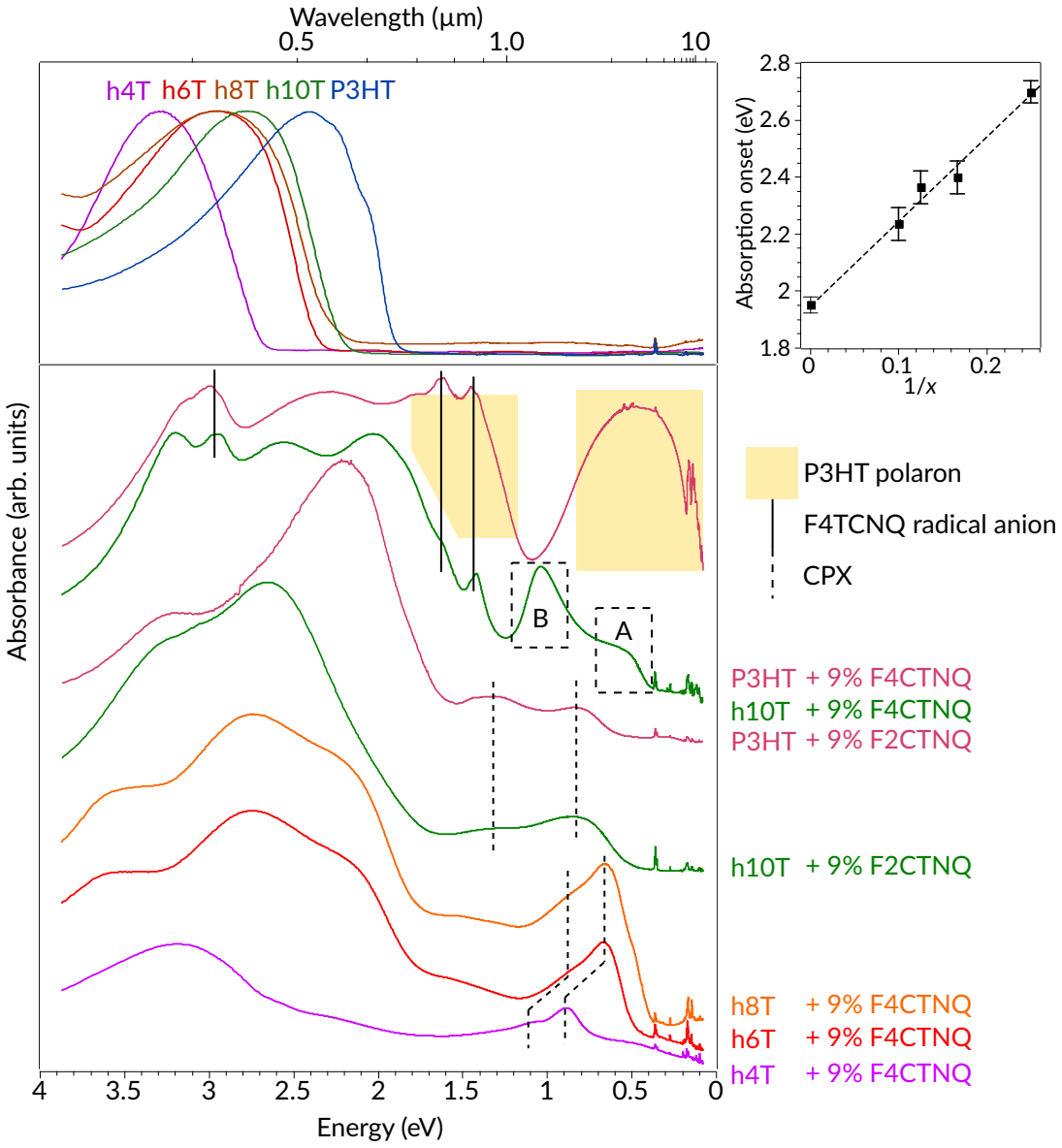


Figure 5.2: Top: UV-vis/NIR data merged with FTIR thin-film spectra of pure h4T, h6T, h8T, h10T, and P3HT together with a plot of extrapolated transition onset *versus* $1/x$ with $x$ being the number of thiophene repeat units. Bottom: Thin-film spectra upon doping with F2TCNQ (only h10T and P3HT) and F4TCNQ at a dopant molar ratio $\chi = 9\%$ *versus* thiophene-ring unit; peaks 'A' and 'B' are discussed in this chapter as the indicators of charged h10T and the h10T-F4TCNQ CPX, respectively; additional UV-vis/NIR data of h4T, h6T, h8T, h10T at 2%, 5%, 9%, and 17% F4TCNQ doping can be found in figure C.2. Note that the FTIR data below 0.5 eV should only be regarded as a qualitative addition to the UV-vis/NIR data due to the differences between the two experiments that are explained in section 3.2.3.
Figure modified from [4] J. T. Liu, H. Hase, S. Taylor, I. Salzmann, and P. Forgione, "Approaching the Integer-Charge Transfer Regime in Molecularly Doped Oligothiophenes by Efficient Decarboxylative Cross-Coupling," *Angewandte Chemie International Edition*, vol. 59, no. 18, pp. 7146–7153, Apr. 2020. Copyright 2020 John Wiley and Sons.

Figure 5.2: (continued) Permission granted through contributor rights retained at publication. Modifications to be noted in this version: Labeling and coloring were changed to conform with this thesis. Compounds previously labeled '4b', '8', '9', '10', and 'F4' correspond here to h4T, h6T, h8T, h10T, and F4TCNQ, respectively; dopant molar ratios $\chi$ *versus* thiophene-ring unit are now provided. The 'Energy' range is now extended below 0.5 eV through the merging with FTIR spectra; for completeness of the latter and better data comparison within this thesis, spectra of P3HT, pristine and doped with 9% F4TCNQ, are now the same as in chapter 4, instead of [2]. Spectra of F2TCNQ-doped h10T and P3HT are now added. The previously inset graph of 'Onset' (here, 'Absorption onset') against $1/x$ is now re-plotted with error bars.

with the same peak centered at 0.66 eV. Assigning this peak to the CPX HOMO-LUMO transition is in line with the bathochromic shift expected for longer conjugation length as recently calculated in a theoretical study on the level of density functional theory (DFT), where the electronic structure of CPXs formed by 4T, $\alpha$-sexithiophene, $\alpha$-octithiophene, and $\alpha$-decithiophene (10T) with F4TCNQ has been investigated [143]. This shift can also be understood using the Hückel-like approach introduced in section 2.3.3, equation 2.2, from which the gap $E_{\mathrm{gap}}$ between the energy levels of the CPX HOMO $E_{\mathrm{CPX,H}}$ and LUMO $E_{\mathrm{CPX,L}}$ can be estimated as:

$$E_{\mathrm{gap}} = E_{\mathrm{CPX,H}} - E_{\mathrm{CPX,L}} = 2\sqrt{(IE - EA)^2 + 4\beta^2} \tag{5.1}$$

from the host $IE$, the p-dopant $EA$, and the resonance integral $\beta$ [33, 50]. The fact that both h6T and h8T CPXs yield the same transition energy despite the lower $IE$ of h8T, on the one hand, could stem from differences in the exciton binding energy that needs to be subtracted from $E_{\mathrm{gap}}$ for the energy of the optical transition. On the other hand, assuming virtually equal exciton binding energies for both the h6T and h8T CPXs, a decreased $\beta$ value might compensate the lower $IE$ of h8T, meaning that the nodal structure of host HOMO and dopant LUMO match up less for h8T+F4TCNQ than for h6T+F4TCNQ (*cf.* section 2.3.3). As $\beta = 0$ would mean that the CPX provides the same HOMO and LUMO energy levels as the pristine host and p-dopant, respectively, a lower $\beta$ value for h8T+F4TCNQ means that its CPX formation is less energetically favorable over IPA formation than in the case of h6T+F4TCNQ—regardless of the fact that h8T already is more likely to be ionized due to its lower $IE$. The viscously liquid consistency means that nodal-structure matching is not mediated by constraints of crystalline packing but most likely a result of the different oligomer lengths. Therefore, shorter oligothiophenes might favor CPX formation due to better for node matching between the host HOMO and dopant LUMO.

The present F4TCNQ-doped h10T spectrum shows a more complex arrangement of features. As with P3HT (see also section 4.3.1), $F4TCNQ^{\bullet-}$ with h10T is identified by sharp peaks at 1.45 and 1.63 eV (solid vertical lines in figure 5.2) [50, 124, 225, 226]. Since for P3HT these are accompanied by broad polaron bands [34, 126], charged h10T features are expected, here. As potential contenders, the present spectrum displays a weak peak at 0.6 eV (labeled 'A') and a more prominent feature at 1.04 eV (labeled 'B').

Peak A seems to represent h10T$^{\bullet+}$ according to literature while peak B appears at lower energy than expected for this assignment: a theoretical study on the optical properties of charged oligothiophenes including 10T reported the two lowest energy transitions of its radical cation 10T$^{\bullet+}$ to be around 0.6 and 1.3 eV [125]; an experimental study on tridodecyl nonithiophene and tetradodecyl duodecithiophene reported radical-cation transitions (in solution at room temperature) at 0.67/1.46 eV and 0.59/1.42 eV, respectively [84]. The latter study, however, also recorded spectra at reduced temperature with the two of peaks at 0.94/1.94 eV instead, which they attribute to dimerization of the tetradodecyl duodecithiophene radical cation; since another absorption peak is indeed observed around 2 eV, we hypothesized in the original publication [4] that peak B is indicative of h10T$^{\bullet+}$ packed in the solid film that appears to exist under a layer of the otherwise viscous liquid material. In that scenario, peak A was seen as a further bathochromic shift from the observed CPX HOMO-LUMO transition of h8T; in support of this assignment, the absence of peak A at lower $\chi$ values (see figure C.2) could fit into an analogy with P3HT where CPXs with F4TCNQ are found only at high dopant loading, as seen in the previous chapter.

In contrast to F4TCNQ, F2TCNQ-doped h10T exhibits no features that can be associated with IPA formation but, instead, two peaks in NIR that match the positions of the CPX transitions in F2TCNQ-doped P3HT at 0.82 and 1.31 eV, even exhibiting similar peak widths. This indicates that CPX formation on P3HT appears to be a phenomenon localized to about 10 thiophene units, and supports h10T as a valid oligomer analogue to P3HT. This finding adds another point in the interpretation of the F4TCNQ-doped h10T spectrum, as follows. If the according peaks for the h10T-F4TCNQ CPX, in analogy, were to be located at the positions for the P3HT-F4TCNQ CPX at 0.66/1.15 eV [39] and, again, exhibit a similar width, the sharper peak B might mask the 1.15 eV CPX peak while peak A, here observed at 0.5 eV, might simply be the visible flank of a CPX peak centered at 0.66 eV. As the latter is also the value observed here for the F4TCNQ CPX-transition with h6T and h8T, this would support the aforementioned idea that the nodal-structure matching between host HOMO and dopant LUMO becomes less favorable for CPX formation for longer oligothiophene chains.

Finally, in a related study [8] that I contributed to (see List of Associated Works for details), the fact that h10T+F2TCNQ only yields CPX formation was utilized in comparison with the novel dopant PFP3CN3-CP based on a cyclopropane core that exhibits virtually the same *EA* as F2TCNQ but was designed to sterically inhibit CPX formation through shielding its electron-rich core by three perfluorophenyl side groups. This CPX-inhibiting approach was deemed successful, as this dopant produced no new transitions in the fundamental gap of h10T, in contrast to the peaks of the CPX with F2TCNQ. As already mentioned in the Foreword of chapter 4, CPX-inhibition was seen as the reason why doping P3HT with PFP3CN3-CP produced generally higher conductivity than with F2TCNQ despite the same *EA* values.

### 5.3.2 Vibrational Absorption Spectroscopy

As laid out in sections 4.3.2 and 4.4.1, the peak positions of the C≡N stretching modes of TCNQ derivatives are sensitive to the degree of charge transfer [51–53] and can therefore

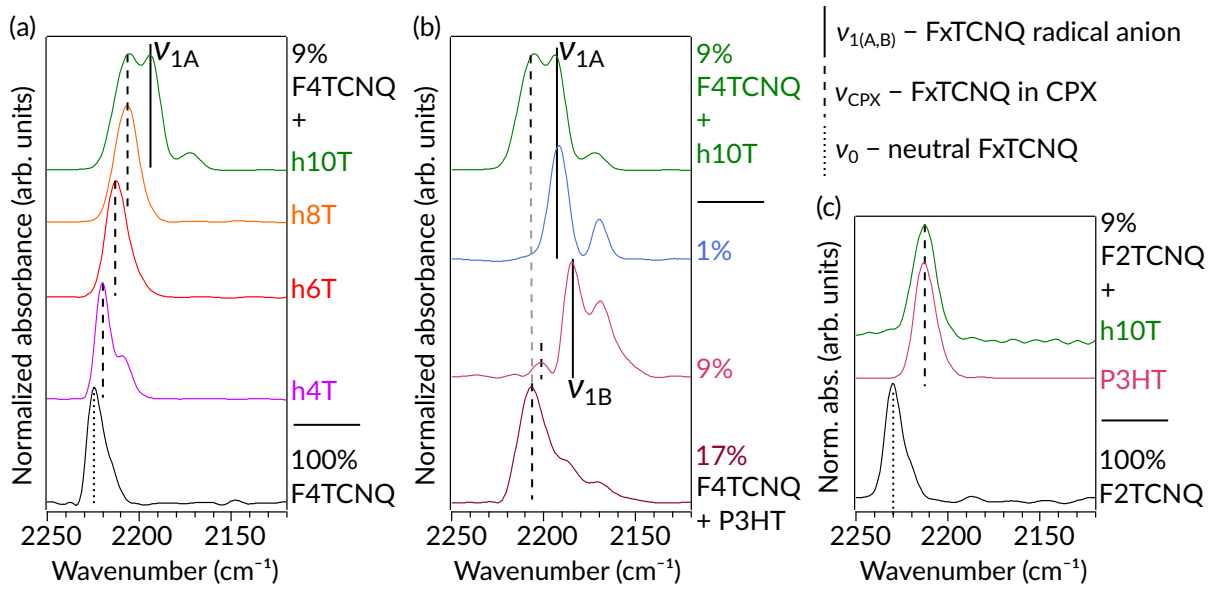


Figure 5.3: FTIR data in the region of the C≡N vibrations of h4T, h6T, h8T, h10T, and P3HT films doped with F2TCNQ and F4TCNQ. (a) Comparison of F4TCNQ-doping at a dopant molar ratio $\chi$ = 9% *versus* thiophene-ring unit in h4T, h6T, h8T, and h10T. (b) Comparison of F4TCNQ-doping with $\chi$ = 9% in h10T *versus* 1%, 9%, and 17% in P3HT. (c) Comparison of 9% F2TCNQ-doping in h10T

be utilized to support peak assignments in the optical absorption spectra to IPA or CPX as long as potential effects from the general electric field of counter charges [54, 58] are given consideration.

Firstly, the main C≡N-mode peak of F4TCNQ undergoes a softening of 6 cm$^{-1}$ (see figure 5.3(a)) from the neutral position (2226 cm$^{-1}$; dotted vertical line in figure 5.3(a))) when doping h4T, and is identical to the peak shift reported for 4T [34]. This shift increases for h6T and then h8T which is commonly interpreted as an increase in degree of charge transfer [51–53] and is expected as a result of $IE$ decreasing with conjugation length [143, 220].

Secondly, F4TCNQ-doped h10T again stands out, here, by exhibiting equally strong peaks at both 2206 cm$^{-1}$ (dashed vertical line in figure 5.3(a),(b)) and 2194 cm$^{-1}$ ($\nu_{1A}$ in figures 5.3(a),(b)). The former is at the same position as for h8T and in between the CPX-related peaks obtained for 9 and 17% F4TCNQ with P3HT; it can therefore be safely assigned to CPX formation (dashed vertical lines in figures 5.3(a),(b)). As discussed in section 4.4.1, $\nu_{1A}$ is at a position known for F4TCNQ$^{\bullet-}$ as found for 1%-doped P3HT—an indicator for IPA formation. In the original publication [4] we interpreted this peak as identifying F4TCNQ$^{\bullet-}$ stacked with the polymer backbone as we assigned in a prior study [2]. However, as section 4.4.1 discusses, it is rather more likely indicative of a more localized hole than in the case of, e.g., 9% F4TCNQ in P3HT which exhibits the peak position $\nu_{1B}$ = 2185 cm$^{-1}$, instead.

Finally, the F2TCNQ C≡N-mode peak with h10T (see figure 5.3(c)) falls completely in line with the optical absorption spectra by exhibiting a sole CPX-related peak at

2215 $cm^{-1}$ as found for 9% F2TCNQ in P3HT, the dopant-per-thiophene-unit equivalent in the polymer. Again, this underlines the localized nature of CPX formation.

### 5.3.3 Energy Levels from Cyclic Voltammetry (CV)

An *IE* ($V_{redox}$ *versus* $Fc/Fc^+$) of 5.39 (0.29), 5.39 (0.29), 5.45 (0.35), and 5.53 eV (0.43 V) can be derived from cyclic voltammograms (see figure C.9) for h10T, h8T, h6T, and h4T, respectively, dissolved in dichloromethane. Bringing to mind again the error margin expected for energy levels derived from CV (±0.1V) [75], the value for h4T is in good agreement with a previous report on the same compound (there, labeled 'isoDH-4T') [83]; $V_{redox}$ *versus* $Fc/Fc^+$ for h6T agrees well with the value of the closely related 3,3‴″-hexyl-2,2′:5′,2″:5″,2‴:5‴,2⁗:5⁗,2⁗′:5⁗′,2⁗′′-sexithiophene (labeled 'isoDH-6T'; 4 instead of the 2 non-hexylated thiophene units at the center of h6T) reported in the same study [83]. The *IE* reduction with increasing oligomer length towards h8T and h10T is expected from DFT calculations on linear oligothiophenes, in general [143, 220].

CV was also conducted on h10T drop-cast onto an ITO-coated glass-slide for analysis of the IPA formation found with this oligomer in comparison with P3HT whose voltammogram was measured in the same manner (see section 4.3.5). The *IE* ($V_{redox}$ *versus* $Fc/Fc^+$) of 5.42 eV (0.32 V) is in agreement with the value extracted from CV data of h10T in solution, above. At a first glance, the similarity of both values seems to undermine the argument in sections 4.3.5 and 4.4.2 that CV on a film provides an *IE* value sensitive to solid-state effects like the up to 0.5 eV effective *EA* increase (or, conversely, *IE* decrease) for radical anion intercalation in alkyl side-chains [69]. However, as already mentioned above, the h*x*Ts are viscously liquid at room temperature except in the case of F4TCNQ-doped h10T. It is therefore conceivable, that aggregation occurs with F4TCNQ but not $PF_6^-$ of the CV electrolyte, hence, CV only probes the material in its viscously liquid form, potentially very similar to the dissolved state.

It is remarkable that h8T and h10T have virtually the same *IE* but only h10T forms IPAs with F4TCNQ. Further, both in the case of h4T+F4TCNQ and P3HT+FTCNQ, the dopant *EA* is about 0.2 eV lower than the host *IE* but only the latter undergoes IPA formation. This fits the comparison that was mentioned in the introduction of this chapter, between 4T+F4TCNQ and P3HT+FTCNQ according to data by Méndez et al. [34] where only the latter system undergoes IPA formation despite it having an equal (or even less favorable) *IE*-*EA* relation; note that their comparison was done employing UPS/IPES-derived data but still holds using CV-derived values as well (see appendix B). This points to a CPX-dominated oligomer regime and an IPA-facilitating polymer regime at whose threshold indeed lies h10T. The aforementioned decrease in nodal-structure matching as a CPX-favoring parameter could be a potential reason for this finding.

Another idea comes from the fact that a dark film was observed to precipitate from the viscously liquid h10T upon doping with F4TCNQ. In this film, h10T could form hexyl side-chain regions similar to those in P3HT where $F4TCNQ^{\bullet-}$ is known to reside [2, 36, 56, 58, 138–142] (*cf.* section 4.3.3). This region effectively increases the dopant *EA* and, therefore, makes the system more favorable to IPA formation [69] (*cf.* section 4.4.2). It is conceivable that h10T offers long enough uninterrupted chains of hexylated thiophene units (4 units to either side) to form side-chain regions sufficiently large to harbor a F4TCNQ radical anion.

## 5.4 Conclusion

The presented data shows that a critical length in h$x$T thiophene oligomers towards IPA-formation upon doping with F4TCNQ, is reached with $x = 10$ thiophene units—a finding anticipated from prior work on the comparison of doping with TCNQ derivatives in the oligomer 4T and P3HT as its polymer equivalent [34]. CV-derived energy levels demonstrate that $IE$ values decreasing due to longer conjugation lengths cannot be seen as the sole reason for this observation. That is because IPA formation occurred for some cases with P3HT and h10T where comparable $IE$-$EA$ conditions with the shorter h$x$Ts only yielded CPX formation.

On the one hand, the length of the uninterrupted chain of hexylated thiophene units might play a role here as the formation of alkyl side-chain regions can offer an electrostatic harbor for $F4TCNQ^{\bullet-}$ that effectively reduces the energetic barrier to ionization [69]. A driver for CPX formation therefore lies with the electrostatic environment that a host material presents to a dopant. This could be verified using oligothiophenes that comprise four consecutive hexylated thiophene units, as h10T does, but a varied number of non-hexylated ones.

On the other hand, the present data pointed to a reduction of the resonance integral $\beta$, as a result of reduced nodal-structure matching between host HOMO and dopant LUMO for longer oligothiophenes, thus, making CPX formation energetically less competitive against IPA formation. To use equation 5.1 to quantify and confirm the change in $\beta$, the optical gap, as determined here, cannot be used unless the exciton binding energy in the CPX is known. However, as done before by Méndez et al. [34] on 4T+F4TCNQ, future efforts could determine the $IE$ and $EA$ of the CPX through UPS and IPES, respectively, to obtain the according energy gap and, subsequently, the $\beta$ values.

In general, a next step in the study of oligothiophenes could be the synthesis of soluble, yet solid-state derivatives of h$x$T to investigate structural aspects through diffraction techniques as well as the thin-film conductivity to assess their applicability in electronics.

# Chapter 6

# Conclusion

Organic semiconductors (OSCs) are an up-and-coming class of materials opening up new avenues for applications such as opto-electronics, thermal energy harvesting, or flexible, wearable electronics. However, in contrast to their inorganic counterparts, efficient doping of OSCs as a fundamental method to control charge-carrier density and species (electrons and holes) is still facing major hurdles. This work focused on the particular issue of gaining control over the circumstances under which fractional charge transfer between host and dopant through formation of a ground-state charge-transfer complex (CPX) can occur in molecularly doped OSCs. In contrast to integer charge transfer through ion-pair (IPA) formation, CPX formation is generally detrimental to doping efficiency. To study the driving forces and underlying mechanisms in situations where IPA formation competes with CPX formation, the central system investigated in this thesis was the prototypical conjugated polymer poly(3-hexylthiophene-2,5-diyl) (P3HT) p-doped with the strong molecular acceptor 2,3,5,6-tetrafluoro-7,7,8,8-tetracyanoquinodimethane (F4TCNQ), where both processes are observed simultaneously, with a ratio depending on deposition conditions, polymer parameters, and dopant loading.

Summarizing the work in this thesis, first of all, chapter 4 investigated the doping of P3HT with a series of 'FxTCNQs', i.e. F4TCNQ, F2TCNQ, FTCNQ, and TCNQ, as they exhibit, in that order, decreasing electron affinity $EA$ values. Importantly, they cross the ionization energy $IE$ value of P3HT when going from F4TCNQ to F2TCNQ. This way, the dependency of CPX and IPA occurrence on the $IE$-$EA$ energy difference could be probed. Given that the molecular structure and, therefore, spatial demand in a doped OSC is essentially identical throughout the FxTCNQ series, $IE$-$EA$ can be regarded as an isolated parameter in this study. It was confirmed that not only $IE$ and $EA$ impact the formation of CPXs but also the doping concentration, as CPXs were only found for P3HT-F4TCNQ above 9% dopant molar ratio. Therefore, all dopants were employed in a series of concentrations between 1% and 17%, here, probing the influence of dopant loading. Adding that all systems were studied through a comprehensive array of techniques assessing their opto-electronic properties and structure, an unprecedented unifying database on P3HT-FxTCNQ systems was created. It features optical absorption spectroscopy in the ultraviolet, visible light, and the near-infrared, Fourier-transform infrared spectroscopy (FTIR), cyclic voltammetry, conductivity, and grazing-incidence x-ray diffraction (GIXRD) data, providing complementary information on both energetic

and structural properties. This was supplemented by modeling of the occupation of the Gaussian-shaped density of states (DOS) in mixed host-dopant systems for the highest occupied molecular orbital in the ground state (HOMO) of P3HT, acknowledging that $IE$ and $EA$ values are typically derived from measurements on pristine materials which might not reflect the energetic situation upon mixing compounds. This is based on the notion that the presence of dopant molecules in the host matrix can disrupt its structural and, consequently, energetic order, leading to a broader energy distribution of HOMO levels of the host, reaching further towards the energy levels of the lowest unoccupied molecular orbital in the ground state (LUMO) of the dopants, thus enabling charge transfer with dopants of smaller $EA$. The IPA content according to different HOMO-DOS widths was calculated and compared to estimations deduced from experimental FTIR data.

Secondly, in a similar series of experiments presented in chapter 5, P3HT was exchanged with hexylated oligomer-equivalents h$x$T of $x$ = 4, 6, 8, and 10 thiophene repeat units (full names in section 5.2, structure in figure 5.1) to probe the conjugation length as a parameter for IPA *versus* CPX formation. In particular, the minimum conjugation length in linear oligothiophenes was thereby probed as a factor to promote IPA over CPX formation. As h4T, h6T, and h8T already exhibited only CPXs upon using F4TCNQ, weaker dopants of the FxTCNQ series were not employed in the light of limited h$x$T availability, which was provided in an internal collaboration with the group of Dr. Forgione (Department of Chemistry and Biochemistry). Similarly, while h10T indeed showed IPAs (along CPXs) for F4TCNQ, exclusive CPX formation was already observed for the next-weaker dopant, F2TCNQ, hence, FTCNQ and TCNQ were not employed, here.

Four distinct conclusions were drawn from the overall body of the present work. Firstly, the broad, coherent dataset created on P3HT-FxTCNQ in chapter 4 allowed to question and evaluate common experimental identifiers of IPA *versus* CPX formation, in particular, the positions of C≡N stretching modes, often used to determine the degree of charge transfer with FxTCNQs. However, the specificity of that determination is commonly overestimated in literature since these modes are generally highly sensitive to the surroundings of the dopant. Therefore, additional factors leading to their shift recently became the subject of several investigations whose findings were evaluated for their applicability, here. Further, the present work adds that the magnitude of peaks at CPX-assigned C≡N-mode positions appear to over-represent the amount of dopants in a CPX, that is, in comparison to the situation when analyzing the similarly shifting ring C=C-mode peaks. Hence, a central conclusion of chapter 4 is that small amounts of neutral or ionized dopant content might go undetected in a study when solely relying on C≡N-mode positions. On the one hand, finding that dopant content according to the C=C modes is more in line with optical absorption and GIXRD data, adds support to previous endorsements of using the C=C modes instead of the C≡N modes. On the other hand, the issue remains that the C≡N modes are experimentally more accessible since the C=C modes are readily masked by those of the host molecule, as common in conjugated organic molecules. Further, as the discrepancy between the two modes is not a matter of different methods but plays out within one-and-the-same record of a vibrational spectrum, it highlights that data from other techniques should be compared to gauge the validity limits of any conclusions. Sole reliance on another method should also

be avoided as the ambiguous feature overlap in the present optical absorption spectra demonstrated; other methods entail their own issues, e.g., the FxTCNQ N 1s core-level peak-positions in x-ray photoelectron spectroscopy are not definitely determined [55]. Therefore, limitations to the validity of the data must be assessed in the context of the desired analysis as, e.g., done here by regarding the C≡N mode-derived IPA content as a *lower* limit in the light of analyzing a concomitantly *increasing* HOMO-DOS width.

Secondly, having data reliability established, both the doping of P3HT (chapter 4) and h10T (chapter 5) demonstrated that IPA formation appears favorable in the system even for cases where the $EA$ of the dopant is lower than the $IE$ of the host. In comparison to known experimental values of the Gaussian HOMO-DOS width in pristine P3HT, the presented calculated data showed that a significant broadening must occur to explain the amounts of ionized F2TCNQ and FTCNQ as deduced from spectroscopic data. This is contrasted by TCNQ-doping where no evidence for ionization was seen whatsoever, and the HOMO-DOS width producing such a result would be only as wide as or even narrower than in the pristine case—a peculiar situation since the $EA$ of TCNQ is only slightly weaker than that of FTCNQ. On the one hand, a self-amplifying effect is proposed, where an initial number of ionized dopants leads to DOS broadening which, in turn, leads to more dopants being ionized. The activation threshold to produce a sufficient amount of initially ionized dopants to cause effective DOS broadening would need to lie between the $EA$ values of TCNQ and FTCNQ. On the other hand, it needs to be acknowledged that CPX formation is not implicitly modeled into the DOS, here, and thus omitted factors promoting CPXs might be stronger in TCNQ than FTCNQ. However, modeling CPX formation demands including details of the spatial arrangement between host and dopant along with effects of the surrounding bulk which, however, requires either information that cannot be deduced for intrinsically semi-crystalline P3HT or approaches that go beyond the scope of the present work, e.g., all-atom molecular dynamics simulations [184] or close combinations of modern morphology modeling with density functional theory [227]. These, however, are also still lacking examples where the system is not parametrically preset to go into either IPA or CPX formation, instead of a model evolving to form either one or both.

Therefore, dealing with a driver of CPX formation, the third conclusion turns back to the analysis of experimental data. The present experiments clearly showed that low dopant concentrations do promote IPA formation. In particular, the GIXRD data in chapter 4 enabled putting forward the hypothesis that CPX formation becomes more potent in rivaling IPA formation when a certain host-dopant stoichiometry for the creation of a distinct CPX polymorph is reached. Knowledge about such a driver behind CPX formation would be of importance to control doping phenomena since, e.g., steric hindrance was shown to inhibit CPX formation but comes at the cost of reduced dopant $EA$ [8], hence, disabling IPA formation for some high-$IE$ hosts, in the first place. Instead, thin-film deposition and, generally, crystallization strategies could then be devised based on the prevention of the proposed CPX polymorph. However, to transform this hypothesis into a valid theory, future studies are needed that (re-)evaluate diffraction data in the light of this proposal on more systems where both IPA and CPX occurrence might be observable. A system posing as an exciting first contender could be poly(2,5-bis(3-tetradecylthiophen-2-yl)thieno[3,2-b]thiophene) (known as PBTTT) in place of P3HT due to similar $IE$ [228] but a significantly different repeat unit.

Finally, studying P3HT oligomer-equivalents in chapter 5, it was found that the threshold from the CPX into the IPA regime upon F4TCNQ-doping lies around 10 thiophene repeat units. While longer conjugation lengths entail lower $IE$ values which make IPA formation generally energetically more favorable, other factors must be at play as is demonstrated, e.g., by the fact that the difference between host $IE$ and dopant $EA$ is virtually the same in F4TCNQ-doped h4T and F2TCNQ-doped P3HT but only the latter system exhibits IPA formation. Two potential reasons for this behavior were identified. Firstly, the resonance integral $\beta$ appears to be reduced for longer h$x$Ts, potentially, as a result of less nodal-structure matching—on which $\beta$ depends—between host HOMO and dopant LUMO in the CPX. Thus, a reduction in $\beta$ makes CPX formation even less energetically competitive against IPA formation with increasing conjugation length than the lower $IE$ values already do. To validate this finding, the $IE$ and $EA$ of the CPX could be obtained in future work through ultraviolet photoelectron spectroscopy and inverse photoelectron spectroscopy, respectively, to calculate and, therefore, quantify and confirm the change in $\beta$—an approach used in the past to calculate $\beta$ for F4TCNQ-doped $\alpha$-quarterthiophene [34]. Secondly, the extent of the *contiguous* hexyl chain region, as a marked difference between P3HT and the employed oligomers, appears to be of importance and has so far not been addressed in literature. As the applied h10T consists of 4 hexylated thiophene rings to either side of 2 non-hexylated units in the center, future studies should characterize the doping response of linear oligothiophenes with 4 consecutive, hexylated units but different overall conjugation length. This strategy could enable to ultimately single out the influences of conjugation length and hexylation. Defining such strategies would benefit the goal to create IPA-forming, discrete oligothiophenes to achieve highly reproducible device performance [65, 66, 68] due to their well-defined molecular length, in contrast to batch-to-batch differences and the mixture of various sizes commonly found with polythiophenes. This, in turn, could be beneficial to reduce transport losses in organic hole-transport layers in perovskite solar cells [29].

In summary, this work demonstrated the complexity of energetic—hand-in-hand with structural—influences behind the two fundamental doping phenomena in molecular doping of OSCs, namely, the formation of ion pairs (IPAs) and of ground state charge transfer complexes (CPXs). A broad dataset was provided on a prototypical polythiophene and a series of oligomer equivalents along with equally prototypical p-type dopants from the family of TCNQ derivatives. The knowledge created in the present work will therefore serve as a solid foundation for future investigations into the doping of, not only thiophene-based, OSCs and suggests that studies with similarly broad datasets can play an important role in testing the fragmented outcomes of smaller studies against each other. Moreover, the data demonstrated that a multi-technique approach is vital for mitigating ambiguities in the spectroscopic assessment of dopant content. Finally, this thesis proposes three drivers for IPA and CPX formation beyond the host-dopant $IE$-$EA$ energy relation: (i) in a self-amplified process, host HOMO-DOS broadening is triggered for a sufficient amount of initially ionized dopant content leading to further ionization, (ii) IPA formation can be facilitated by an increased host conjugation length, and (iii) crystalline phase CPX-formation can become favorable for an otherwise IPA-forming system below a critical host-dopant stoichiometry.

# Bibliography


[1] H. Hase, "The impact of dopant strength and thermal annealing on p-doped P3HT thin films," Master's thesis, Humboldt-Universität zu Berlin, Berlin, May 2017.

[2] H. Hase, K. O'Neill, J. Frisch, A. Opitz, N. Koch, and I. Salzmann, "Unraveling the Microstructure of Molecularly Doped Poly(3-hexylthiophene) by Thermally Induced Dedoping," *The Journal of Physical Chemistry C*, vol. 122, no. 45, pp. 25 893–25 899, Nov. 2018.

[3] H. Hase and I. Salzmann, "Doping in organic semiconductors," in *Handbook of Organic Materials for Electronic and Photonic Devices, 2nd Edition*, O. Ostroverkhova, Ed. Woodhead Publishing, 2019, pp. 349–383.

[4] J. T. Liu, H. Hase, S. Taylor, I. Salzmann, and P. Forgione, "Approaching the Integer-Charge Transfer Regime in Molecularly Doped Oligothiophenes by Efficient Decarboxylative Cross-Coupling," *Angewandte Chemie International Edition*, vol. 59, no. 18, pp. 7146–7153, Apr. 2020.

[5] S. Bhagat, H. Hase, and I. Salzmann, "Chemical doping of organic semiconductors," in *Organic Flexible Electronics*, P. Cosseddu and M. Caironi, Eds. Elsevier, 2021, pp. 107–141.

[6] H. Hase, M. Berteau-Rainville, S. Charoughchi, E. Orgiu, and I. Salzmann, "Doping-related broadening of the density of states governs integer-charge transfer in P3HT," *Applied Physics Letters*, vol. 118, no. 20, p. 203301, May 2021.

[7] H. Hase, M. Berteau-Rainville, S. Charoughchi, W. Bodlos, E. Orgiu, and I. Salzmann, "Critical dopant concentrations govern integer and fractional charge-transfer phases in doped P3HT," *Journal of Physics: Materials*, vol. 6, no. 1, p. 014004, Jan. 2023.

[8] S. Charoughchi, J. T. Liu, M. Berteau-Rainville, H. Hase, M. S. Askari, S. Bhagat, P. Forgione, and I. Salzmann, "Sterically-Hindered Molecular p-Dopants Promote Integer Charge Transfer in Organic Semiconductors," *Angewandte Chemie International Edition*, vol. 62, no. 31, p. e202304964, Aug. 2023.

[9] F. Hu, M. Berteau-Rainville, H. Hase, Y. Zhang, Q. Wang, I. Salzmann, and S. Duhm, "Energy-Level Alignment Governs Doping Related Fermi-Level Shifts in Polymer Films," *ACS Applied Electronic Materials*, under review, 2023.

[10] C. W. Tang and S. A. VanSlyke, "Organic electroluminescent diodes," *Applied Physics Letters*, vol. 51, no. 12, pp. 913–915, Sep. 1987.

[11] C. W. Tang, "Two-layer organic photovoltaic cell," *Applied Physics Letters*, vol. 48, no. 2, pp. 183–185, Jan. 1986.

[12] G. Horowitz, D. Fichou, X. Peng, Z. Xu, and F. Garnier, "A field-effect transistor based on conjugated alpha-sexithienyl," *Solid State Communications*, vol. 72, no. 4, pp. 381–384, Oct. 1989.

[13] H. Fukagawa, T. Sasaki, T. Tsuzuki, Y. Nakajima, T. Takei, G. Motomura, M. Hasegawa, K. Morii, and T. Shimizu, "Long-Lived Flexible Displays Employing Efficient and Stable Inverted Organic Light-Emitting Diodes," *Advanced Materials*, vol. 30, no. 28, p. 1706768, Jul. 2018.

[14] D. M. Hoffman, P. V. Johnson, J. S. Kim, A. D. Vargas, and M. S. Banks, "240 Hz OLED technology properties that can enable improved image quality: Image quality factors of 240 Hz OLED," *Journal of the Society for Information Display*, vol. 22, no. 7, pp. 346–356, Jul. 2014.

[15] S. Reineke, F. Lindner, G. Schwartz, N. Seidler, K. Walzer, B. Lüssem, and K. Leo, "White organic light-emitting diodes with fluorescent tube efficiency," *Nature*, vol. 459, no. 7244, pp. 234–238, May 2009.

[16] L. J. Richter, D. M. DeLongchamp, and A. Amassian, "Morphology Development in Solution-Processed Functional Organic Blend Films: An In Situ Viewpoint," *Chemical Reviews*, vol. 117, no. 9, pp. 6332–6366, May 2017.

[17] J. Pope and C. Lekakou, "Thermoelectric polymer composite yarns and an energy harvesting wearable textile," *Smart Materials and Structures*, vol. 28, no. 9, p. 095006, Sep. 2019.

[18] N. Okada, K. Sato, M. Yokoo, E. Kodama, S. Kanehashi, and T. Shimomura, "Thermoelectric Properties of Poly(3-hexylthiophene) Nanofiber Aerogels with a Giant Seebeck Coefficient," *ACS Applied Polymer Materials*, vol. 3, no. 1, pp. 455–463, Jan. 2021.

[19] R. R. Søndergaard, M. Hösel, N. Espinosa, M. Jørgensen, and F. C. Krebs, "Practical evaluation of organic polymer thermoelectrics by large-area R2R processing on flexible substrates," *Energy Science & Engineering*, vol. 1, no. 2, pp. 81–88, Sep. 2013.

[20] C. Zisis, E. Pechlivani, S. Tsimikli, E. Mekeridis, A. Laskarakis, and S. Logothetidis, "Organic Photovoltaics on Greenhouse Rooftops: Effects on Plant Growth," *Materials Today: Proceedings*, vol. 19, pp. 65–72, 2019.

[21] J. Mun, J. Kang, Y. Zheng, S. Luo, Y. Wu, H. Gong, J.-C. Lai, H.-C. Wu, G. Xue, J. B.-H. Tok, and Z. Bao, "F4-TCNQ as an Additive to Impart Stretchable Semiconductors with High Mobility and Stability," *Advanced Electronic Materials*, vol. 6, no. 6, p. 2000251, Jun. 2020.

[22] M. Irimia-Vladu, ""Green" electronics: Biodegradable and biocompatible materials and devices for sustainable future," *Chem. Soc. Rev.*, vol. 43, no. 2, pp. 588–610, 2014.

[23] A. Camus, M. Reali, and C. Santato, "Advances in high-resolution printed transistors: The case of bio-sourced organic materials," *Current Opinion in Green and Sustainable Chemistry*, vol. 34, p. 100594, Apr. 2022.

[24] S. Sze and K. K. Ng, *Physics of Semiconductor Devices*. Hoboken, NJ, USA: John Wiley & Sons, Inc., Oct. 2006.

[25] A. D. Scaccabarozzi, A. Basu, F. Aniés, J. Liu, O. Zapata-Arteaga, R. Warren, Y. Firdaus, M. I. Nugraha, Y. Lin, M. Campoy-Quiles, N. Koch, C. Müller, L. Tsetseris, M. Heeney, and T. D. Anthopoulos, "Doping Approaches for Organic Semiconductors," *Chemical Reviews*, vol. 122, no. 4, pp. 4420–4492, Feb. 2022.

[26] K.-H. Yim, G. L. Whiting, C. E. Murphy, J. J. M. Halls, J. H. Burroughes, R. H. Friend, and J.-S. Kim, "Controlling Electrical Properties of Conjugated Polymers via a Solution-Based p-Type Doping," *Advanced Materials*, vol. 20, no. 17, pp. 3319–3324, Sep. 2008.

[27] K. Harada, M. Sumino, C. Adachi, S. Tanaka, and K. Miyazaki, "Improved thermoelectric performance of organic thin-film elements utilizing a bilayer structure of pentacene and 2,3,5,6-tetrafluoro-7,7,8,8-tetracyanoquinodimethane (F4-TCNQ)," *Applied Physics Letters*, vol. 96, no. 25, p. 253304, Jun. 2010.

[28] A. J. Heeger, "Semiconducting and Metallic Polymers: The Fourth Generation of Polymeric Materials (Nobel Lecture)," *Angewandte Chemie International Edition*, vol. 40, no. 14, pp. 2591–2611, Jul. 2001.

[29] Y. Yao, C. Cheng, C. Zhang, H. Hu, K. Wang, and S. De Wolf, "Organic Hole-Transport Layers for Efficient, Stable, and Scalable Inverted Perovskite Solar Cells," *Advanced Materials*, vol. 34, no. 44, p. 2203794, Nov. 2022.

[30] K. Walzer, B. Maennig, M. Pfeiffer, and K. Leo, "Highly Efficient Organic Devices Based on Electrically Doped Transport Layers," *Chemical Reviews*, vol. 107, no. 4, pp. 1233–1271, Apr. 2007.

[31] G. He, K. Walzer, M. P. Pfeiffer, K. Leo, R. Pudzich, and J. Salbeck, "Ultra-high-efficiency electrophosphorescent p-i-n OLEDs with double emission layers," in *Optical Science and Technology, the SPIE 49th Annual Meeting*, Z. H. Kafafi and P. A. Lane, Eds., Denver, CO, Nov. 2004, p. 42.

[32] B. Lüssem, M. Riede, and K. Leo, "Doping of organic semiconductors," *physica status solidi (a)*, vol. 210, no. 1, pp. 9–43, Jan. 2013.

[33] I. Salzmann, G. Heimel, M. Oehzelt, S. Winkler, and N. Koch, "Molecular Electrical Doping of Organic Semiconductors: Fundamental Mechanisms and Emerging Dopant Design Rules," *Accounts of Chemical Research*, vol. 49, no. 3, pp. 370–378, Mar. 2016.

[34] H. Méndez, G. Heimel, S. Winkler, J. Frisch, A. Opitz, K. Sauer, B. Wegner, M. Oehzelt, C. Röthel, S. Duhm, D. Többens, N. Koch, and I. Salzmann, "Charge-transfer crystallites as molecular electrical dopants," *Nature Communications*, vol. 6, no. 1, p. 8560, Dec. 2015.

[35] M. Cui, H. Rui, X. Wu, Z. Sun, W. Qu, W. Qin, and S. Yin, "Coexistent Integer Charge Transfer and Charge Transfer Complex in F4-TCNQ-Doped PTAA for Efficient Flexible Organic Light-Emitting Diodes," *The Journal of Physical Chemistry Letters*, vol. 12, no. 35, pp. 8533–8540, Sep. 2021.

[36] O. Zapata-Arteaga, B. Dörling, A. Perevedentsev, J. Martín, J. S. Reparaz, and M. Campoy-Quiles, "Closing the Stability–Performance Gap in Organic Thermoelectrics by Adjusting the Partial to Integer Charge Transfer Ratio," *Macromolecules*, vol. 53, no. 2, pp. 609–620, Jan. 2020.

[37] A. Babuji, A. Cazorla, E. Solano, C. Habenicht, H. Kleemann, C. Ocal, K. Leo, and E. Barrena, "Charge-Transfer Complexes in Organic Field-Effect Transistors: Superior Suitability for Surface Doping," *ACS Applied Materials & Interfaces*, vol. 14, no. 39, pp. 44 632–44 641, Oct. 2022.

[38] I. Salzmann, G. Heimel, S. Duhm, M. Oehzelt, P. Pingel, B. M. George, A. Schnegg, K. Lips, R.-P. Blum, A. Vollmer, and N. Koch, "Intermolecular Hybridization Governs Molecular Electrical Doping," *Physical Review Letters*, vol. 108, no. 3, p. 035502, Jan. 2012.

[39] I. E. Jacobs, C. Cendra, T. F. Harrelson, Z. I. Bedolla Valdez, R. Faller, A. Salleo, and A. J. Moulé, "Polymorphism controls the degree of charge transfer in a molecularly doped semiconducting polymer," *Materials Horizons*, vol. 5, no. 4, pp. 655–660, 2018.

[40] P. Beyer, D. Pham, C. Peter, N. Koch, E. Meister, W. Brütting, L. Grubert, S. Hecht, D. Nabok, C. Cocchi, C. Draxl, and A. Opitz, "State-of-Matter-Dependent Charge-Transfer Interactions between Planar Molecules for Doping Applications," *Chemistry of Materials*, vol. 31, no. 4, pp. 1237–1249, Feb. 2019.

[41] I. F. Perepichka and D. F. Perepichka, *Handbook of Thiophene-Based Materials: Applications in Organic Electronics and Photonics*. Chichester, U.K: Wiley, 2009.

[42] L. Zhang, N. S. Colella, B. P. Cherniawski, S. C. B. Mannsfeld, and A. L. Briseno, "Oligothiophene Semiconductors: Synthesis, Characterization, and Applications

for Organic Devices," *ACS Applied Materials & Interfaces*, vol. 6, no. 8, pp. 5327–5343, Apr. 2014.

[43] A. Mishra, C.-Q. Ma, and P. Bäuerle, "Functional Oligothiophenes: Molecular Design for Multidimensional Nanoarchitectures and Their Applications †," *Chemical Reviews*, vol. 109, no. 3, pp. 1141–1276, Mar. 2009.

[44] K. A. Mazzio and C. K. Luscombe, "The future of organic photovoltaics," *Chemical Society Reviews*, vol. 44, no. 1, pp. 78–90, 2015.

[45] A. Facchetti, "Semiconductors for organic transistors," *Materials Today*, vol. 10, no. 3, pp. 28–37, Mar. 2007.

[46] F. A. Larik, M. Faisal, A. Saeed, Q. Abbas, M. A. Kazi, N. Abbas, A. A. Thebo, D. M. Khan, and P. A. Channar, "Thiophene-based molecular and polymeric semiconductors for organic field effect transistors and organic thin film transistors," *Journal of Materials Science: Materials in Electronics*, vol. 29, no. 21, pp. 17 975–18 010, Nov. 2018.

[47] K. Kanai, K. Akaike, K. Koyasu, K. Sakai, T. Nishi, Y. Kamizuru, T. Nishi, Y. Ouchi, and K. Seki, "Determination of electron affinity of electron accepting molecules," *Applied Physics A*, vol. 95, no. 1, pp. 309–313, Apr. 2009.

[48] B. Wegner, L. Grubert, C. Dennis, A. Opitz, A. Röttger, Y. Zhang, S. Barlow, S. R. Marder, S. Hecht, K. Müllen, and N. Koch, "Predicting the yield of ion pair formation in molecular electrical doping: Redox-potentials *versus* ionization energy/electron affinity," *Journal of Materials Chemistry C*, vol. 7, no. 44, pp. 13 839–13 848, 2019.

[49] B. Neelamraju, K. E. Watts, J. E. Pemberton, and E. L. Ratcliff, "Correlation of Coexistent Charge Transfer States in $F_4$ TCNQ-Doped P3HT with Microstructure," *The Journal of Physical Chemistry Letters*, vol. 9, no. 23, pp. 6871–6877, Dec. 2018.

[50] H. Méndez, G. Heimel, A. Opitz, K. Sauer, P. Barkowski, M. Oehzelt, J. Soeda, T. Okamoto, J. Takeya, J.-B. Arlin, J.-Y. Balandier, Y. Geerts, N. Koch, and I. Salzmann, "Doping of Organic Semiconductors: Impact of Dopant Strength and Electronic Coupling," *Angewandte Chemie International Edition*, vol. 52, no. 30, pp. 7751–7755, Jul. 2013.

[51] J. S. Chappell, A. N. Bloch, W. A. Bryden, M. Maxfield, T. O. Poehler, and D. O. Cowan, "Degree of charge transfer in organic conductors by infrared absorption spectroscopy," *Journal of the American Chemical Society*, vol. 103, no. 9, pp. 2442–2443, May 1981.

[52] E. Kampar and O. Neilands, "Degree of Charge Transfer in Donor–Acceptor Systems of the $\pi$–$\pi$ Type," *Russian Chemical Reviews*, vol. 55, no. 4, pp. 334–342, Apr. 1986.

[53] M. Meneghetti and C. Pecile, "Charge–transfer organic crystals: Molecular vibrations and spectroscopic effects of electron–molecular vibration coupling of the strong electron acceptor $TCNQF_4$," *The Journal of Chemical Physics*, vol. 84, no. 8, pp. 4149–4162, Apr. 1986.

[54] N. L. Haworth, J. Lu, N. Vo, T. H. Le, C. D. Thompson, A. M. Bond, and L. L. Martin, "Diagnosis of the Redox Levels of $TCNQF_4$ Compounds Using Vibrational Spectroscopy," *ChemPlusChem*, vol. 79, no. 7, pp. 962–972, Jul. 2014.

[55] K. E. Watts, B. Neelamraju, E. L. Ratcliff, and J. E. Pemberton, "Stability of Charge Transfer States in $F_4TCNQ$-Doped P3HT," *Chemistry of Materials*, vol. 31, no. 17, pp. 6986–6994, Sep. 2019.

[56] S. E. Yoon, Y. Kang, G. G. Jeon, D. Jeon, S. Y. Lee, S.-J. Ko, T. Kim, H. Seo, B.-G. Kim, and J. H. Kim, "Exploring Wholly Doped Conjugated Polymer Films Based on Hybrid Doping: Strategic Approach for Optimizing Electrical Conductivity and Related Thermoelectric Properties," *Advanced Functional Materials*, vol. 30, no. 42, p. 2004598, Oct. 2020.

[57] D. A. Stanfield, Y. Wu, S. H. Tolbert, and B. J. Schwartz, "Controlling the Formation of Charge Transfer Complexes in Chemically Doped Semiconducting Polymers," *Chemistry of Materials*, vol. 33, no. 7, pp. 2343–2356, Apr. 2021.

[58] D. A. Stanfield, Z. Mehmedović, and B. J. Schwartz, "Vibrational Stark Effect Mapping of Polaron Delocalization in Chemically Doped Conjugated Polymers," *Chemistry of Materials*, vol. 33, no. 21, pp. 8489–8500, Nov. 2021.

[59] K. E. Watts, K. E. Clary, D. L. Lichtenberger, and J. E. Pemberton, "FTIR Spectroelectrochemistry of F4TCNQ Reduction Products and Their Protonated Forms," *Analytical Chemistry*, vol. 92, no. 10, pp. 7154–7161, May 2020.

[60] K. E. Watts, B. Neelamraju, M. Moser, I. McCulloch, E. L. Ratcliff, and J. E. Pemberton, "Thermally Induced Formation of $HF_4TCNQ^-$ in $F_4TCNQ$-Doped Regioregular P3HT," *The Journal of Physical Chemistry Letters*, vol. 11, no. 16, pp. 6586–6592, Aug. 2020.

[61] M. Berteau-Rainville, E. Orgiu, and I. Salzmann, "On validity and limits of deducing the degree of charge transfer from shifts of cyano vibrations," *Electronic Structure*, vol. 5, no. 3, p. 034002, Sep. 2023.

[62] M. Oehzelt, N. Koch, and G. Heimel, "Organic semiconductor density of states controls the energy level alignment at electrode interfaces," *Nature Communications*, vol. 5, no. 1, p. 4174, Sep. 2014.

[63] M. Oehzelt, K. Akaike, N. Koch, and G. Heimel, "Energy-level alignment at organic heterointerfaces," *Science Advances*, vol. 1, no. 10, p. e1501127, Nov. 2015.

[64] H. Bässler, D. Kroh, F. Schauer, V. Nádaždy, and A. Köhler, "Mapping the Density of States Distribution of Organic Semiconductors by Employing Energy Resolved–Electrochemical Impedance Spectroscopy," *Advanced Functional Materials*, vol. 31, no. 9, p. 2007738, Feb. 2021.

[65] P. Bäuerle, T. Fischer, B. Bidlingmeier, J. P. Rabe, and A. Stabel, "Oligothiophenes—Yet Longer? Synthesis, Characterization, and Scanning Tunneling Microscopy Images of Homologous, Isomerically Pure Oligo(alkylthiophene)s," *Angewandte Chemie International Edition in English*, vol. 34, no. 3, pp. 303–307, 1995.

[66] T. Tao, H.-F. Qian, K. Zhang, J. Geng, and W. Huang, "Functionalized oligothiophene-based heterocyclic aromatic fluorescent compounds with various donor–acceptor spacers and adjustable electronic properties: A theoretical and experimental perspective," *Tetrahedron*, vol. 69, no. 35, pp. 7290–7299, Sep. 2013.

[67] L. Liang, X.-Q. Chen, X. Xiang, J. Ling, W. Shao, Z. Lu, J. Li, W. Wang, and W.-S. Li, "Searching proper oligothiophene segment as centre donor moiety for isoindigo-based small molecular photovoltaic materials," *Organic Electronics*, vol. 42, pp. 93–101, Mar. 2017.

[68] V. M. Manninen, J. P. Heiskanen, K. M. Kaunisto, O. E. O. Hormi, and H. J. Lemmetyinen, "Spectroscopic study of a synthesized Alq3 end-capped oligothiophene applied in organic solar cells," *RSC Advances*, vol. 4, no. 17, pp. 8846–8855, Jan. 2014.

[69] M. Comin, V. Lemaur, A. Giunchi, D. Beljonne, X. Blase, and G. D'Avino, "Doping of semicrystalline conjugated polymers: Dopants within alkyl chains do it better," *Journal of Materials Chemistry C*, vol. 10, no. 37, pp. 13 815–13 825, 2022.

[70] J. Li, I. Duchemin, O. M. Roscioni, P. Friederich, M. Anderson, E. Da Como, G. Kociok-Köhn, W. Wenzel, C. Zannoni, D. Beljonne, X. Blase, and G. D'Avino, "Host dependence of the electron affinity of molecular dopants," *Materials Horizons*, vol. 6, no. 1, pp. 107–114, 2019.

[71] E. Conwell, "Properties of Silicon and Germanium," *Proceedings of the IRE*, vol. 40, no. 11, pp. 1327–1337, Nov. 1952.

[72] P. W. Atkins and R. S. Friedman, *Molecular Quantum Mechanics*, 2nd ed. Oxford University Press, 1983.

[73] A. Köhler and H. Bässler, *Electronic Processes in Organic Semiconductors: An Introduction*. Weinheim: Wiley-VCH, 2015.

[74] J.-L. Bredas, "Mind the gap!" *Mater. Horiz.*, vol. 1, no. 1, pp. 17–19, 2014.

[75] C. M. Cardona, W. Li, A. E. Kaifer, D. Stockdale, and G. C. Bazan, "Electrochemical Considerations for Determining Absolute Frontier Orbital Energy Levels of Conjugated Polymers for Solar Cell Applications," *Advanced Materials*, vol. 23, no. 20, pp. 2367–2371, May 2011.

[76] S. Sweetnam, K. R. Graham, G. O. Ngongang Ndjawa, T. Heumüller, J. A. Bartelt, T. M. Burke, W. Li, W. You, A. Amassian, and M. D. McGehee, "Characterization of the Polymer Energy Landscape in Polymer:Fullerene Bulk Heterojunctions with Pure and Mixed Phases," *Journal of the American Chemical Society*, vol. 136, no. 40, pp. 14 078–14 088, Oct. 2014.

[77] B. Neelamraju, M. Rudolph, and E. L. Ratcliff, "Controlling the Kinetics of Charge Transfer at Conductive Polymer/Liquid Interfaces through Microstructure," *The Journal of Physical Chemistry C*, vol. 122, no. 37, pp. 21 210–21 215, Sep. 2018.

[78] J. K. Harris, B. Neelamraju, and E. L. Ratcliff, "Intersystem Subpopulation Charge Transfer and Conformational Relaxation Preceding *in Situ* Conductivity in Electrochemically Doped Poly(3-hexylthiophene) Electrodes," *Chemistry of Materials*, vol. 31, no. 17, pp. 6870–6879, Sep. 2019.

[79] S. Duhm, G. Heimel, I. Salzmann, H. Glowatzki, R. L. Johnson, A. Vollmer, J. P. Rabe, and N. Koch, "Orientation-dependent ionization energies and interface dipoles in ordered molecular assemblies," *Nature Materials*, vol. 7, no. 4, pp. 326–332, Apr. 2008.

[80] G. D'Avino, S. Duhm, R. G. Della Valle, G. Heimel, M. Oehzelt, S. Kera, N. Ueno, D. Beljonne, and I. Salzmann, "Electrostatic interactions shape molecular organization and electronic structure of organic semiconductor blends," *Chemistry of Materials*, vol. 32, no. 3, pp. 1261–1271, 2020.

[81] V. Gold, Ed., *The IUPAC Compendium of Chemical Terminology: The Gold Book*, 4th ed. Research Triangle Park, NC: International Union of Pure and Applied Chemistry (IUPAC), 2019.

[82] S. S. Zade and M. Bendikov, "From Oligomers to Polymer: Convergence in the HOMO-LUMO Gaps of Conjugated Oligomers," *Organic Letters*, vol. 8, no. 23, pp. 5243–5246, Nov. 2006.

[83] A. Facchetti, M.-H. Yoon, C. L. Stern, G. R. Hutchison, M. A. Ratner, and T. J. Marks, "Building Blocks for N-Type Molecular and Polymeric Electronics. Perfluoroalkyl- versus Alkyl-Functionalized Oligothiophenes (nTs; $n$ = 2-6). Systematic Synthesis, Spectroscopy, Electrochemistry, and Solid-State Organization," *Journal of the American Chemical Society*, vol. 126, no. 41, pp. 13 480–13 501, Oct. 2004.

[84] J. A. E. H. van Haare, E. E. Havinga, J. L. J. van Dongen, R. A. J. Janssen, J. Cornil, and J.-L. Brédas, "Redox States of Long Oligothiophenes: Two Polarons on a Single Chain," *Chemistry – A European Journal*, vol. 4, no. 8, pp. 1509–1522, 1998.

[85] W. Salaneck, O. Inganäs, J.-O. Nilsson, J.-E. Österholm, B. Thémans, and J.-L. Brédas, "Thermochromism in the poly(3-alkylthiophene)s: A study of conformational defects by photoelectron spectroscopy," *Synthetic Metals*, vol. 28, no. 1-2, pp. 451–460, Jan. 1989.

[86] E. F. Aziz, A. Vollmer, S. Eisebitt, W. Eberhardt, P. Pingel, D. Neher, and N. Koch, "Localized Charge Transfer in a Molecularly Doped Conducting Polymer," *Advanced Materials*, vol. 19, no. 20, pp. 3257–3260, Sep. 2007.

[87] G. L. Pearson and J. Bardeen, "Electrical Properties of Pure Silicon and Silicon Alloys Containing Boron and Phosphorus," *Physical Review*, vol. 75, no. 5, pp. 865–883, Mar. 1949.

[88] J.-P. Colinge and C. A. Colinge, *Physics of Semiconductor Devices*. Boston: Kluwer Academic Publishers, 2002.

[89] I. Salzmann and G. Heimel, "Toward a comprehensive understanding of molecular doping organic semiconductors (review)," *Journal of Electron Spectroscopy and Related Phenomena*, vol. 204, pp. 208–222, Oct. 2015.

[90] H. Shirakawa, E. J. Louis, A. G. MacDiarmid, C. K. Chiang, and A. J. Heeger, "Synthesis of electrically conducting organic polymers: Halogen derivatives of polyacetylene, $(CH)_x$," *Journal of the Chemical Society, Chemical Communications*, no. 16, p. 578, 1977.

[91] C. K. Chiang, C. R. Fincher, Y. W. Park, A. J. Heeger, H. Shirakawa, E. J. Louis, S. C. Gau, and A. G. MacDiarmid, "Electrical Conductivity in Doped Polyacetylene," *Physical Review Letters*, vol. 39, no. 17, pp. 1098–1101, Oct. 1977.

[92] N. Basescu, Z.-X. Liu, D. Moses, A. J. Heeger, H. Naarmann, and N. Theophilou, "High electrical conductivity in doped polyacetylene," *Nature*, vol. 327, no. 6121, pp. 403–405, Jun. 1987.

[93] Y. Yamamoto, K. Yoshino, and Y. Inuishi, "Electrical Properties of Phthalocyanine-Halogen Complexes," *Journal of the Physical Society of Japan*, vol. 47, no. 6, pp. 1887–1891, Dec. 1979.

[94] G. Parthasarathy, C. Shen, A. Kahn, and S. R. Forrest, "Lithium doping of semiconducting organic charge transport materials," *Journal of Applied Physics*, vol. 89, no. 9, pp. 4986–4992, May 2001.

[95] J. Bernstein, *Polymorphism in Molecular Crystals*, ser. International Union of Crystallography Monographs on Crystallography. OxfordClarendon Press ; New York: Oxford University Press, 2002, no. 14.

[96] O. D. Jurchescu, D. A. Mourey, S. Subramanian, S. R. Parkin, B. M. Vogel, J. E. Anthony, T. N. Jackson, and D. J. Gundlach, "Effects of polymorphism on charge transport in organic semiconductors," *Physical Review B*, vol. 80, no. 8, p. 085201, Aug. 2009.

[97] J. Simbrunner, C. Simbrunner, B. Schrode, C. Röthel, N. Bedoya-Martinez, I. Salzmann, and R. Resel, "Indexing of grazing-incidence X-ray diffraction patterns: The case of fibre-textured thin films," *Acta Crystallographica Section A Foundations and Advances*, vol. 74, no. 4, pp. 373–387, Jul. 2018.

[98] J. Simbrunner, S. Hofer, B. Schrode, Y. Garmshausen, S. Hecht, R. Resel, and I. Salzmann, "Indexing grazing-incidence X-ray diffraction patterns of thin films: Lattices of higher symmetry," *Journal of Applied Crystallography*, vol. 52, no. 2, pp. 428–439, Apr. 2019.

[99] J. Simbrunner, I. Salzmann, and R. Resel, "Indexing of grazing-incidence X-ray diffraction patterns," *Crystallography Reviews*, vol. 29, no. 1, pp. 19–37, Jan. 2023.

[100] A. O. F. Jones, B. Chattopadhyay, Y. H. Geerts, and R. Resel, "Substrate-Induced and Thin-Film Phases: Polymorphism of Organic Materials on Surfaces," *Advanced Functional Materials*, vol. 26, no. 14, pp. 2233–2255, Apr. 2016.

[101] I. Salzmann, D. Nabok, M. Oehzelt, S. Duhm, A. Moser, G. Heimel, P. Puschnig, C. Ambrosch-Draxl, J. P. Rabe, and N. Koch, "Structure Solution of the 6,13-Pentacenequinone Surface-Induced Polymorph by Combining X-ray Diffraction Reciprocal-Space Mapping and Theoretical Structure Modeling," *Crystal Growth & Design*, vol. 11, no. 2, pp. 600–606, Feb. 2011.

[102] I. Salzmann, A. Moser, M. Oehzelt, T. Breuer, X. Feng, Z.-Y. Juang, D. Nabok, R. G. Della Valle, S. Duhm, G. Heimel, A. Brillante, E. Venuti, I. Bilotti, C. Christodoulou, J. Frisch, P. Puschnig, C. Draxl, G. Witte, K. Müllen, and N. Koch, "Epitaxial Growth of $\pi$-Stacked Perfluoropentacene on Graphene-Coated Quartz," *ACS Nano*, vol. 6, no. 12, pp. 10 874–10 883, Dec. 2012.

[103] S.-i. Machida, Y. Nakayama, S. Duhm, Q. Xin, A. Funakoshi, N. Ogawa, S. Kera, N. Ueno, and H. Ishii, "Highest-Occupied-Molecular-Orbital Band Dispersion of Rubrene Single Crystals as Observed by Angle-Resolved Ultraviolet Photoelectron Spectroscopy," *Physical Review Letters*, vol. 104, no. 15, p. 156401, Apr. 2010.

[104] S. Fratini, D. Mayou, and S. Ciuchi, "The Transient Localization Scenario for Charge Transport in Crystalline Organic Materials," *Advanced Functional Materials*, vol. 26, no. 14, pp. 2292–2315, Apr. 2016.

[105] H. Bässler and A. Köhler, "Charge Transport in Organic Semiconductors," in *Unimolecular and Supramolecular Electronics I*, R. M. Metzger, Ed. Berlin, Heidelberg: Springer Berlin Heidelberg, 2011, vol. 312, pp. 1–65.

[106] G. Horowitz, "Validity of the concept of band edge in organic semiconductors," *Journal of Applied Physics*, vol. 118, no. 11, p. 115502, Sep. 2015.

[107] H. Bässler, "Charge Transport in Disordered Organic Photoconductors a Monte Carlo Simulation Study," *physica status solidi (b)*, vol. 175, no. 1, pp. 15–56, Jan. 1993.

[108] M. Lögdlund, R. Lazzaroni, S. Stafström, W. R. Salaneck, and J.-L. Brédas, "Direct observation of charge-induced $\pi$-electronic structural changes in a conjugated polymer," *Physical Review Letters*, vol. 63, no. 17, pp. 1841–1844, Oct. 1989.

[109] S. Olthof, W. Tress, R. Meerheim, B. Lüssem, and K. Leo, "Photoelectron spectroscopy study of systematically varied doping concentrations in an organic semiconductor layer using a molecular p-dopant," *Journal of Applied Physics*, vol. 106, no. 10, p. 103711, Nov. 2009.

[110] W. Gao and A. Kahn, "Controlled p doping of the hole-transport molecular material N,N′-diphenyl-N,N′-bis(1-naphthyl)-1,1′-biphenyl-4,4′-diamine with tetrafluorotetracyanoquinodimethane," *Journal of Applied Physics*, vol. 94, no. 1, pp. 359–366, Jun. 2003.

[111] ——, "Effect of electrical doping on molecular level alignment at organic–organic heterojunctions," *Applied Physics Letters*, vol. 82, no. 26, pp. 4815–4817, Jun. 2003.

[112] ——, "Electrical doping: The impact on interfaces of $\pi$-conjugated molecular films," *Journal of Physics: Condensed Matter*, vol. 15, no. 38, pp. S2757–S2770, Oct. 2003.

[113] ——, "Controlled p-doping of zinc phthalocyanine by coevaporation with tetrafluorotetracyanoquinodimethane: A direct and inverse photoemission study," *Applied Physics Letters*, vol. 79, no. 24, pp. 4040–4042, Dec. 2001.

[114] S. Olthof, R. Meerheim, M. Schober, and K. Leo, "Energy level alignment at the interfaces in a multilayer organic light-emitting diode structure," *Physical Review B*, vol. 79, no. 24, p. 245308, Jun. 2009.

[115] A. J. Heeger, S. Kivelson, J. R. Schrieffer, and W. P. Su, "Solitons in conducting polymers," *Reviews of Modern Physics*, vol. 60, no. 3, pp. 781–850, Jul. 1988.

[116] J. L. Bredas and G. B. Street, "Polarons, bipolarons, and solitons in conducting polymers," *Accounts of Chemical Research*, vol. 18, no. 10, pp. 309–315, Oct. 1985.

[117] O. Bubnova, Z. U. Khan, H. Wang, S. Braun, D. R. Evans, M. Fabretto, P. Hojati-Talemi, D. Dagnelund, J.-B. Arlin, Y. H. Geerts, S. Desbief, D. W. Breiby, J. W. Andreasen, R. Lazzaroni, W. M. Chen, I. Zozoulenko, M. Fahlman, P. J. Murphy, M. Berggren, and X. Crispin, "Semi-metallic polymers," *Nature Materials*, vol. 13, no. 2, pp. 190–194, Feb. 2014.

[118] R. Österbacka, C. P. An, X. M. Jiang, and Z. V. Vardeny, "Two-Dimensional Electronic Excitations in Self-Assembled Conjugated Polymer Nanocrystals," *Science*, vol. 287, no. 5454, pp. 839–842, Feb. 2000.

[119] S. Winkler, P. Amsalem, J. Frisch, M. Oehzelt, G. Heimel, and N. Koch, "Probing the energy levels in hole-doped molecular semiconductors," *Materials Horizons*, vol. 2, no. 4, pp. 427–433, 2015.

[120] J. Hubbard, "Electron Correlations in Narrow Energy Bands," *Proceedings of the Royal Society A: Mathematical, Physical and Engineering Sciences*, vol. 276, no. 1365, pp. 238–257, Nov. 1963.

[121] R.-Q. Png, M. C. Ang, M.-H. Teo, K.-K. Choo, C. G. Tang, D. Belaineh, L.-L. Chua, and P. K. Ho, "Madelung and Hubbard interactions in polaron band model of doped organic semiconductors," *Nature Communications*, vol. 7, p. 11948, Sep. 2016.

[122] J. Torrance, B. Scott, and F. Kaufman, "Optical properties of charge transfer salts of tetracyanoquinodimethane (TCNQ)," *Solid State Communications*, vol. 17, no. 11, pp. 1369–1373, Dec. 1975.

[123] I. Zanon and C. Pecile, "Vibronic structure of the near-infrared and visible electronic transitions of 7,7,8,8-tetracyanoquinodimethane radical anion," *The Journal of Physical Chemistry*, vol. 87, no. 19, pp. 3657–3664, Sep. 1983.

[124] P. Pingel and D. Neher, "Comprehensive picture of p -type doping of P3HT with the molecular acceptor F 4 TCNQ," *Physical Review B*, vol. 87, no. 11, p. 115209, Mar. 2013.

[125] U. Salzner, "Theoretical Investigation of Excited States of Oligothiophenes and of Their Monocations," *Journal of Chemical Theory and Computation*, vol. 3, no. 3, pp. 1143–1157, May 2007.

[126] G. Heimel, "The Optical Signature of Charges in Conjugated Polymers," *ACS Central Science*, vol. 2, no. 5, pp. 309–315, May 2016.

[127] K. Fesser, A. R. Bishop, and D. K. Campbell, "Optical absorption from polarons in a model of polyacetylene," *Physical Review B*, vol. 27, no. 8, pp. 4804–4825, Apr. 1983.

[128] E. Zojer, J. Cornil, G. Leising, and J. L. Brédas, "Theoretical investigation of the geometric and optical properties of neutral and charged oligophenylenes," *Physical Review B*, vol. 59, no. 12, pp. 7957–7968, Mar. 1999.

[129] B. Wegner, D. Lungwitz, A. E. Mansour, C. E. Tait, N. Tanaka, T. Zhai, S. Duhm, M. Forster, J. Behrends, Y. Shoji, A. Opitz, U. Scherf, E. J. W. List-Kratochvil, T. Fukushima, and N. Koch, "An Organic Borate Salt with Superior *p* -Doping Capability for Organic Semiconductors," *Advanced Science*, vol. 7, no. 17, p. 2001322, Sep. 2020.

[130] D. Tsokkou, P. Cavassin, G. Rebetez, and N. Banerji, "Bipolarons rule the short-range terahertz conductivity in electrochemically doped P3HT," *Materials Horizons*, vol. 9, no. 1, pp. 482–491, 2022.

[131] C. Enengl, S. Enengl, S. Pluczyk, M. Havlicek, M. Lapkowski, H. Neugebauer, and E. Ehrenfreund, "Doping-Induced Absorption Bands in P3HT: Polarons and Bipolarons," *ChemPhysChem*, vol. 17, no. 23, pp. 3836–3844, Dec. 2016.

[132] Y. Zhong, V. Untilova, D. Muller, S. Guchait, C. Kiefer, L. Herrmann, N. Zimmermann, M. Brosset, T. Heiser, and M. Brinkmann, "Preferential Location of Dopants

in the Amorphous Phase of Oriented Regioregular Poly(3-hexylthiophene-2,5-diyl) Films Helps Reach Charge Conductivities of 3000 S $cm^{-1}$," *Advanced Functional Materials*, vol. 32, no. 30, p. 2202075, Jul. 2022.

[133] G. Heimel, I. Salzmann, S. Duhm, and N. Koch, "Design of Organic Semiconductors from Molecular Electrostatics," *Chemistry of Materials*, vol. 23, no. 3, pp. 359–377, Feb. 2011.

[134] G. Heimel, I. Salzmann, S. Duhm, J. P. Rabe, and N. Koch, "Intrinsic Surface Dipoles Control the Energy Levels of Conjugated Polymers," *Advanced Functional Materials*, vol. 19, no. 24, pp. 3874–3879, Dec. 2009.

[135] H. Li, M. E. DeCoster, R. M. Ireland, J. Song, P. E. Hopkins, and H. E. Katz, "Modification of the Poly(bisdodecylquaterthiophene) Structure for High and Predominantly Nonionic Conductivity with Matched Dopants," *Journal of the American Chemical Society*, vol. 139, no. 32, pp. 11 149–11 157, Aug. 2017.

[136] R. Kroon, D. Kiefer, D. Stegerer, L. Yu, M. Sommer, and C. Müller, "Polar Side Chains Enhance Processability, Electrical Conductivity, and Thermal Stability of a Molecularly p-Doped Polythiophene," *Advanced Materials*, vol. 29, no. 24, p. 1700930, Jun. 2017.

[137] B. X. Dong, C. Nowak, J. W. Onorato, T. Ma, J. Niklas, O. G. Poluektov, G. Grocke, M. F. DiTusa, F. A. Escobedo, C. K. Luscombe, P. F. Nealey, and S. N. Patel, "Complex Relationship between Side-Chain Polarity, Conductivity, and Thermal Stability in Molecularly Doped Conjugated Polymers," *Chemistry of Materials*, vol. 33, no. 2, pp. 741–753, Jan. 2021.

[138] A. Hamidi-Sakr, L. Biniek, J.-L. Bantignies, D. Maurin, L. Herrmann, N. Leclerc, P. Lévêque, V. Vijayakumar, N. Zimmermann, and M. Brinkmann, "A Versatile Method to Fabricate Highly In-Plane Aligned Conducting Polymer Films with Anisotropic Charge Transport and Thermoelectric Properties: The Key Role of Alkyl Side Chain Layers on the Doping Mechanism," *Advanced Functional Materials*, vol. 27, no. 25, p. 1700173, Jul. 2017.

[139] S. Nagamatsu and S. S. Pandey, "Ordered arrangement of F4TCNQ anions in three-dimensionally oriented P3HT thin films," *Scientific Reports*, vol. 10, no. 1, p. 20020, Dec. 2020.

[140] V. Untilova, T. Biskup, L. Biniek, V. Vijayakumar, and M. Brinkmann, "Control of Chain Alignment and Crystallization Helps Enhance Charge Conductivities and Thermoelectric Power Factors in Sequentially Doped P3HT:$F_4$TCNQ Films," *Macromolecules*, vol. 53, no. 7, pp. 2441–2453, Apr. 2020.

[141] D. T. Scholes, P. Y. Yee, J. R. Lindemuth, H. Kang, J. Onorato, R. Ghosh, C. K. Luscombe, F. C. Spano, S. H. Tolbert, and B. J. Schwartz, "The Effects of Crystallinity on Charge Transport and the Structure of Sequentially Processed $F_4$TCNQ-Doped

Conjugated Polymer Films," *Advanced Functional Materials*, vol. 27, no. 44, p. 1702654, Nov. 2017.

[142] C. E. Tait, A. Reckwitz, M. Arvind, D. Neher, R. Bittl, and J. Behrends, "Spin–spin interactions and spin delocalisation in a doped organic semiconductor probed by EPR spectroscopy," *Physical Chemistry Chemical Physics*, vol. 23, no. 25, pp. 13 827–13 841, 2021.

[143] A. M. Valencia and C. Cocchi, "Electronic and Optical Properties of Oligothiophene-F4TCNQ Charge-Transfer Complexes: The Role of the Donor Conjugation Length," *The Journal of Physical Chemistry C*, vol. 123, no. 14, pp. 9617–9623, Apr. 2019.

[144] K.-F. Braun and S. W. Hla, "Charge transfer in the TCNQ-sexithiophene complex," *The Journal of Chemical Physics*, vol. 129, no. 6, p. 064707, Aug. 2008.

[145] T. Salzillo, M. Masino, G. Kociok-Köhn, D. Di Nuzzo, E. Venuti, R. G. Della Valle, D. Vanossi, C. Fontanesi, A. Girlando, A. Brillante, and E. Da Como, "Structure, Stoichiometry, and Charge Transfer in Cocrystals of Perylene with TCNQ-$F_x$," *Crystal Growth & Design*, vol. 16, no. 5, pp. 3028–3036, May 2016.

[146] K. Tashiro, Y. Minagawa, M. Kobayashi, S. Morita, T. Kawai, and K. Yoshino, "Structure and thermochromic solid-state phase transition of poly(3-alkylthiophene): [3] effects of alkyl side chain length on the phase transitional behavior," *Synthetic Metals*, vol. 55, no. 1, pp. 321–328, Mar. 1993.

[147] K. Tashiro, M. Kobayashi, T. Kawai, and K. Yoshino, "Crystal structural change in poly(3-alkyl thiophene)s induced by iodine doping as studied by an organized combination of X-ray diffraction, infrared/Raman spectroscopy and computer simulation techniques," *Polymer*, vol. 38, no. 12, pp. 2867–2879, Jun. 1997.

[148] P. Pingel, L. Zhu, K. S. Park, J.-O. Vogel, S. Janietz, E.-G. Kim, J. P. Rabe, J.-L. Brédas, and N. Koch, "Charge-Transfer Localization in Molecularly Doped Thiophene-Based Donor Polymers," *The Journal of Physical Chemistry Letters*, vol. 1, no. 13, pp. 2037–2041, Jul. 2010.

[149] A. Fediai, F. Symalla, P. Friederich, and W. Wenzel, "Disorder compensation controls doping efficiency in organic semiconductors," *Nature Communications*, vol. 10, no. 1, p. 4547, Dec. 2019.

[150] P. Y. Yee, D. T. Scholes, B. J. Schwartz, and S. H. Tolbert, "Dopant-Induced Ordering of Amorphous Regions in Regiorandom P3HT," *The Journal of Physical Chemistry Letters*, vol. 10, no. 17, pp. 4929–4934, Sep. 2019.

[151] T.-A. Chen, X. Wu, and R. D. Rieke, "Regiocontrolled Synthesis of Poly(3-alkylthiophenes) Mediated by Rieke Zinc: Their Characterization and Solid-State Properties," *Journal of the American Chemical Society*, vol. 117, no. 1, pp. 233–244, Jan. 1995.

[152] X. Jiang, C. An, R. Österbacka, and Z. Vardeny, "FTIR studies of charged photoexcitations in regio-regular and regio-random poly(3-alkylthiophene) films," *Synthetic Metals*, vol. 116, no. 1-3, pp. 203–206, Jan. 2001.

[153] J. Gao, E. T. Niles, and J. K. Grey, "Aggregates Promote Efficient Charge Transfer Doping of Poly(3-hexylthiophene)," *The Journal of Physical Chemistry Letters*, vol. 4, no. 17, pp. 2953–2957, Sep. 2013.

[154] A. A. Y. Guilbert, M. Zbiri, P. A. Finn, M. Jenart, P. Fouquet, V. Cristiglio, B. Frick, J. Nelson, and C. B. Nielsen, "Mapping Microstructural Dynamics up to the Nanosecond of the Conjugated Polymer P3HT in the Solid State," *Chemistry of Materials*, vol. 31, no. 23, pp. 9635–9651, Dec. 2019.

[155] J.-O. Vogel, I. Salzmann, S. Duhm, M. Oehzelt, J. P. Rabe, and N. Koch, "Phase-separation and mixing in thin films of co-deposited rod-like conjugated molecules," *Journal of Materials Chemistry*, vol. 20, no. 20, p. 4055, 2010.

[156] T. J. Aubry, J. C. Axtell, V. M. Basile, K. J. Winchell, J. R. Lindemuth, T. M. Porter, J.-Y. Liu, A. N. Alexandrova, C. P. Kubiak, S. H. Tolbert, A. M. Spokoyny, and B. J. Schwartz, "Dodecaborane-Based Dopants Designed to Shield Anion Electrostatics Lead to Increased Carrier Mobility in a Doped Conjugated Polymer," *Advanced Materials*, vol. 31, no. 11, p. 1805647, 2019.

[157] T. J. Aubry, K. J. Winchell, C. Z. Salamat, V. M. Basile, J. R. Lindemuth, J. M. Stauber, J. C. Axtell, R. M. Kubena, M. D. Phan, M. J. Bird, A. M. Spokoyny, S. H. Tolbert, and B. J. Schwartz, "Tunable Dopants with Intrinsic Counterion Separation Reveal the Effects of Electron Affinity on Dopant Intercalation and Free Carrier Production in Sequentially Doped Conjugated Polymer Films," *Advanced Functional Materials*, vol. 30, no. 28, p. 2001800, 2020.

[158] J. Gao, J. D. Roehling, Y. Li, H. Guo, A. J. Moulé, and J. K. Grey, "The effect of 2,3,5,6-tetrafluoro-7,7,8,8-tetracyanoquinodimethane charge transfer dopants on the conformation and aggregation of poly(3-hexylthiophene)," *Journal of Materials Chemistry C*, vol. 1, no. 36, p. 5638, 2013.

[159] A. Y. Sosorev and D. Y. Paraschuk, "Charge-Transfer Complexes of Conjugated Polymers," *Israel Journal of Chemistry*, vol. 54, no. 5-6, pp. 650–673, Jun. 2014.

[160] Y. Yoshida, K. Isomura, Y. Kumagai, M. Maesato, H. Kishida, M. Mizuno, and G. Saito, "Coronene-based charge-transfer complexes," *Journal of Physics: Condensed Matter*, vol. 28, no. 30, p. 304001, Aug. 2016.

[161] F. Ghani, A. Opitz, P. Pingel, G. Heimel, I. Salzmann, J. Frisch, D. Neher, A. Tsami, U. Scherf, and N. Koch, "Charge transfer in and conductivity of molecularly doped thiophene-based copolymers," *Journal of Polymer Science Part B: Polymer Physics*, vol. 53, no. 1, pp. 58–63, Jan. 2015.

[162] D. T. Duong, C. Wang, E. Antono, M. F. Toney, and A. Salleo, "The chemical and structural origin of efficient p-type doping in P3HT," *Organic Electronics*, vol. 14, no. 5, pp. 1330–1336, May 2013.

[163] S. Bhagat, W. D. Leal, M. B. Majewski, J. Simbrunner, S. Hofer, R. Resel, and I. Salzmann, "Aggregate formation in crystalline blends of $\alpha$-sexithiophene and para-sexiphenyl," *Electronic Structure*, vol. 3, no. 3, p. 034004, Sep. 2021.

[164] M. T. Fontana, D. A. Stanfield, D. T. Scholes, K. J. Winchell, S. H. Tolbert, and B. J. Schwartz, "Evaporation vs Solution Sequential Doping of Conjugated Polymers: $F_4$ TCNQ Doping of Micrometer-Thick P3HT Films for Thermoelectrics," *The Journal of Physical Chemistry C*, vol. 123, no. 37, pp. 22 711–22 724, Sep. 2019.

[165] P. R. Griffiths and J. A. de Haseth, *Fourier Transform Infrared Spectrometry*. Hoboken, NJ, USA: John Wiley & Sons, Inc., Apr. 2007.

[166] M. Pal and M. Pradhan, "Quantum Cascade Laser Spectroscopy," in *Modern Techniques of Spectroscopy*, D. K. Singh, M. Pradhan, and A. Materny, Eds. Singapore: Springer Singapore, 2021, vol. 13, pp. 363–387.

[167] K. Yeh, S. Kenkel, J.-N. Liu, and R. Bhargava, "Fast Infrared Chemical Imaging with a Quantum Cascade Laser," *Analytical Chemistry*, vol. 87, no. 1, pp. 485–493, Jan. 2015.

[168] T. Konevskikh, A. Ponossov, R. Blümel, R. Lukacs, and A. Kohler, "Fringes in FTIR spectroscopy revisited: Understanding and modelling fringes in infrared spectroscopy of thin films," *The Analyst*, vol. 140, no. 12, pp. 3969–3980, 2015.

[169] N. Elgrishi, K. J. Rountree, B. D. McCarthy, E. S. Rountree, T. T. Eisenhart, and J. L. Dempsey, "A Practical Beginner's Guide to Cyclic Voltammetry," *Journal of Chemical Education*, vol. 95, no. 2, pp. 197–206, Feb. 2018.

[170] F. Scholz, A. Bond, R. Compton, D. Fiedler, G. Inzelt, H. Kahlert, Š. Komorsky-Lovrić, H. Lohse, M. Lovrić, F. Marken, A. Neudeck, U. Retter, F. Scholz, and Z. Stojek, Eds., *Electroanalytical Methods*. Berlin, Heidelberg: Springer Berlin Heidelberg, 2010.

[171] R. R. Gagne, C. A. Koval, and G. C. Lisensky, "Ferrocene as an internal standard for electrochemical measurements," *Inorganic Chemistry*, vol. 19, no. 9, pp. 2854–2855, Sep. 1980.

[172] A. Lausi, M. Polentarutti, S. Onesti, J. R. Plaisier, E. Busetto, G. Bais, L. Barba, A. Cassetta, G. Campi, D. Lamba, A. Pifferi, S. C. Mande, D. D. Sarma, S. M. Sharma, and G. Paolucci, "Status of the crystallography beamlines at Elettra," *The European Physical Journal Plus*, vol. 130, no. 3, p. 43, Mar. 2015.

[173] M. Birkholz, *Thin Film Analysis by X-Ray Scattering*. Weinheim, FRG: Wiley-VCH Verlag GmbH & Co. KGaA, Oct. 2005.

[174] N. Kayunkid, S. Uttiya, and M. Brinkmann, "Structural Model of Regioregular Poly(3-hexylthiophene) Obtained by Electron Diffraction Analysis," *Macromolecules*, vol. 43, no. 11, pp. 4961–4967, Jun. 2010.

[175] I. K. Robinson and D. J. Tweet, "Surface X-ray diffraction," *Reports on Progress in Physics*, vol. 55, no. 5, pp. 599–651, May 1992.

[176] M. Neuschitzer, A. Moser, A. Neuhold, J. Kraxner, B. Stadlober, M. Oehzelt, I. Salzmann, R. Resel, and J. Novák, "Grazing-incidence in-plane X-ray diffraction on ultra-thin organic films using standard laboratory equipment," *Journal of Applied Crystallography*, vol. 45, no. 2, pp. 367–370, Apr. 2012.

[177] S. Schiefer, M. Huth, A. Dobrinevski, and B. Nickel, "Determination of the Crystal Structure of Substrate-Induced Pentacene Polymorphs in Fiber Structured Thin Films," *Journal of the American Chemical Society*, vol. 129, no. 34, pp. 10 316–10 317, Aug. 2007.

[178] A. Neuhold, J. Novák, H.-G. Flesch, A. Moser, T. Djuric, L. Grodd, S. Grigorian, U. Pietsch, and R. Resel, "X-ray radiation damage of organic semiconductor thin films during grazing incidence diffraction experiments," *Nuclear Instruments and Methods in Physics Research Section B: Beam Interactions with Materials and Atoms*, vol. 284, pp. 64–68, Aug. 2012.

[179] B. Schrode, S. Pachmajer, M. Dohr, C. Röthel, J. Domke, T. Fritz, R. Resel, and O. Werzer, "*GIDVis*: A comprehensive software tool for geometry-independent grazing-incidence X-ray diffraction data analysis and pole-figure calculations," *Journal of Applied Crystallography*, vol. 52, no. 3, pp. 683–689, Jun. 2019.

[180] B. Toby and M. Suchomel, "Mail-in synchrotron powder diffraction at the APS." *Synchrotron Radiation in Natural Science*, vol. 10, no. 1-2, pp. 77–80, Jan. 2011.

[181] R. García, "Dynamic atomic force microscopy methods," *Surface Science Reports*, vol. 47, no. 6-8, pp. 197–301, Sep. 2002.

[182] G. J. Leggett, "Scanning Probe Microscopy," in *Surface Analysis– The Principal Techniques*, J. C. Vickerman and I. S. Gilmore, Eds. Chichester, UK: John Wiley & Sons, Ltd, Apr. 2009, pp. 479–562.

[183] D. Shen, W.-C. Chen, M.-F. Lo, and C.-S. Lee, "Charge-transfer complexes and their applications in optoelectronic devices," *Materials Today Energy*, vol. 20, p. 100644, Jun. 2021.

[184] E. C.-K. Wu, C. Z. Salamat, S. H. Tolbert, and B. J. Schwartz, "Molecular Dynamics Study of the Thermodynamics of Integer Charge Transfer vs Charge-Transfer Complex Formation in Doped Conjugated Polymers," *ACS Applied Materials & Interfaces*, vol. 14, no. 23, pp. 26 988–27 001, Jun. 2022.

[185] V. Nádaždy, F. Schauer, and K. Gmucová, "Energy resolved electrochemical impedance spectroscopy for electronic structure mapping in organic semiconductors," *Applied Physics Letters*, vol. 105, no. 14, p. 142109, Oct. 2014.

[186] J. Lorrmann, M. Ruf, D. Vocke, V. Dyakonov, and C. Deibel, "Distribution of charge carrier transport properties in organic semiconductors with Gaussian disorder," *Journal of Applied Physics*, vol. 115, no. 18, p. 183702, May 2014.

[187] C. Deibel, D. Mack, J. Gorenflot, A. Schöll, S. Krause, F. Reinert, D. Rauh, and V. Dyakonov, "Energetics of excited states in the conjugated polymer poly(3-hexylthiophene)," *Physical Review B*, vol. 81, no. 8, p. 085202, Feb. 2010.

[188] Y. Krupskaya, M. Gibertini, N. Marzari, and A. F. Morpurgo, "Band-Like Electron Transport with Record-High Mobility in the TCNQ Family," *Advanced Materials*, vol. 27, no. 15, pp. 2453–2458, Apr. 2015.

[189] F. M. Wiygul, T. J. Emge, J. P. Ferraris, and T. J. Kistenmacher, "Crystal Structure of Monofluoro-7,7,8,8-Tetracyano-p-Quinodimethane, TCNQF. Evidence for Strong One-Dimensional Coupling of Molecular Dipole Moments," *Molecular Crystals and Liquid Crystals*, vol. 71, no. 3-4, pp. 303–314, Aug. 1981.

[190] F. M. Wiygul, J. P. Ferraris, T. J. Emge, and T. J. Kistenmacher, "Crystal, Molecular and Electronic Structure of the Electron Acceptor 2,5-difluoro-7,7,8,8-Tetracyano-p-quinodimethane, 2,5-TCNQF2," *Molecular Crystals and Liquid Crystals*, vol. 78, no. 1, pp. 279–293, Dec. 1981.

[191] T. J. Emge, M. Maxfield, D. O. Cowan, and T. J. Kistenmacher, "Solution and Solid State Studies of Tetrafluoro-7,7,8,8-Tetracyano- *p* -Quinodimethane, TCNQF4. Evidence for Long-Range Amphoteric Intermolecular Interactions and Low-Dimensionality in the Solid State Structure," *Molecular Crystals and Liquid Crystals*, vol. 65, no. 3-4, pp. 161–178, Mar. 1981.

[192] F. Panzer, H. Bässler, and A. Köhler, "Temperature Induced Order–Disorder Transition in Solutions of Conjugated Polymers Probed by Optical Spectroscopy," *The Journal of Physical Chemistry Letters*, vol. 8, no. 1, pp. 114–125, Jan. 2017.

[193] M. L. Tietze, J. Benduhn, P. Pahner, B. Nell, M. Schwarze, H. Kleemann, M. Krammer, K. Zojer, K. Vandewal, and K. Leo, "Elementary steps in electrical doping of organic semiconductors," *Nature Communications*, vol. 9, no. 1, p. 1182, Dec. 2018.

[194] M. Schwarze, C. Gaul, R. Scholz, F. Bussolotti, A. Hofacker, K. S. Schellhammer, B. Nell, B. D. Naab, Z. Bao, D. Spoltore, K. Vandewal, J. Widmer, S. Kera, N. Ueno, F. Ortmann, and K. Leo, "Molecular parameters responsible for thermally activated transport in doped organic semiconductors," *Nature Materials*, vol. 18, no. 3, pp. 242–248, Mar. 2019.

[195] I. Ikemoto, K. Samizo, T. Fujikawa, K. Ishii, T. Ohta, and H. Kuroda, "Photoelectron spectra of tetracyanoethylene (TCNE) and tetracyanochinodimethane (TCNQ)," *Chemistry Letters*, vol. 3, no. 7, pp. 785–790, Jul. 1974.

[196] W. Gao and A. Kahn, "Electronic structure and current injection in zinc phthalocyanine doped with tetrafluorotetracyanoquinodimethane: Interface versus bulk effects," *Organic Electronics*, vol. 3, no. 2, pp. 53–63, Jun. 2002.

[197] J.-D. Chai and M. Head-Gordon, "Long-range corrected hybrid density functionals with damped atom–atom dispersion corrections," *Physical Chemistry Chemical Physics*, vol. 10, no. 44, p. 6615, 2008.

[198] M. J. Frisch, G. W. Trucks, H. B. Schlegel, G. E. Scuseria, M. A. Robb, J. R. Cheeseman, G. Scalmani, V. Barone, B. Mennucci, G. A. Petersson, H. Nakatsuji, M. Caricato, X. Li, H. P. Hratchian, A. F. Izmaylov, J. Bloino, G. Zheng, J. L. Sonnenberg, M. Hada, M. Ehara, K. Toyota, R. Fukuda, J. Hasegawa, M. Ishida, T. Nakajima, Y. Honda, O. Kitao, H. Nakai, T. Vreven, J. A. Montgomery, Jr., J. E. Peralta, F. Ogliaro, M. Bearpark, J. J. Heyd, E. Brothers, K. N. Kudin, V. N. Staroverov, R. Kobayashi, J. Normand, K. Raghavachari, A. Rendell, J. C. Burant, S. S. Iyengar, J. Tomasi, M. Cossi, N. Rega, J. M. Millam, M. Klene, J. E. Knox, J. B. Cross, V. Bakken, C. Adamo, J. Jaramillo, R. Gomperts, R. E. Stratmann, O. Yazyev, A. J. Austin, R. Cammi, C. Pomelli, J. W. Ochterski, R. L. Martin, K. Morokuma, V. G. Zakrzewski, G. A. Voth, P. Salvador, J. J. Dannenberg, S. Dapprich, A. D. Daniels, Ö. Farkas, J. B. Foresman, J. V. Ortiz, J. Cioslowski, and D. J. Fox, "Gaussian 09 Revision E.01 (Gaussian Inc., Wallingford, CT)," Wallingford, CT, 2009.

[199] T. Lu and F. Chen, "Multiwfn: A multifunctional wavefunction analyzer," *Journal of Computational Chemistry*, vol. 33, no. 5, pp. 580–592, Feb. 2012.

[200] M. Wojdyr, "*Fityk* : A general-purpose peak fitting program," *Journal of Applied Crystallography*, vol. 43, no. 5, pp. 1126–1128, Oct. 2010.

[201] J. D. Hunter, "Matplotlib: A 2D Graphics Environment," *Computing in Science & Engineering*, vol. 9, no. 3, pp. 90–95, 2007.

[202] M. B. Qarai, R. Ghosh, and F. C. Spano, "Understanding Bipolarons in Conjugated Polymers Using a Multiparticle Holstein Approach," *The Journal of Physical Chemistry C*, vol. 125, no. 44, pp. 24 487–24 497, Nov. 2021.

[203] A. R. Chew, R. Ghosh, Z. Shang, F. C. Spano, and A. Salleo, "Sequential Doping Reveals the Importance of Amorphous Chain Rigidity in Charge Transport of Semi-Crystalline Polymers," *The Journal of Physical Chemistry Letters*, vol. 8, no. 20, pp. 4974–4980, Oct. 2017.

[204] R. Ghosh, A. R. Chew, J. Onorato, V. Pakhnyuk, C. K. Luscombe, A. Salleo, and F. C. Spano, "Spectral Signatures and Spatial Coherence of Bound and Unbound Polarons in P3HT Films: Theory Versus Experiment," *The Journal of Physical Chemistry C*, vol. 122, no. 31, pp. 18 048–18 060, Aug. 2018.

[205] N. Vo, N. L. Haworth, A. M. Bond, and L. L. Martin, "Investigation of the Redox and Acid-Base properties of TCNQF and TCNQF $_2$ : Electrochemistry, Vibrational

Spectroscopy, and Substituent Effects," *ChemElectroChem*, vol. 5, no. 8, pp. 1173–1185, Apr. 2018.

[206] H. Sirringhaus, P. J. Brown, R. H. Friend, M. M. Nielsen, K. Bechgaard, B. M. W. Langeveld-Voss, A. J. H. Spiering, R. A. J. Janssen, E. W. Meijer, P. Herwig, and D. M. de Leeuw, "Two-dimensional charge transport in self-organized, high-mobility conjugated polymers," *Nature*, vol. 401, no. 6754, pp. 685–688, Oct. 1999.

[207] P. A. Finn, I. E. Jacobs, J. Armitage, R. Wu, B. D. Paulsen, M. Freeley, M. Palma, J. Rivnay, H. Sirringhaus, and C. B. Nielsen, "Effect of polar side chains on neutral and p-doped polythiophene," *Journal of Materials Chemistry C*, vol. 8, no. 45, pp. 16 216–16 223, 2020.

[208] K. Rahimi, I. Botiz, N. Stingelin, N. Kayunkid, M. Sommer, F. P. V. Koch, H. Nguyen, O. Coulembier, P. Dubois, M. Brinkmann, and G. Reiter, "Controllable Processes for Generating Large Single Crystals of Poly(3-hexylthiophene)," *Angewandte Chemie International Edition*, vol. 51, no. 44, pp. 11 131–11 135, Oct. 2012.

[209] R. E. Long, R. A. Sparks, and K. N. Trueblood, "The crystal and molecular structure of 7,7,8,8-tetracyanoquinodimethane," *Acta Crystallographica*, vol. 18, no. 5, pp. 932–939, May 1965.

[210] J. Yamamoto and Y. Furukawa, "Electronic and Vibrational Spectra of Positive Polarons and Bipolarons in Regioregular Poly(3-hexylthiophene) Doped with Ferric Chloride," *The Journal of Physical Chemistry B*, vol. 119, no. 13, pp. 4788–4794, Apr. 2015.

[211] B. D'Andrade, S. Datta, S. Forrest, P. Djurovich, E. Polikarpov, and M. Thompson, "Relationship between the ionization and oxidation potentials of molecular organic semiconductors," *Organic Electronics*, vol. 6, no. 1, pp. 11–20, Feb. 2005.

[212] I. Salzmann, S. Duhm, G. Heimel, M. Oehzelt, R. Kniprath, R. L. Johnson, J. P. Rabe, and N. Koch, "Tuning the Ionization Energy of Organic Semiconductor Films: The Role of Intramolecular Polar Bonds," *Journal of the American Chemical Society*, vol. 130, no. 39, pp. 12 870–12 871, Oct. 2008.

[213] H. Yoshida, K. Yamada, J. Tsutsumi, and N. Sato, "Complete description of ionization energy and electron affinity in organic solids: Determining contributions from electronic polarization, energy band dispersion, and molecular orientation," *Physical Review B*, vol. 92, no. 7, p. 075145, Aug. 2015.

[214] V. I. Arkhipov, P. Heremans, E. V. Emelianova, and H. Bässler, "Effect of doping on the density-of-states distribution and carrier hopping in disordered organic semiconductors," *Physical Review B*, vol. 71, no. 4, p. 045214, Jan. 2005.

[215] E. M. Thomas, E. C. Davidson, R. Katsumata, R. A. Segalman, and M. L. Chabinyc, "Branched Side Chains Govern Counterion Position and Doping Mechanism in Conjugated Polythiophenes," *ACS Macro Letters*, vol. 7, no. 12, pp. 1492–1497, Dec. 2018.

[216] P. Reiser, M. Konrad, A. Fediai, S. Léon, W. Wenzel, and P. Friederich, "Analyzing Dynamical Disorder for Charge Transport in Organic Semiconductors via Machine Learning," *Journal of Chemical Theory and Computation*, vol. 17, no. 6, pp. 3750–3759, Jun. 2021.

[217] A. Fediai, A. Emering, F. Symalla, and W. Wenzel, "Disorder-driven doping activation in organic semiconductors," *Physical Chemistry Chemical Physics*, vol. 22, no. 18, pp. 10 256–10 264, 2020.

[218] J. Armleder, T. Strunk, F. Symalla, P. Friederich, J. Enrique Olivares Peña, T. Neumann, W. Wenzel, and A. Fediai, "Computing Charging and Polarization Energies of Small Organic Molecules Embedded into Amorphous Materials with Quantum Accuracy," *Journal of Chemical Theory and Computation*, vol. 17, no. 6, pp. 3727–3738, Jun. 2021.

[219] J. T. Liu, "Decarboxylative Cross-Coupling as An Efficient Synthetic Tool for Thiophene-Based Materials," Master's thesis, Concordia University, Dec. 2019.

[220] S. S. Zade and M. Bendikov, "Study of Hopping Transport in Long Oligothiophenes and Oligoselenophenes: Dependence of Reorganization Energy on Chain Length," *Chemistry - A European Journal*, vol. 14, no. 22, pp. 6734–6741, Jul. 2008.

[221] J. Frisch, A. Vollmer, J. P. Rabe, and N. Koch, "Ultrathin polythiophene films on an intrinsically conducting polymer electrode: Charge transfer induced valence states and interface dipoles," *Organic Electronics*, vol. 12, no. 6, pp. 916–922, Jun. 2011.

[222] F. C. Spano, "Modeling disorder in polymer aggregates: The optical spectroscopy of regioregular poly(3-hexylthiophene) thin films," *The Journal of Chemical Physics*, vol. 122, no. 23, p. 234701, Jun. 2005.

[223] ——, "Absorption in regio-regular poly(3-hexyl)thiophene thin films: Fermi resonances, interband coupling and disorder," *Chemical Physics*, vol. 325, no. 1, pp. 22–35, Jun. 2006.

[224] J. Clark, J.-F. Chang, F. C. Spano, R. H. Friend, and C. Silva, "Determining exciton bandwidth and film microstructure in polythiophene films using linear absorption spectroscopy," *Applied Physics Letters*, vol. 94, no. 16, p. 163306, Apr. 2009.

[225] D. Kiefer, R. Kroon, A. I. Hofmann, H. Sun, X. Liu, A. Giovannitti, D. Stegerer, A. Cano, J. Hynynen, L. Yu, Y. Zhang, D. Nai, T. F. Harrelson, M. Sommer, A. J. Moulé, M. Kemerink, S. R. Marder, I. McCulloch, M. Fahlman, S. Fabiano, and C. Müller, "Double doping of conjugated polymers with monomer molecular dopants," *Nature Materials*, Jan. 2019.

[226] D. A. Dixon, J. C. Calabrese, and J. S. Miller, "Crystal and molecular structure of the 2:1 charge-transfer salt of decamethylferrocene and perfluoro-7,7,8,8-tetracyano-p-quinodimethane: [[Fe(C5Me5)2]+.cntdot.]2[TCNQF4]2-. The electronic structure of [TCNQF4]n (n = 0, 1-, 2-)," *The Journal of Physical Chemistry*, vol. 93, no. 6, pp. 2284–2291, Mar. 1989.

[227] J. Armleder, T. Neumann, F. Symalla, T. Strunk, J. E. Olivares Peña, W. Wenzel, and A. Fediai, "Controlling doping efficiency in organic semiconductors by tuning short-range overscreening," *Nature Communications*, vol. 14, no. 1, p. 1356, Mar. 2023.

[228] V. Vijayakumar, P. Durand, H. Zeng, V. Untilova, L. Herrmann, P. Algayer, N. Leclerc, and M. Brinkmann, "Influence of dopant size and doping method on the structure and thermoelectric properties of PBTTT films doped with $F_6$TCNNQ and $F_4$TCNQ," *Journal of Materials Chemistry C*, vol. 8, no. 46, pp. 16 470–16 482, 2020.

[229] M. S. A. Abdou, F. P. Orfino, Y. Son, and S. Holdcroft, "Interaction of Oxygen with Conjugated Polymers: Charge Transfer Complex Formation with Poly(3-alkylthiophenes)," *Journal of the American Chemical Society*, vol. 119, no. 19, pp. 4518–4524, May 1997.

[230] J. Li, C. W. Rochester, I. E. Jacobs, E. W. Aasen, S. Friedrich, P. Stroeve, and A. J. Moulé, "The effect of thermal annealing on dopant site choice in conjugated polymers," *Organic Electronics*, vol. 33, pp. 23–31, Jun. 2016.

[231] N. T. Vo, L. L. Martin, and A. M. Bond, "A Systematic (Spectro-) Electrochemical Approach to the Synthesis and Characterisation of Co(II) and Ni(II) Compounds Containing Reduced Forms of TCNQF," *ChemElectroChem*, vol. 6, no. 1, pp. 221–228, Jan. 2019.

[232] K. S. Ahn, H. Jo, J. B. Kim, I. Seo, H. H. Lee, and D. R. Lee, "Structural Transition and Interdigitation of Alkyl Side Chains in the Conjugated Polymer Poly(3-hexylthiophene) and Their Effects on the Device Performance of the Associated Organic Field-Effect Transistor," *ACS Applied Materials & Interfaces*, vol. 12, no. 1, pp. 1142–1150, Jan. 2020.

[233] M. Skompska and A. Szkurłat, "The influence of the structural defects and microscopic aggregation of poly(3-alkylthiophenes) on electrochemical and optical properties of the polymer films: Discussion of an origin of redox peaks in the cyclic voltammograms," *Electrochimica Acta*, vol. 46, no. 26-27, pp. 4007–4015, Aug. 2001.

# Appendix A

# Fourier-Transform Infrared Spectroscopy (FTIR) on Sample Aging

To gauge the influence of air exposure in the wake of the GIXRD measurements, the FTIR samples were stored in ambient conditions for a week and then the spectra were re-taken (dashed lines in figure 4.3; see section 4.2). These tests also capture the impact of oxygen-doping [229] and effects of possible changes of spatial rearrangement (e.g. F4TCNQ is known to readily diffuse through P3HT at room temperature [230]) which could create or destroy charge-transfer complex (CPX) and ion-pair (IPA) arrangements. Overall, no significant changes can be seen, with a few exceptions. Most notably, the CPX peak $\nu_{\mathrm{CPX}}$ in 9% F4TCNQ shifted from 2207 $\mathrm{cm}^{-1}$ to 2215 $\mathrm{cm}^{-1}$. The latter peak was also found in a publication by Zapata-Arteaga et al. [36] where all sample preparation handling took place in ambient conditions. While this would point to an oxygen- or humidity-caused change in the CPX, a study by Watts et al. [55] focused on P3HT-F4TCNQ aging and found no such shift in the CPX peak. Moving on, 5 and 17% F2TCNQ, as well as 17% FTCNQ see a relative increase in the IPA peak $\nu_1$, along with a higher neutral peak $\nu_0$ in 17% F2TCNQ and stronger $\nu_{\mathrm{CPX}}$ in 17% FTCNQ. However, no significant trends can be made out and, most importantly, the 5 and 17% samples that were sent for GIXRD still represent the initial spectra, qualitatively.

# Appendix B

# Revisiting $IE$ and $EA$ Values in the Comparison of Doping 4T and P3HT

Table B.1: UPS/IPES- *versus* CV-derived $IE/EA$ values for the discussion of IPA and CPX formation in P3HT and 4T, respectively. UPS/IPES-derived values are the ones employed by Méndez et al. [34] (additional values in parenthesis). CV-derived values are converted from redox potentials as explained in section 4.2.5. †Estimated from the oligothiophene series in [83] (see main text) since CV data on 4T was not successfully measured, to date.

| | 4T | F4TCNQ | P3HT | FTCNQ |
|---|---|---|---|---|
| Method | $IE$ (eV) | $EA$ (eV) | $IE$ (eV) | $EA$ (eV) |
| UPS/IPES | 5.3 [34] | 5.24 [113] (5.08 [47]) | 4.6 [221] (4.8 [148]) | 4.55 [47] |
| CV | 5.6† | 5.31 | 5.21 | 4.73 |

Méndez et al. [34] previously found that polymers and oligomers favor IPA and CPX formation, respectively. This hypothesis should briefly be revisited since the study employed UPS/IPES-derived $IE/EA$ values while Wegner et al. [48] recently reported that those derived from CV offer superior accuracy in the prediction of IPA formation. Table B.1 shows that the choice of $IE/EA$ values employed in the comparison of F4TCNQ-doped 4T and P3HT doped with, e.g., FTCNQ; in both cases the $IE$ matches the $EA$ value according to UPS/IPES data but only the polymer case exhibited IPA formation [34].

While there exists no CV-derived $IE$ value for 4T to date, one can safely assume about (5.6±0.1) eV from trends observed by Facchetti et al. [83] on the 4T derivatives h4T (there, labeled 'isoDH-4T'; 5.63 eV) and 5,5‴-dihexyl-2,2′:5′,2″:5″,2‴-quarterthiophene (there, labeled 'DH-4T'; 5.52 eV) in comparison with 5T (5.57 eV) and 6T (5.54 eV). The $EA$ of F4TCNQ does now not match the $IE$ of 4T but is, instead, about 0.3 eV weaker. Nevertheless, the original observation by Méndez et al. [34] still holds and even gains in support, as the $EA$ of FTCNQ is now about 0.5 eV weaker than the $IE$ of P3HT, making IPA formation even less expected in this case.

# Appendix C

# Supporting Data

## C.1 Optical Absorption Spectroscopy

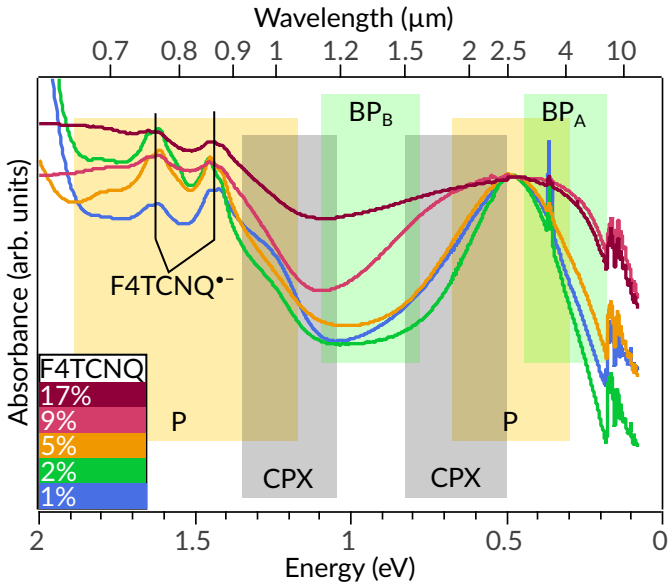


Figure C.1: UV-vis/NIR merged with FTIR thin-film absorbance spectra of P3HT doped with F4TCNQ at increasing dopant molar ratios $\chi$; focused on broad features contributing to the absorption below 2 eV; absorption caused by polarons is marked by 'P' [33, 39, 124], charge-transfer complex by 'CPX' [39], and bipolarons by 'BP$_A$' [131, 202] and 'BP$_B$' [130]. All spectra are normalized to the 0.48 eV (polaron) absorbance; sharp peaks below 0.5 eV are due to vibrational transitions in the mid infrared. Note that the FTIR data below 0.5 eV should only be regarded as a qualitative addition to the UV-vis/NIR data due to the differences between the two experiments that are explained in section 3.2.3.

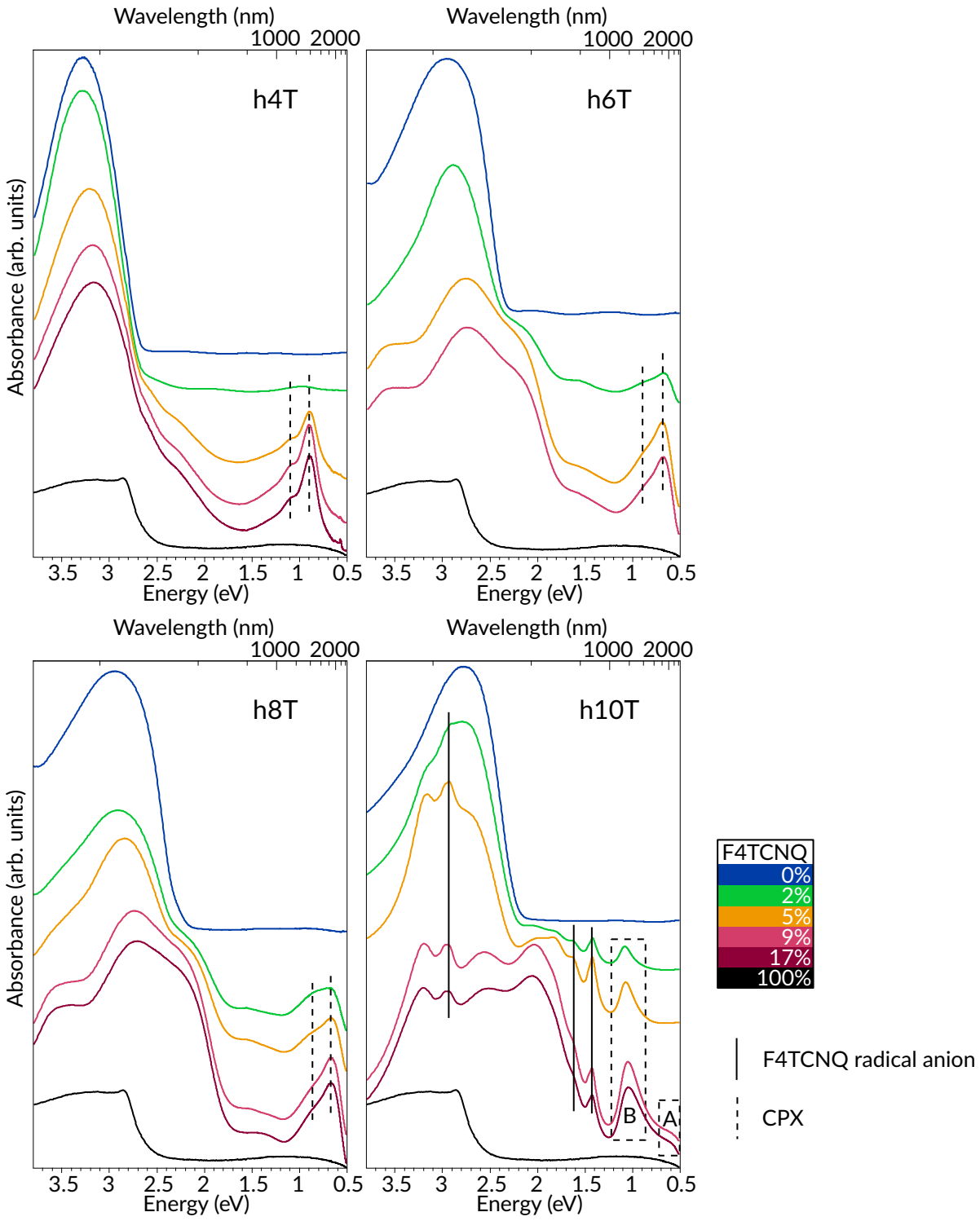


Figure C.2: UV-vis/NIR thin-film absorbance spectra of h4T, h6T, h8T, and doped with F4TCNQ at increasing dopant molar ratios $\chi$ *versus* thiophene-ring unit, as well as spectra of the corresponding pure compounds; peaks 'A' and 'B' are discussed in chapter 5 as the indicators of charged h10T and the h10T-F4TCNQ CPX, respectively

## C.2 Vibrational Absorption Spectroscopy

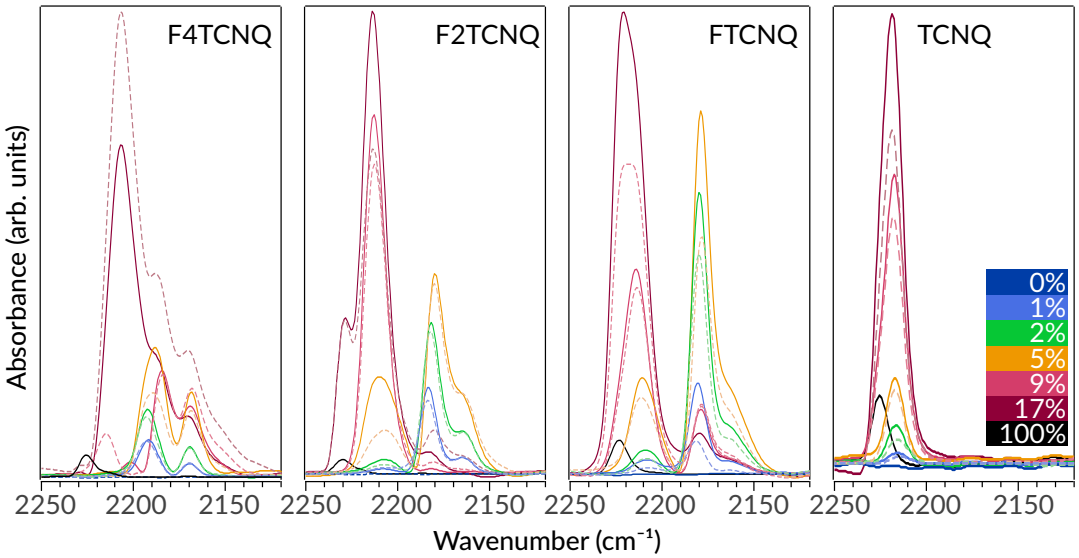


Figure C.3: Non-normalized FTIR thin-film absorbance spectra of P3HT doped with FxTCNQ (x=0,1,2,4) at increasing dopant molar ratios $\chi$ as well as the corresponding pure compounds; focused on the C≡N stretching modes of the dopants. Solid-line spectra were recorded under inert $N_2$ atmosphere and faded dashed-line spectra stem from the same samples after one week of aging and 1 h full exposure to ambient conditions (see section 4.2).

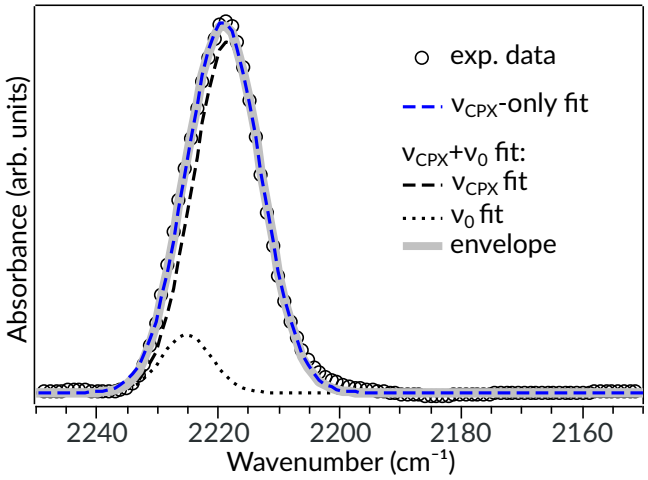


Figure C.4: Fits of the C≡N stretching modes of 17% TCNQ in P3HT. The assumption of a neutral-dopant peak $\nu_0$ is ambiguous as the CPX-related peak $\nu_{CPX}$ is not significantly affected besides a slight hardening which, however, is observed at high $\chi$ with all TCNQ derivatives investigated, here.

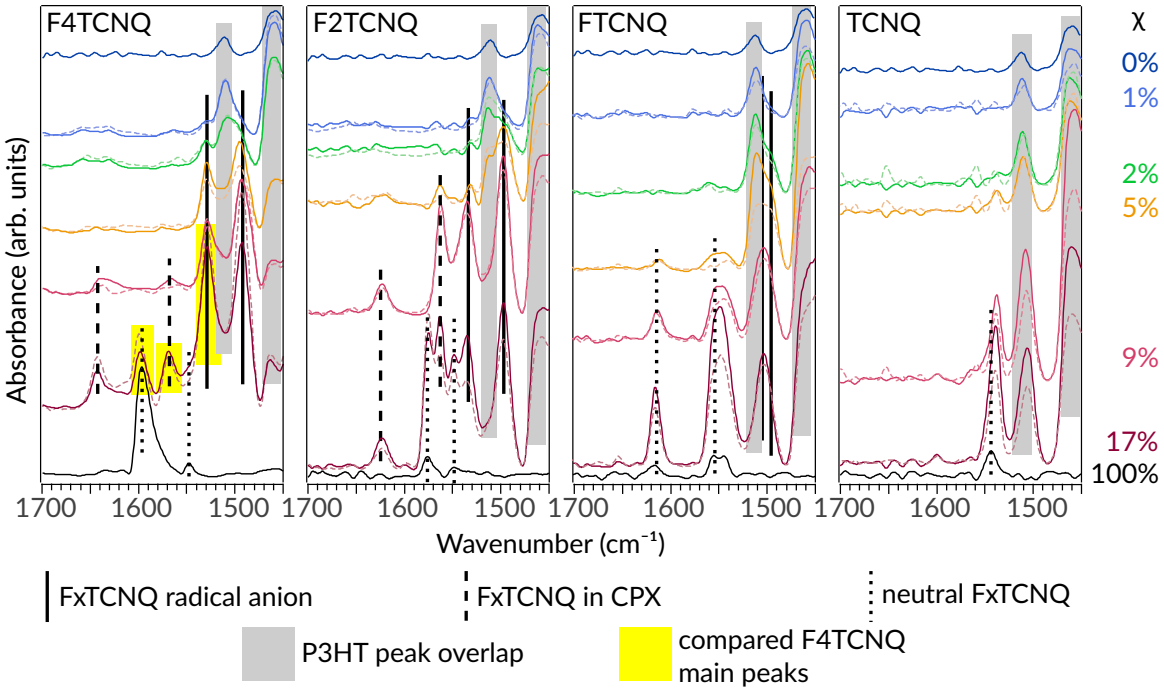


Figure C.5: FTIR thin-film absorbance spectra of P3HT doped with FxTCNQ (x=0,1,2,4) at increasing dopant molar ratios $\chi$ as well as those of the corresponding pure compounds; focused on the dopant ring C=C stretching modes (also showing exocyclic C=C stretching [54, 205] and P3HT thiophene ring modes [146, 147]). Solid-line spectra were recorded under inert $N_2$ atmosphere and faded dashed-line spectra stem from the same samples after one week of aging and 1 h full exposure to ambient conditions (see section 4.2). Peak positions from P3HT according to [146]; these do not shift for ionized P3HT [147]. Indicated peaks of neutral dopants and their radical anion are at known positions for F4TCNQ [53, 145, 205], F2TCNQ [145, 205], FTCNQ [205, 231], and TCNQ [145, 205]. CPX features of F4TCNQ and F2TCNQ are assigned by exclusion. Peaks between the positions for neutral and ionized dopant are likely shifts between them, depending on degree of charge transfer, as explained in the main text for the C≡N stretching modes. However, the peaks above 1600 $cm^{-1}$ are more likely to stem from non-shifting Raman-active modes [205] that become IR-active upon CPX formation. For 17% F4TCNQ, peaks highlighted in yellow are considered in the main text when explaining that, here, the ionized peak is dominant while CPX formation would prevail according to the C≡N modes (figure 4.3). A similar, yet, less stark discrepancy in relative peak presence is also observed between the yellow highlighted 17% F2TCNQ peaks and their C≡N-mode equivalents.

## C.3 Grazing-Incidence X-Ray Diffraction (GIXRD)

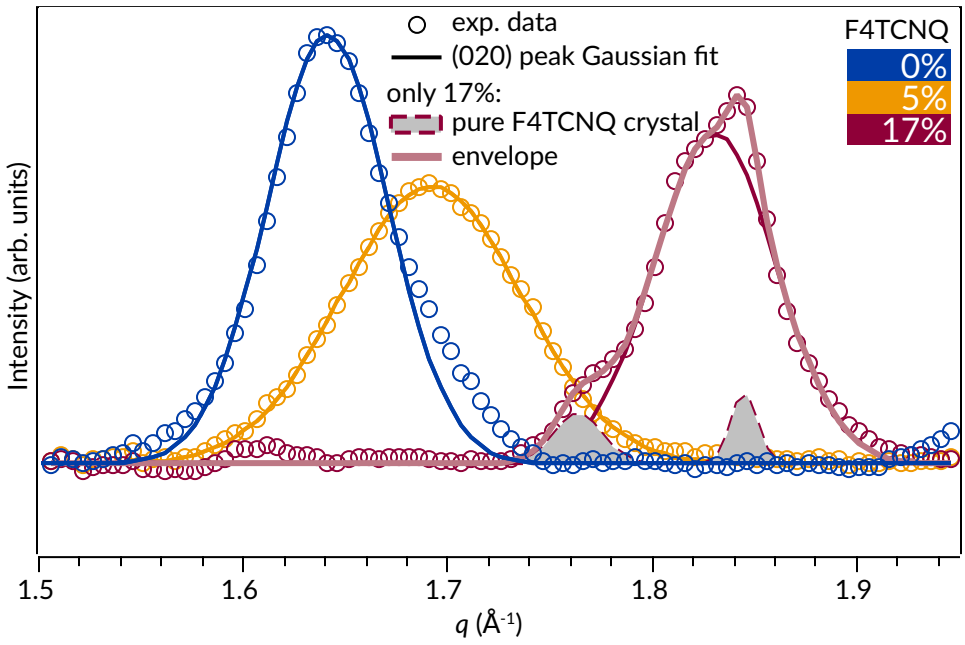


Figure C.6: Exemplary fits of GIXRD line scans; selected to demonstrate the broader FWHM of the (020) peak for IPA-rich 5% F4TCNQ molar ratio (0.10 $Å^{-1}$) *versus* pure P3HT (0%) and CPX-rich 17% F4TCNQ loading (both 0.07 $Å^{-1}$).

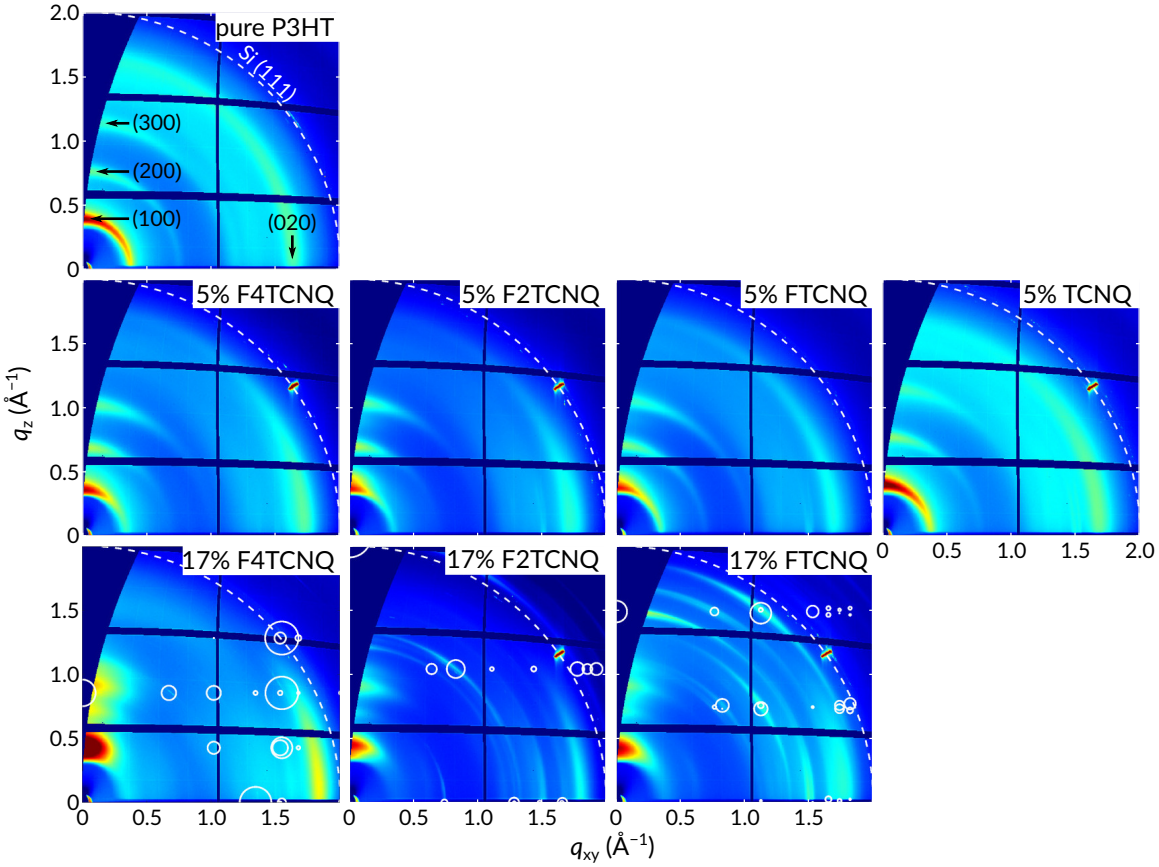


Figure C.7: GIXRD reciprocal space maps on films of pure P3HT as well as doped with FxTCNQ (x=0,1,2,4) at increasing dopant molar ratios $\chi$, recorded at Elettra Sincrotrone Trieste, Italy (incomplete, preliminary investigation to the data in figure C.8). $q_z$, $q_{xy}$ are the out-of-plane and in-plane components of the scattering vector $\mathbf{q}$, respectively. Colors correspond to intensities on a logarithmic scale. (100), (200), and (300) indicate the lamellar spacing of the P3HT chains while (020) stems from their π-π backbone(-dopant) stacking. Features marked by white circles (area proportional to structure factor) stem from pure TCNQ [209], FTCNQ [189], F2TCNQ [190], and F4TCNQ [191]. The features around 1.5 Å$^{-1}$ and close to the $q_{xy}$ axis would fit the packing of interdigitated hexyl side chains as found by Ahn et al. [232] in low-temperature pure P3HT thin films. Here, it might be a side-effect of a CPX polymorph. The P3HT-F4TCNQ CPX model by Jacobs et al. [39] predicts such side chain packing, however, their experimental data exhibits no such diffraction feature.

Figure C.8: (on next page) GIXRD reciprocal space maps on films of pure P3HT as well as doped with FxTCNQ (x=0,1,2,4) at increasing dopant molar ratios $\chi$ recorded at Canadian Light Source Saskatoon, SK, Canada; see caption under figure C.7, above, for more details.

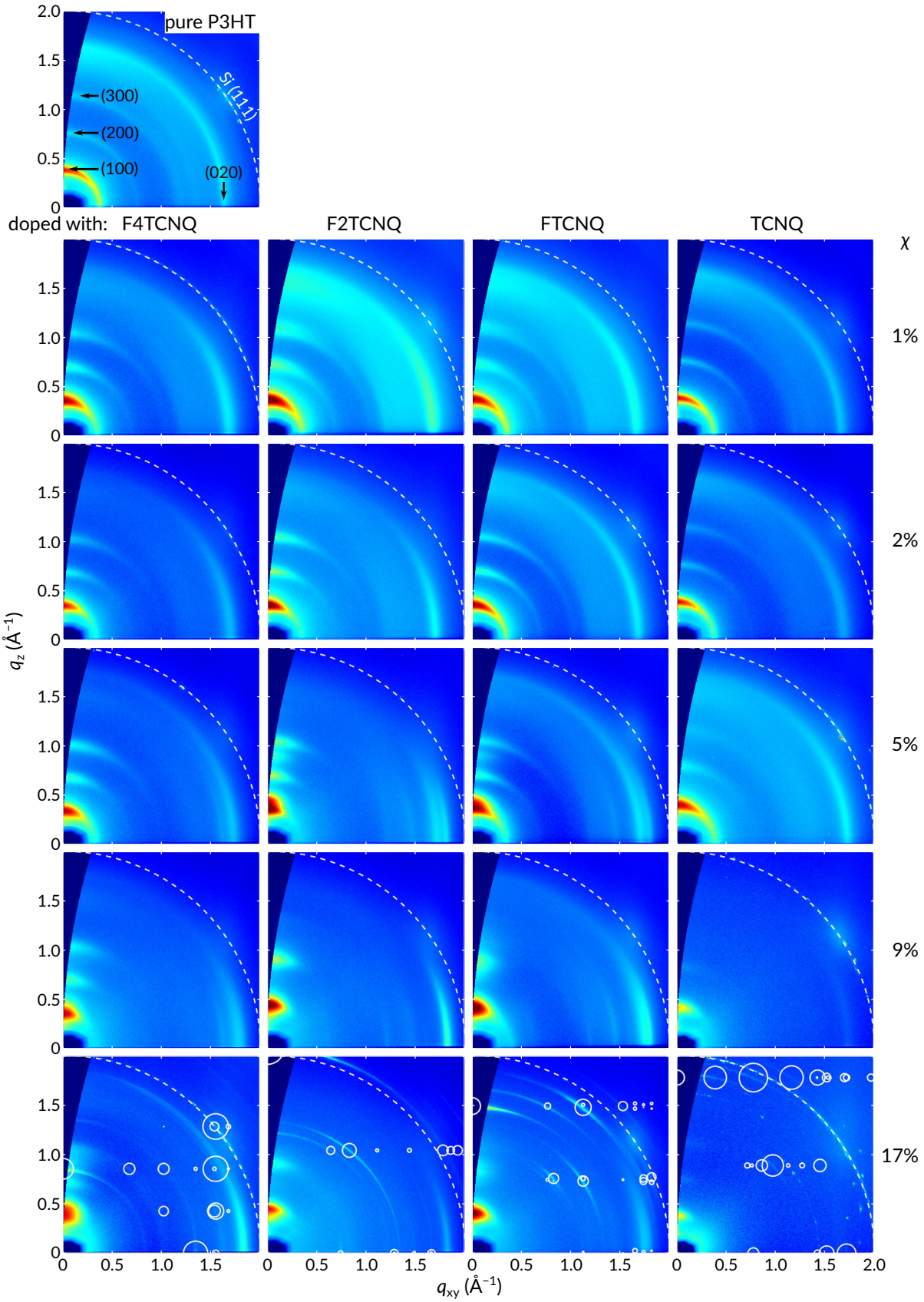


Figure C.8: Caption on previous page.

## C.4 Cyclic Voltammetry (CV)

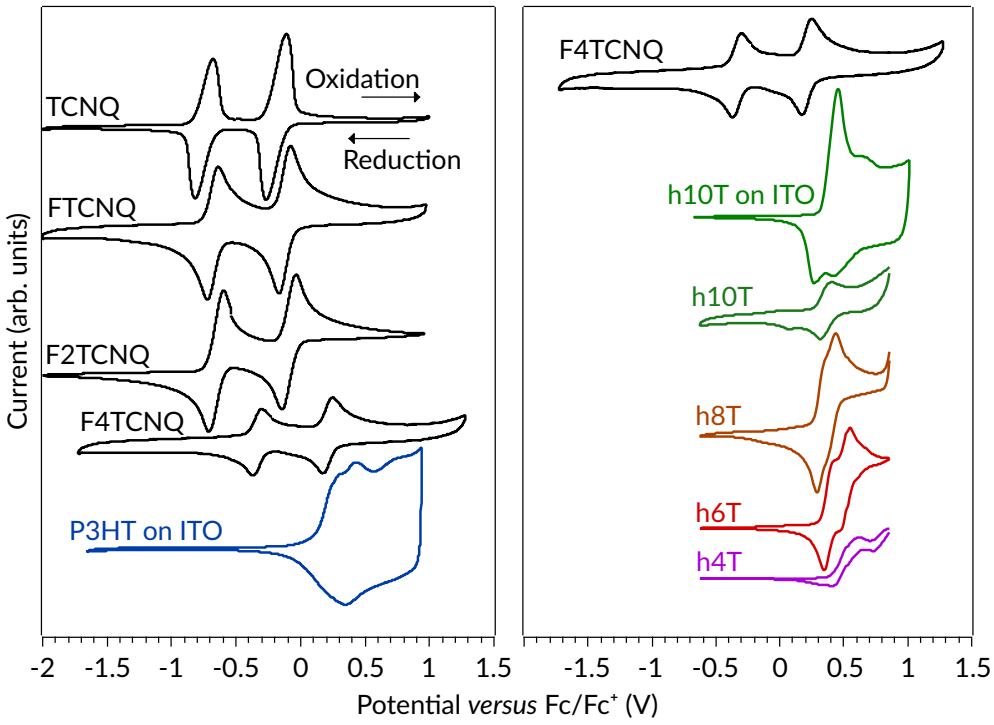


Figure C.9: Cyclic voltammograms. Left: F4TCNQ, F2TCNQ, FTCNQ, and TCNQ dissolved in acetonitrile (scan rate $0.05\,\mathrm{V\,s^{-1}}$), references against spin-cast P3HT on ITO ($0.02\,\mathrm{V\,s^{-1}}$). P3HT shows a peak at 0.42 V with a shoulder at 0.28 V which can be interpreted as yielding from the amorphous and crystalline phases, respectively [76, 233]. With the crystalline peak at lower voltage, the onset-determined $IE$ is rather descriptive of this phase. Considering only this $IE$ value in the calculation of the HOMO-DOS width, one must note that its results do not discriminate between contributions from crystalline and amorphous phases. Right: h10T, h8T, h6T, and h4T dissolved in dichloromethane (scan rate $0.05\,\mathrm{V\,s^{-1}}$) and drop-cast h10T on ITO in acetonitrile ($0.02\,\mathrm{V\,s^{-1}}$) referenced against F4TCNQ.

## C.5 Conductivity

Table C.1: Thin-film conductivity of pure P3HT and of FxTCNQ (x=0,1,2,4) doped P3HT at increasing dopant molar ratios $\chi$, as depicted in figure 4.5. ‡Alternative value obtained upon further investigation of the increase in conductivity from 9 to 17% TCNQ where I found the 17% data point to not be reproducible.

| $\chi$ (%) | Conductivity ($S\,cm^{-1}$) | | | |
|---|---|---|---|---|
| | F4TCNQ | F2TCNQ | FTCNQ | TCNQ |
| 0 | $(6.1 \pm 0.9) \times 10^{-6}$ | | | |
| 1 | $(4.6 \pm 1.0) \times 10^{-4}$ | $(3.7 \pm 0.9) \times 10^{-5}$ | $(9 \pm 2) \times 10^{-6}$ | $(2.8 \pm 0.7) \times 10^{-6}$ |
| 2 | $(3.8 \pm 0.7) \times 10^{-3}$ | $(4 \pm 2) \times 10^{-4}$ | $(3.7 \pm 0.7) \times 10^{-5}$ | $(2.4 \pm 0.5) \times 10^{-6}$ |
| 5 | $0.29 \pm 0.08$ | $(1.8 \pm 0.6) \times 10^{-2}$ | $(1.4 \pm 0.3) \times 10^{-4}$ | $(7 \pm 2) \times 10^{-7}$ |
| 9 | $3.2 \pm 0.6$ | $(3.1 \pm 0.9) \times 10^{-3}$ | $(7.7 \pm 0.8) \times 10^{-5}$ | $(7 \pm 3) \times 10^{-7}$ |
| 17 | $2.6 \pm 0.6$ | $(4 \pm 2) \times 10^{-2}$ | $(1.9 \pm 0.3) \times 10^{-5}$ | $(2.3 \pm 0.4) \times 10^{-5}$ |
| | | | | $(5 \pm 2) \times 10^{-8}$‡ |

## C.6 Computational Data

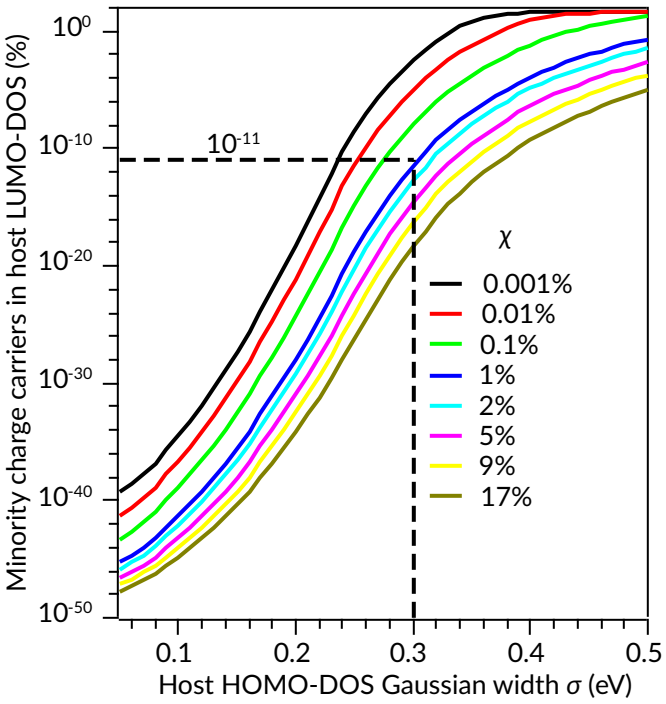


Figure C.10: Minority charge-carrier (holes in HOMO-DOS and electrons in LUMO-DOS) population in the host LUMO-DOS relative to the sum of such populations in the HOMO- and LUMO-DOS, each, of both the host and dopant; calculated for different dopant molar ratios $\chi$ and host HOMO-DOS width $\sigma$; within the resolution of the graph, the results are the same for all host-dopant pairs of the present study. The respective dopant HOMO-DOS data stays below $10^{-49}$% for the whole range of $\chi$ and $\sigma$. As explained in section 4.2, the focus, here, lies on the host HOMO-DOS and dopant LUMO-DOS. With the dopant HOMO-DOS being entirely negligible, the validity of this focus is only limited by the minority charge-carrier population in the host LUMO-DOS. Within the range of the present experimental data ($\chi \geq 1$%) this validity is well-maintained since the relative host LUMO-DOS population never exceeds $10^{-11}$% (horizontal dashed line), considering the overall maximum $\sigma = 0.23$ eV found for the investigated systems and going further beyond to 0.30 eV (vertical dashed line).

Table C.2: Molecular dipole and quadrupole moments for F4TCNQ, F2TCNQ, FTCNQ, and TCNQ as calculated trough DFT (see section 4.2 for details).

| | | Dipole moment (D) | | | |
|---|---|---|---|---|---|
| | | x | y | z | Magnitude |
| TCNQ | neutral | -0.000008 | 0.000005 | 0.000236 | 0.000236 |
| | charged | 0.000003 | -0.000005 | 0.000152 | 0.000152 |
| FTCNQ | neutral | -0.377923 | 0.825899 | 0.001934 | 0.908262 |
| | charged | 0.071174 | 0.139040 | 0.002171 | 0.156213 |
| F2TCNQ | neutral | 0.000041 | 0.000127 | 0.000442 | 0.000463 |
| | charged | -0.000018 | -0.000030 | -0.000163 | 0.000165 |
| F4TCNQ | neutral | 0.000000 | 0.000600 | -0.000013 | 0.000600 |
| | charged | 0.000003 | 0.001362 | -0.001716 | 0.002188 |

| | | Quadrupole moment (D) | | | |
|---|---|---|---|---|---|
| | | xx | yy | zz | magnitude |
| TCNQ | neutral | -70.69 | 12.32 | 58.37 | 75.52 |
| | charged | -156.62 | 34.51 | 122.11 | 164.58 |
| FTCNQ | neutral | -70.30 | 8.13 | 62.18 | 76.92 |
| | charged | -157.56 | 30.50 | 127.06 | 167.13 |
| F2TCNQ | neutral | -70.63 | 4.02 | 66.61 | 79.34 |
| | charged | -158.88 | 26.48 | 132.41 | 170.25 |
| F4TCNQ | neutral | -69.51 | -5.49 | 75.00 | 83.61 |
| | charged | -162.61 | 19.54 | 143.07 | 177.56 |